UNIVERSITAT POLITÈCNICA DE VALÈNCIA

INSTITUTO INTERUNIVERSITARIO DE INVESTIGACIÓN DE RECONOCIMIENTO MOLECULAR Y DESARROLLO TECNOLÓGICO

Design of novel bio-gated nanomaterials for sensing and therapeutic applications

PhD. THESIS

Submitted by

Maria del Mar Oroval Cucarella

PhD. Supervisors:

Prof. Ramón Martínez-Máñez
Dr. María Dolores Marcos Martínez
Dr. Maria Carmen Coll Merino

Valencia, January 2017

idm
Instituto Interuniversitario de Reconocimiento
Molecular y Desarrollo Tecnológico

Escuela Técnica Superior de Ingeniería del Diseño

RAMÓN MARTÍNEZ MÁÑEZ, PhD in Chemistry and Professor at the Universitat Politècnica de València, MARÍA DOLORES MARCOS MARTÍNEZ, PhD in Chemistry and Lecturer at the *Universitat Politècnica de València,* and MARIA CARMEN COLL MERINO, PhD in Chemistry

CERTIFY:

That the work *"Design of novel bio-gated nanomaterials for sensing and therapeutic applications"* has been developed by Maria del Mar Oroval Cucarella under their supervision in the Instituto Interuniversitario de Investigación de Reconocimiento Molecular y Desarrollo Tecnológico de la *Universitat Politècnica de València*, as a thesis Project in order to obtain the degree of PhD in Chemistry at the *Universitat Politècnica de València.*

Valencia, January 2017.

Prof. Ramón Martínez -Máñez Dr. M Dolores Marcos Martínez

Dr. M. Carmen Coll Merino

Als meus pares i a Dani.

Agraïments.

Aknowledgements. Agradecimientos.

Arribat aquest moment, voldria agrair a totes aquelles persones que m'han acompanyat al llarg d'aquest camí i que, d'una manera o altra, han contribuït a la realització d'aquesta tesi.

En primer lloc voldria donar les gràcies als meus directors. Gràcies a Loles Marcos i a Ramón Martínez per confiar en mi i per donar-me l'oportunitat de fer el doctorat en el seu grup d’investigació. Gràcies a Carmen Coll per tantes que coses que m'ha ensenyat sobre materials, pel seu suport i per intentar ajudar-me sempre encara que fora en la distància.

Gràcies a Félix Sancenón, per la seua dedicació i per oferir-me sempre la seua ajuda quan la necessitava. Gràcies a Estela Climent, per la seua dedicació i per tantes coses que em va ensenyar en el meu primer treball d’investigació, que m'ha servit de referent al llarg d'aquests anys. Gràcies a Andrea Bernardos, per la seua ajuda essencial durant l'últim període de la meua tesi, per tindre sempre temps per a mi sense esperar res a canvi i sobretot per la seua amistat.

Gràcies a Reynaldo Villalonga per acollir-me en el seu laboratori a la Universitat Complutense de Madrid durant sis setmanes. Gràcies també a Paula Díez i a Alfredo Sánchez per la seua ajuda i dedicació durant la meua estada al seu laboratori.

Gràcies a Dmitry Shchukin per obrir-me les portes del seu grup d’investigació a la Universitat de Liverpool per poder realitzar una estada d’investigació, i per la seua dedicació. Gràcies també als membres del seu grup d'investigació per acollir-me com una més i ajudar-me en tot el que estava a la seua mà. Sobretot a Paula Félix, per la seua infinita ajuda, tant dins com fora del laboratori, i per fer-me sentir un poquet més a prop de casa.

Agraïments

Gràcies als que han estat els meus companys i companyes indispensables en aquesta etapa. Al vostre costat he après i he crescut com a persona i com a investigadora. Gràcies per la vostra amistat, pel vostre suport i sobretot per fer-me aquesta etapa més fàcil i més feliç.

Als meus amics i amigues que, encara que no entenguen massa bé que és això del món de la investigació científica, sempre tenen paraules de suport i s'alegren dels meus èxits com si foren seus.

I finalment, gràcies a la meua família. Especialment als meus pares pel seu suport incondicional, per estimar-me i cuidar-me tant, i per creure en mi més que jo mateixa. Gràcies a Dani, per escoltar-me i donar-me el seu suport sempre, i per despertar-me cada dia el cor i el somriure.

Abstract

The present PhD thesis, entitled “Design of novel bio-gated nanomaterials for sensing and therapeutic applications”, is focused on the design, preparation, characterization and evaluation of new smart hybrid organic-inorganic materials for their applications on the field of sensing and controlled drug delivery.

The first chapter of this thesis introduces the concept of organic-inorganic hybrid materials containing switchable “gate-like” ensembles and their applications in the detection of chemical and biochemical species and as suitable materials for drug delivery applications.

The second chapter describes the preparation of an aptamer-capped mesoporous material for the fluorogenic detection of α-thrombin in human plasma and serum. Dye-loaded MCM-41 particles were capped with a thrombin aptamer (TBA) for the preparation of the material. In the presence of α-thrombin, TBA was displaced from the surface due to the formation of TBA−protein complex, triggering the release of the dye. The capped system was tested in simulated human blood plasma and in PBS buffer with 10% of human serum and achieved a low limit of detection (LOD) for thrombin. Moreover, the prepared material displayed great selectivity for α-thrombin in the presence of other non-exclusive binding proteins. The gated-nanomaterial resulted suitable to perform an accurate α-thrombin detection in human serum.

In the third chapter a new fluorogenic sensing nanoprobe for the detection of As(III) is described. The system consists of the combination of MSNs with an aptamer (Ars-3), which possesses a very high affinity to As(III), as a pore blocking agent. The sensitivity of the nanocarrier for As(III) was further studied. Furthermore, the selectivity of the nanocarrier towards As(III) in the presence of other cations was also successfully verified. In addition, the sensor allowed accurate As(III) determination in real media.

The fourth chapter reports a novel proof-of-concept to detect *Mycoplasma* genomic DNA and cocaine. The new approach combined gated mesoporous silica nanoparticles and surface-enhanced Raman scattering (SERS) spectroscopy. In particular, two gated-hybrid mesoporous materials loaded with a SERS reporter and capped with suitable oligonucleotide sequences to detect *Mycoplasma* genomic DNA or cocaine, were prepared. Release of the reporter was triggered from the different materials by the presence of the corresponding target, and was detected by SERS upon adsorption on gold nanotriangles. This novel procedure allowed detecting *Mycoplasma* genomic DNA and cocaine with a high selectivity and sensitivity.

The fifth chapter describes the development of a nanodevice able to deliver insulin as a function of the glucose concentration, in simulated human blood plasma. The glucose-driven nanomaterial consisted of β-cyclodextrin-modified glucose oxidase (CD-GOx)-capped silica nanoparticles loaded with insulin. The reaction of glucose by the capping enzyme (GOx) triggered insulin release in a self-regulated manner. Furthermore, the response to glucose was found to be selective and other saccharides were unable to deliver the entrapped insulin.

We hope the results obtained in this thesis may inspire further works to design smart nanodevices with application in analytical chemistry, clinical or environmental assays and self-regulated drug delivery systems.

Resumen

La presente tesis doctoral, titulada "Diseño de nuevos nanomateriales con puertas moleculares biológicas para aplicaciones de detección y terapéuticas", se centra en el diseño, preparación, caracterización y evaluación de nuevos materiales híbridos orgánicos-inorgánicos inteligentes para su aplicación en el campo de la detección y liberación controlada de fármacos.

El primer capítulo de la presente tesis introduce el concepto de los materiales híbridos orgánicos-inorgánicos funcionalizados con puertas moleculares y su aplicación en la detección de especies químicas y bioquímicas de interés, y como materiales adecuados para su aplicación en liberación controlada de fármacos.

El segundo capítulo describe la preparación de un material mesoporoso con aptámeros como puerta moleculares, para la detección fluorogénica de α-trombina en plasma y suero humano. En la preparación del material se utilizaron partículas de MCM-41 cargadas con un colorante y cuyos poros se taparon con un aptámero que reconoce la proteína trombina (TBA). En presencia de α-trombina, el TBA se desplazó de la superficie debido a la formación del complejo TBA-proteína permitiendo así la liberación del colorante. El funcionamiento del material se evaluó en plasma humano simulado y en PBS con 10% de suero humano y se alcanzó un bajo límite de detección (LOD) para trombina. Además, el material resultó ser selectivo para α-trombina en presencia de otras proteínas no específicas. El nanomaterial resultó adecuado para la detección precisa de α-trombina en suero humano.

En el tercer capítulo se describe una nuevo nanomaterial sensor para la detección fluorogénica de As (III). El sistema consiste en la combinación de nanopartículas mesoporosas de sílice (MSNs) con un aptámero (Ars-3), que posee una alta afinidad por el As(III), como agente bloqueante de los poros. Además, se estudió la sensibilidad del nanomaterial para As(III). Por otro lado, se demostró la selectividad del nanomaterial para As(III) en presencia de otros cationes.

Adicionalmente, el sensor permitió una determinación precisa de As(III) en un medio real.

El cuarto capítulo describe una novedosa prueba de concepto para la detección de ADN genómico de *Mycoplasma* y cocaína. El nuevo enfoque combinó MSNs con puertas moleculares y espectroscopía Raman amplificada en superficie (SERS). En particular, se prepararon dos materiales híbridos con puertas moleculares y cargados con un reportero SERS. Como puertas moleculares se utilizaron dos secuencias de oligonucleótidos para detectar ADN genómico de *Mycoplasma* o cocaína. La liberación del reportero SERS desde los materiales se indujo por la presencia del analito correspondiente, y fue detectado por SERS tras su adsorción sobre nanotríangulos de oro. Este nuevo procedimiento permitió detectar ADN genómico de *Mycoplasma* y cocaína con alta selectividad y sensibilidad.

El quinto capítulo describe el desarrollo de un nanodispositivo capaz de liberar insulina en función de la concentración de glucosa en plasma sanguíneo humano simulado. El nanomaterial consiste en nanopartículas de sílice funcionalizadas cuyos poros se taparon con la enzima glucosa-oxidasa modificada con β-ciclodextrinas (CD-GOx) y cargadas con insulina. La reacción de la glucosa con la enzima bloqueante (GOx) desencadenó la liberación autorregulada de insulina. Asimismo, se encontró que la respuesta a la glucosa era selectiva y otros azúcares no indujeron la liberación de la insulina cargada.

Esperamos que los resultados obtenidos en esta tesis puedan inspirar otros trabajos para diseñar nanodispositivos inteligentes con aplicación en la química analítica, ensayos clínicos o medioambientales y en sistemas de liberación autorregulada de fármacos.

Resum

La present tesi doctoral, titulada "Disseny de nous nanomaterials amb portes moleculars biològiques per a aplicacions de detecció i terapèutiques", es centra en el disseny, preparació, caracterització i avaluació de nous materials híbrids orgànics-inorgànics intel·ligents per a la seua aplicació en el camp de la detecció i lliberació controlada de fàrmacs.

El primer capítol de la present tesi introduïx el concepte dels materials híbrids orgànics-inorgànics funcionalizats amb portes moleculars i la seua aplicació en la detecció d'espècies químiques i bioquímiques d'interés i com a materials adequats per a la lliberació controlada de fàrmacs.

El segon capítol descriu la preparació d'un material mesoporós amb aptàmers com a porta molecular, per a la detecció fluorogénica de α-trombina en plasma i sèrum humà. En la preparació del material es van utilitzar partícules de MCM-41 carregades amb un colorant i els porus del qual es van tapar amb un aptàmer que reconeix la proteïna trombina (TBA). En presència de α-trombina el TBA es va desplaçar de la superfície a causa de la formació del complex TBA-proteïna permetent així l'alliberament del colorant. El funcionament del material es va avaluar en plasma humà simulat i en PBS amb 10% de sèrum humà i es va aconseguir un baix límit de detecció (LOD) per a trombina. A més, el material va resultar ser selectiu per a α-trombina en presència d'altres proteïnes no específiques. El nanomaterial va resultar adequat per a la detecció precisa de α-trombina en sèrum humà.

En el tercer capítol es descriu un nou nanomaterial sensor per a la detecció fluorogènica d'As(III). El sistema consistix en la combinació de nanopartícules mesoporoses de sílice (MSNs) amb un aptàmer (Ars-3), que posseïx una alta afinitat per l'As(III), com a agent bloquejant dels porus. A més, es va estudiar la sensibilitat del nanomaterial per a As(III). D'altra banda, es va demostrar la selectivitat del nanomaterial per a As(III) en presència d'altres cations. Addicionalment, el sensor va permetre una determinació precisa d'As(III) en un medi real.

El quart capítol descriu una nova prova de concepte per a la detecció de ADN genòmic de *Mycoplasma* i cocaïna. El nou enfocament va combinar MSNs amb portes moleculars i espectroscòpia Raman amplificada en superfície (SERS). Concretament, es van preparar dos materials híbrids amb portes moleculars i carregats amb un reporter SERS. Com a portes moleculars es van utilitzar dos seqüències d'oligonucleòtids per a detectar ADN genòmic de *Mycoplasma* o cocaïna. L'alliberament del reporter SERS des dels materials es va induir per la presència de l'anàlit corresponent, i va ser detectada per SERS després de la seua adsorció sobre nanotriangles d'or. Este nou procediment va permetre detectar ADN genòmic de *Mycoplasma* i cocaïna amb alta selectivitat i sensibilitat.

El quint capítol descriu el desenrotllament d'un nanodispositiu capaç d'alliberar insulina en funció de la concentració de glucosa en plasma sanguini humà simulat. El nanomaterial consistix en nanopartícules de sílice funcionalizades els porus del qual es van tapar amb l'enzim glucosa-oxidasa modificada amb ß-ciclodextrines (CD-GOx) i carregades amb insulina. La reacció de la glucosa per l'enzim bloquejant (GOx) va desencadenar l'alliberament autoregulat d'insulina. Així mateix, es va trobar que la resposta a la glucosa va ser selectiva i altres sucres no van induir la lliberació de la insulina carregada.

Esperem que els resultats obtinguts en aquesta tesi puguen inspirar nous treballs per a dissenyar nanodispositius intel·ligents amb aplicació en la química analítica, assajos clínics o mediambientals i en sistemes de lliberació autoregulada de fàrmacs.

Abbreviations and Acronyms

APTES	*(3-aminopropyl)triethoxysilane*
ATP	*adenosine triphosphate*
AuNPs	*Gold nanoparticles*
AuNTs	*Gold nanotriangles*
BET	*Brunauer-Emmet-Teller*
BJH	*Barrett-Joyner Halenda*
BSA	*Bovine serum albumin*
cAMP	*Cyclic adenosine monophosphate*
CAT	*Catalase*
CD	*Cyclodextrin*
CD-GOx	*Cyclodextrin-modified-glucose oxidase*
CLSM	*Confocal laser scanning microscopy*
CMC	*Critical micelar concentration*
CTAB	*n-Cetyltrimethylammonium bromide*
CTP	*Cytosine 5'-triphosphate*
DNA	*Deoxyribonucleic acid*
DOX	*Doxorubicin*
DTT	*Dithiotheritol*
EA	*Elemental analysis*
EDC	*1-Ethyl-3-(3-dimethylaminopropyl)carbodiimide*
EDX	*Energy dispersive X-ray spectroscopy*
FITC	*Fluorescein isothiocyanate*
FTIR	*Fourier transformed infrared spectroscopy*
G-InS	*Gluconic acid-modified insulin*
GOx	*Glucose oxidase*
GSH	*Glutathione*
GTP	*Guanosine 5'-triphosphate*
GTPMS	*(3-Glycidyloxypropyl)trimethoxysilane*
HA	*Hyaluronic acid*
HIFU	*High-intensity focused ultrasound*
IUPAC	*International Union of Pure and Applied Chemistry*

LOD	*Limit of detection*
MB	*Methylene blue*
ME	*Mercaptoethanol*
MSNs	*Mesoporous silica nanoparticles*
NHS	*N-hydroxysuccinimide*
NPs	*Nanoparticles*
PBS	*Phosphate buffer solution*
PCR	*Polymerase chain reaction*
PFH	*Perfluorohexane*
PMOs	*Periodic Mesoporous Organosilicas*
PSA	*Prostate-specific antigen*
PtNPs	*Platinum nanoparticles*
PXRD	*Powder X-ray diffraction*
Rh 6G	*Rhodamine 6G*
Rh B	*Rhodamine B*
RNA	*Ribonucleic acid*
Ru(bipy)	*Tris(bipyridine)ruthenium(II) chloride*
SEM	*Scanning electron microscopy*
SERS	*Surface enhanced Raman spectroscopy*
TEM	*Transmission electron microscopy*
TEOS	*Tetraethyl orthosilicate*
TGA	*Thermogravimetric analysis*
TLCT	*True liquid-crystal templating mechanism*
TMOS	*Tetramethylorthosilicate*
TMS	*Tetramethylbenzidine*
TTF	*Tetrathiafulvalene*
US	*Ultrasound*
UTP	*Uridine triphosphate*
UV	*Ultraviolet*

Table of contents

1. **GENERAL INTRODUCTION 1**
    - 1.1 Nanotechnology... 3
    - 1.2 Organic-Inorganic Hybrid Functional Nanomaterials 4
    - 1.3 Mesoporous Silica Particles as Inorganic Scaffolds 7
    - 1.4 Advanced Applications of Functional Organic-Inorganic Hybrid Supports: Gated Materials.. 24
2. **OBJECTIVES...63**
3. ***CHAPTER II. An Aptamer-Gated Silica Mesoporous Material for Thrombin Detection*** **..67**
4. ***CHAPTER III. Selective fluorogenic sensing of As(III) using aptamer-capped nanomaterials*** **...93**
5. ***CHAPTER IV. Surface Enhanced Raman Scattering and Gated Materials for Sensing Applications: The Ultrasensitive Detection of Mycoplasma and Cocaine*** **...123**
6. ***CHAPTER V. Self-Regulated Glucose-Sensitive Neoglycoenzyme-Capped Mesoporous Silica Nanoparticles for Insulin Delivery*** **...........159**
7. **GENERAL DISCUSSION..185**
8. **CONCLUSIONS 191**
9. **APPENDICES .... .195**
    - i. Publications object of this thesis.......................................197
    - ii. Other scientific contributions 198

1. General Introduction

1.1 Nanotechnology

The field of nanoscience and nanotechnology emerged and consolidated as a distinct field in the decades of eighties and nineties, thanks to the contributions of three scientist considered the fathers of this field: Richard Feynman, Norio Taniguchi and Eric Drexler. While Richard Feynman presaged the whole field in the mid-80s, Norio Taniguchi coined the term “nanotechnology” in 1974.[1] Later on in 1986, Eric Drexler published the first book on molecular nanotechnology “*Engines of creation: the coming era of nanotechnology*”.[2] Since then, nanoscience has represented an ongoing technology revolution.

Essentially nanotechnology is the study, design, synthesis and application of functional materials, devices, and systems through control of matter at the atomic and molecular levels at the nanometer scale (1–100 nm).[3,4] Nanotechnology has resulted from the convergence of different disciplines such as chemistry, physics, biology, material science and engineering. This interdisciplinary science encompasses the production and application of physical, chemical, and biological systems at scales ranging from individual atoms or molecules to submicron dimensions, as well as the integration of the resulting nanostructures into larger systems, offering immense opportunities and challenges.[5]

The emergence of a wide range of new nanomaterials has endowed nanotechnology with many potential applications in numerous aspects of everyday life and in many research fields such as: agriculture, medicine, coatings, cosmetics, electronics, energy storage, catalysis and food packaging.[6–10] In this context, different types of nanomaterials have been developed such as carbon nanotubes, nanocomposites, silica nanoparticles, metal based nanoparticles, polymer nanoparticles, quantum dots, etc.[11]

1.2 Organic-Inorganic Hybrid Functional Nanomaterials

Although the fields of molecular and supramolecular chemistry and inorganic materials have traditionally been poorly interrelated, research in this currently highly interdisciplinary region has recently emerged exponentially and has resulted in many novel hybrid materials with advanced functions in a surprisingly short time.[12] These hybrid materials are synthetized with the aim to achieve specific properties that are very difficult to satisfy by using single component based materials. The combination of (bio)organic and inorganic components at the nanoscale leads to nanocomposite materials with improved properties due to the synergistic effects of this coupling.[13–15]

In this context, hybrid organic inorganic materials within the nanoscale range have attracted considerable interest due to the combination of the beneficial characteristic of organic and (bio)organic chemistry and material science. The inorganic components can provide mechanical, thermal, or structural stability, whereas organic groups can introduce flexibility into the framework, or change, for instance, the optical properties of the material. In other words, as noted by Professor Clément Sánchez "Hybrid organic-inorganic materials are not simply physical mixtures. They can be broadly defined as molecular or nano-composites with (bio)organic and inorganic components, intimately mixed where at least one of the component domains has a dimension ranging from a few Å to several nanometers. Consequently the properties of hybrid materials are not only the sum of the individual contributions of both phases, but the role of their inner interfaces could be predominant".[16]

This implies that anchoring organic molecules, biomolecules, or supramolecules onto selected inorganic scaffoldings with different chemical nature, sizes, and shapes promotes the development of smart nanodevices that can be applied in a number scientific and technological fields.[17–22] The sections below are devoted to detail the synthesis, characterization, main features and some examples of hybrid organic inorganic nanomaterials.

1.3 Mesoporous Silica Particles as Inorganic Scaffolds

Among different inorganic or hybrid solids, much attention has been paid in recent years to periodic porous materials in fundamental and applied research. The great interest they have gained is due to the possibility of tailoring the pore structure, framework composition, and morphologies over a wide range. According to their pore sizes, porous materials are classified by the IUPAC (International Union of Pure and Applied Chemistry) as microporous (pore size <2 nm), mesoporous (2–50 nm) and macroporous (>50 nm) materials.[23] A great number of potential applications arise from the promising properties of these high-surface area materials including separation,[24] catalysis,[25] electronics,[26] energy conversion and storage,[27] and sensor technology.[28]

Zeolites, a well-known example of this type of materials, is a family of microporous aluminosilicates materials which act as molecular sieves adsorbing molecules with certain dimensions able to enter the pores. These materials have been traditionally used in the industry for gas separation,[29] but they are mainly used as catalysts in the petrochemical industry.[30] Despite the enormous industrial importance of zeolites, their application is limited by their relatively modest pore size, which is in any case less than a nanometer. Therefore, the need of porous ordered materials with pore sizes higher than a nanometer promoted the research in this field.

Within this framework, the patents and publications of the first highly ordered mesoporous materials developed by the scientists at the Mobil Research and Development Corporation in 1992, was a breakthrough that aroused great interest in the scientific world.[31,32] The authors described the synthesis of a new mesoporous silica family known as M41S phases. The features of these mesostructured materials allowed to overcome the limitations of the zeolite's pore size (restricted to *ca.* 15 Å) and, consequently, provided new opportunities in a variety of applications.

The most common and best-known ordered mesoporous frameworks are the three discrete structures MCM-41 (with a hexagonal arrangement of the mesopores), MCM-48 (with a cubic arrangement of the mesopores), and MCM-50 (with a laminar structure) (see Figure 1).[33] This new family of materials is obtained by a mechanism designed as "liquid-crystal templating", which is based on a surfactant-assisted process. The variation of the synthesis conditions such as temperature, pH or concentration determines the formation of one or another material.

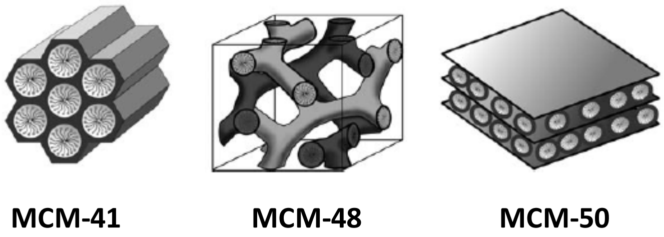

Figure 1. Structures of mesoporous M41S phase materials: MCM-41 (2D hexagonal), MCM-48 (cubic) and MCM-50 (lamellar). *Reprinted with permission from Angew. Chem. Int. Ed. 2006, 45, 3216. Copyright © 2006 Wiley-VCH Verlag GmbH & Co. KGaA, Weinheim.*

This class of materials is characterized by uniform cylindrical pores ranging from 2 to 10 nm, a high pore volume in the order of 1 cm^3 g^{-1}, large surface area with values from 500 to 1000 m^2 g^{-1}, and amorphous pore walls. In addition, these materials are featured by high chemical and thermal stability. On the other hand, the synthetic procedure is well described and requires inexpensive and nonhazardous precursors which facilitates large-scale production and that can be chemically modified using well-known silicon oxide functionalization chemistry. These outstanding characteristics make these materials highly suitable as scaffolds for hosting molecules in the design of materials for controlled release studies upon the exposition to an external stimulus, which is the essential objective of the present PhD thesis.

1.3.1 Synthesis of inorganic mesoporous materials

As stated above, regardless the huge industrial importance of zeolites, their use for certain applications is limited by their relatively small pore size (less than a nanometer). Thus, the requirement of new ordered porous systems with pores of larger dimensions, triggered the research on mesoporous materials. As pointed in section 1.2, the first successful method and still most studied was based on silica. Basically, to accomplish the synthesis of a high ordered porous structure with homogenous pore dimensions two essential components are necessary:

- ✓ a ***template*** which acts as a structure-directing agent of the high ordered porous net.
- ✓ a ***polymeric precursor*** which has to self-organize around the template and build up the final rigid structure by means of a polymerization reaction.

Typically, a synthetic route to achieve a highly ordered porous structure requires a homogeneous surfactant solution dissolved in the medium (water). The most innovative part of the procedure described by researchers of the Mobil Oil Company, is the use of supramolecular aggregates of ionic surfactants (long-chain alkyltrimethylammonium halides) as structure directing agents instead of using the traditional cationic organic species, widely used as templates in the assembly of microporous zeolitic structures.[32] Therefore, comprehension of the behavior of the surfactant in aqueous solution is essential to understand the relationship between the surfactant and the formation of the final mesostructured material.

Surfactants or directing agents are large organic molecules with amphiphilic character, formed by hydrophilic (polar head) and hydrophobic (non-polar hydrocarbon chain) components. In order to reduce the contact between the surfactant hydrophobic chains and the aqueous media, these amphiphilic species self-organize by aggregating their non-polar cues and forming micelles. Thus, the minimum energy configuration is reached and the produced micelles are in equilibrium with surfactant molecules in solution, as depicted in Figure 2.

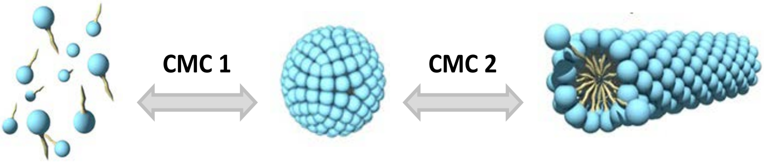

Figure 2. Surfactant molecules, spherical micelle and cylindrical micelle.

The critical micelle concentration (CMC 1) is defined as the lowest concentration at which the formation of spherical micelles is observed. The second critical micelle concentration (CMC 2) is the concentration at which spherical micelles begin to transform into cylindrical micelles. The concentration required for the formation of both micelle types strongly depends on the nature of the surfactant used, its concentration, temperature, the pH of the solution and the total salt concentration. Those micelles can self-organize into supramicellar structures and, depending on the same parameters cited above, three different phases of supermicellar aggregates can be obtained: hexagonal, cubic and laminar (Figure 3). Thereby, by varying the synthesis parameters different "template shapes" can be obtained.

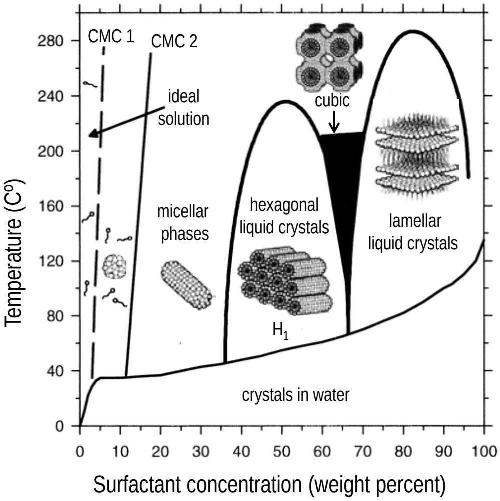

Figure 3. Schematic phase diagram for the surfactant cetyltrimethylamonium bromide (CTABr) in water. The aggregation of surfactant molecules into micelles and then into lyotropic liquid crystalline phases as a function of concentration and of temperature is shown. *Adapted from Chem. Mater., 1996, 8, 1682, Copyright © 1996 American Chemical Society.*

The so-called sol-gel process under which the synthesis of inorganic silica based ordered structures is carried out, consists on the hydrolysis and polycondensation of oligomeric silicates-type precursors originating from different sources of silica (e.g. sodium silicate, alkoxydes like tetraethylorthosilicate (TEOS) and tetramethylorthosilicate (TMOS)).

Once the supramicellar aggregates are formed, the silica precursors are added to the reaction mixture. Under specific conditions of pH and temperature the silica precursor molecules are hydrolyzed and condensed around the supramicellar aggregates template, yielding a silicon oxide phase. The final mesoporous materials are obtained by subsequent removal of the surfactant by aerobic high temperature calcination or extraction with adequate solvents.[34]

In an attempt to clarify the formation of these materials, researchers suggested two different mechanisms involved in the synthetic process. These two pathways are schematically represented in Figure 4. The first one is the so-called True Liquid-Crystal Templating (TLCT), and occurs when the concentration of surfactant is sufficiently high to allow the formation of the lyotropic liquid crystal phase without requiring the presence of the inorganic precursor. The other mechanism is a cooperative self-assembly type mechanism. In this case, it is considered that when the concentration of the surfactant is insufficient, the formation of the liquid crystal phase can be promoted by the inorganic precursor.[35]

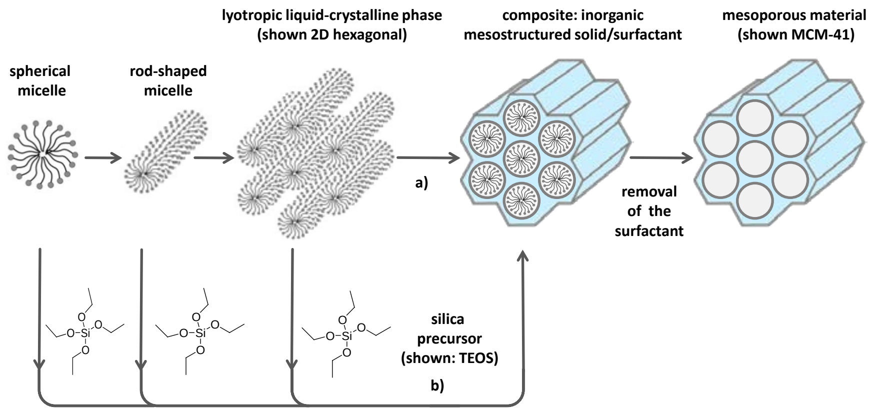

Figure 4. Schematic representation of the formation of mesoporous materials by structure-directing agents: a) true liquid-crystal template mechanism; b) cooperative liquid crystal template mechanism. *Adapted from Angew. Chem. Int. Ed. 2006, 45, 3216.Copyright © 2006 Wiley.*

Essentially, synthesis conditions; such as source of silica, pH and composition of the reaction mixture, ionic strength, type of surfactant used, temperature and time affect the surfactant micellar conformation, the silica-surfactant interactions and the degree of silica poly-condensation. These conditions also determine the features of the final porous net such as the type of mesostructure, diameter and volume of pores, wall thickness and the macroscopic morphology.

Meanwhile, this original approach has been extended by a wide number of variations with the aim to obtain a large variety of mesoporous materials with different defined topology and morphology. For instance, triblock copolymer templates are employed, under acidic conditions, to prepare the so-called SBA (Santa Barbara Amorphous) silica phases.[36,37]

Among the MS41 family of materials, the one that has been more extensively studied and used is MCM-41, showing hexagonal arrays of cylindrical mesopores. As can be seen in Figure 4, under the correct pH, temperature and concentration conditions, the surfactant (CTABr) self-organizes into hexagonal shaped supramolecular aggregates. Subsequently, the inorganic siliceous precursor (TEOS) is added to the solution, under basic reaction conditions, and it polymerizes around the supermicellar-template giving rise to the final mesoscopically ordered composite formation. The obtained as-synthesized material may undergo a calcination or extraction process in order to obtain the final mesoporous scaffold, formed by hollow unidirectional channels in a hexagonal arrangement and of *ca.* 2.5 nm of diameter.[38]

By following this synthetic route the high degree of homogeneity of the initial elements is transmitted to the final material, yielding a system of pores not only homogeneously in size but also in shape and regularity. Additionally, an important feature of this MCM-41-type material is its versatility, since it is possible to modify its final characteristics by the introduction of small changes in the synthesis route or through a post-synthesis treatment. In fact, controlling the morphology of this type of materials is one of the main challenges that need to be addressed in order to enable their use in advanced applications. For instance, the particle morphology can be tuned from micrometric and heterogeneous particles to produce different forms, including thin films, nanoparticles or monoliths.[39–42]

On the other hand, the modulation of the pore size is also as important as modulating the particle size or morphology. Basically, three different approaches have been developed that attempt to expand the pore sizes of mesoporous materials, while retaining the original morphology and the highly ordered hexagonal mesopores: i) by changing the lengths of the alkyl chains in the surfactant; ii) by spontaneous self-swelling of the material in the reaction mixture; iii) by using suitable swelling organic molecules (hydrophobic reagents).[43–49] The first approach, is based on the idea that if identical numbers of surfactants with shorter alkyl-chain lengths are replaced by surfactants with longer alkyl-chain lengths, the pore sizes of the mesoporous silica should increase (see Figure 5a).[50] By following this approach pores enlarged more than 3-4 nm cannot be obtained, due to the poor solubility of alkyl-chains with more than 20 carbon atoms. In the second one, the heating of the reaction mixture is prolonged to temperatures of about 150 °C.[44] With these method, pore enlargement to 6 nm have been reported.[44] However, the most frequently used approach is the introduction of a swelling agent into the structure directing template, either in the preparation step or in the post-synthesis hydrothermal treatment.[51–54] In this method, it is assumed that the swelling agent (i.e.: 1,3,5-trimethylbenzene, TMB) penetrates into hydrophobic parts of micelle rods inside mesopores, due to the strong hydrophobic interaction with the surfactant's alkyl chain. The incorporation of the swelling agent into the mesopores leads to the pore expansion of the mesoporous silica framework to a huge extent (Figure 5b).[48,55]

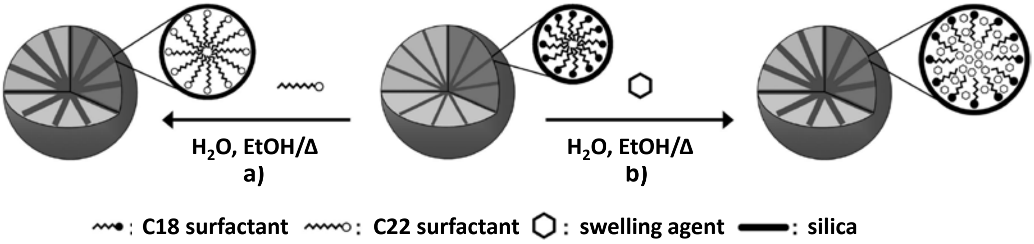

Figure 5. Schematic representation of pore expansion of mesoporous silica scaffolds: a) using longer alkyl chains and b) using swelling organic molecules. *Adapted from Chem. Mater. 2008, 20, 4777. Copyright © 2008 American Chemical Society.*

1.3.2 Obtaining hybrid organic-inorganic materials: functionalization of mesoporous silica scaffolds

As stated in Section 1.2, the preparation of organic-inorganic hybrid materials is particularly appealing because of the possibility to combine the functional variation of organic chemistry with the benefits of a thermally stable and robust inorganic scaffold. To construct such systems, it is necessary the incorporation of organic groups (functionalization) in the inorganic silica-based mesoporous scaffold.

A remarkable structural feature of mesoporous materials is that, unlike zeolites, silica-based materials do not have order at the atomic level, so that the order of these materials is related to the arrangement of the pores (mesoscopic order). Moreover, their walls present a high concentration of structural defects originating from the hydrolysis of the silica precursor and its subsequent condensation. This condensation is not complete and therefore mesoporous materials present remaining silanol (Si-OH) groups in their final structure.

These structural defects act as suitable anchoring spots for organic functionalization. Considering that, silanol groups can easily react with trialkoxysilane derivatives ($(R'O)_3SiR$, R: organic group) by means a nucleophilic aliphatic substitution, originating organic-inorganic hybrid materials. The incorporation of organic moieties allows a precise control over the features of these hybrid materials, by considering the chemical nature of the R moiety that can be selected in order to include specific groups onto the inorganic framework.[56–58]

To construct porous hybrid materials, three different synthetic routes are available for anchoring organic groups to the framework of silica-based materials:[59]

- ✓ **Grafting procedure**

This method is based on a post-synthetic procedure to modify the surface of a purely inorganic silica material. The process is carried out by reaction of trialcoxysilane derivatives ($(R'O)_3SiR$)) with the free silanol groups of the pore surfaces (see Figure 6). By following this method functionalization with a large range of organic groups can be carried out by variation of the organic moiety R. However, the number of anchored organic groups would be limited by the number of silanol groups in the surface. This functionalization method has some interesting advantages. Firstly, the mesostructure of the starting silica phase is generally retained. Secondly, due to the large number of organosilanes available, it is possible to develop a wide range of functionalized mesoporous silica phases with different chemical and physical properties, by simply varying the organic residue R.

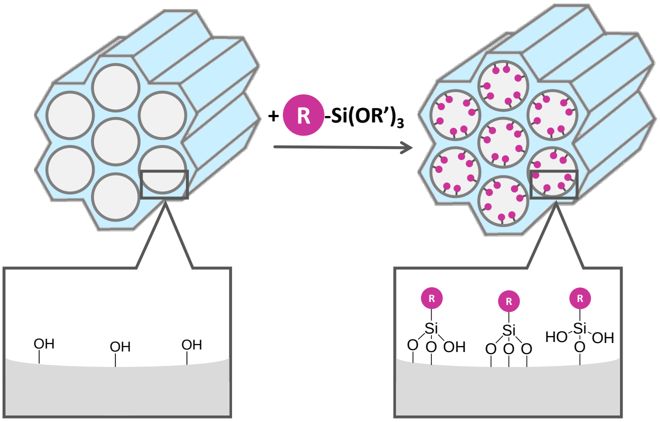

Figure 6. Grafting (postsynthetic functionalization) for organic modification of mesoporous pure silica phases with terminal organosilanes of the type $(R'O)_3SiR$. R: organic functional group. *Adapted from Angew. Chem. Int. Ed. 2006, 45, 3216. Copyright © 2006 Wiley.*

Assuming that the distribution of the reactive silanol groups in the mesoporous scaffold is on average the same in the internal and in the external surface (inside and outside the pores), the distribution of the organic molecules on the solid after the grafting may be determined by other factors. These factors are diffusion processes and steric hindrance around the silanols. If the grafting process is carried out before the removal of the surfactant, as the inner surface is occupied by the inert template, the modification takes place essentially in the external surface. On the other hand, if the template is removed before the grafting, the organosilanes react preferentially at the pore openings due to steric hindrance. Consequently, although the silica mesoporous material can present some organic groups covalently bonded into their inner surface, grafting processes occur mainly in the external surface of the inorganic scaffolds.[60,61]

Another factor to be considered in the grafting processes is the polycondensation rate of the organosilane precursor by reacting with itself rather than with the surface silanol groups. This condensation may lead to the formation of oligomers of the organosilane, which may block the pore outlets. Competition between the condensation and the grafting process itself is influenced by some parameters such as: type of organosilane and solvent, temperature reaction and amount of water adsorbed on the surface.

✓ **Co-condensation procedure**

The co-condensation method represents an alternative to synthesize organically functionalized mesoporous silica phases. In this approach, the organosilica precursor ($(R'O)_3SiR$)) is incorporated into the synthesis medium simultaneously to the corresponding tetraalkoxysilanes ($(RO)_4$-Si , TEOS or TMOS). In this case, the trialkoxyorganosilica precursors are hydrolyzed and react with the silica skeleton precursors, and a simultaneous condensation of both takes place. In the resulting framework, the organic groups R are bonded to silicon atoms of the inorganic skeleton scaffold wall (see Figure 7).

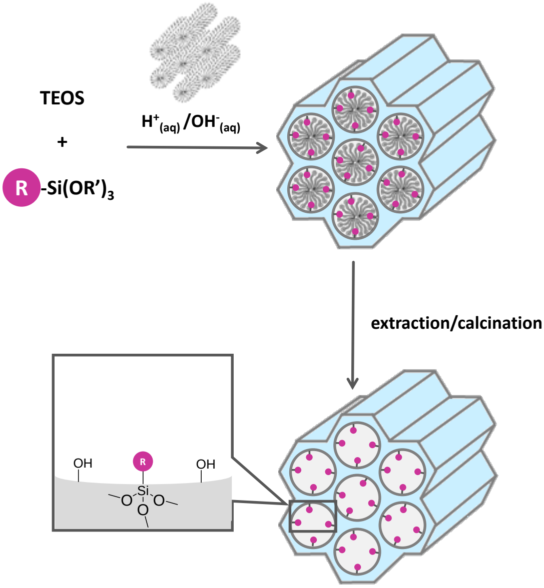

Figure 7. Co-condensation method (direct synthesis) for the organic modification of mesoporous pure silica phases. R: organic functional group. *Adapted from Angew. Chem. Int. Ed. 2006, 45, 3216.Copyright © 2006 Wiley.*

This method yields scaffolds both internal and external functionalized, thereby allowing the incorporation of a relatively high amount of functional groups. In addition, the organic units are generally more homogeneously distributed than in materials synthesized through the grafting process.[62] However, it is convenient to take into account some disadvantages of the present method:

- The presence of increasing concentration of $(R'O)_3SiR$ in the reaction mixture may interfere with the formation of micellar aggregates, decreasing the mesoscopic order in the final material and in extreme cases, leading to disordered frameworks.[60]

- Homo-condensation reactions between silane groups are favored. Consequently, the proportion of terminal organic groups that are incorporated into the pore-wall network is generally lower than would correspond to the starting concentration in the reaction mixture. In addition, the homogeneous distribution of different organic functionalities in the framework cannot be guaranteed.

- The incorporated organic groups can lead to a reduction in the pore diameter, pore volume, and specific surface area.

- Finally, only extractive methods can be used in order to remove the surfactant template, since aerobic calcinations would induce the degradation of the organic groups.

An alternative synthetic route to obtain mesoporous organic-inorganic hybrid materials consists on the preparation of *Periodic Mesoporous Organosilicas* (PMOs). These materials are synthesized by means of a condensation reaction of bridged organosilica precursors of the type $(R'O)_3Si\text{-}R\text{-}Si(OR')_3$, in the presence of a structure-directing agent. In this case, the organic units are incorporated in the three-dimensional network structure of the silica matrix through two covalent bonds and thus distributed totally homogeneously within the pore walls of the scaffold (see Figure 8). This approach leads to materials that can have large inner surface areas of up to 1800 m^2 g^{-1} as well as high thermal stability. However, by using this method a completely disordered pore system is usually obtained.[63,64]

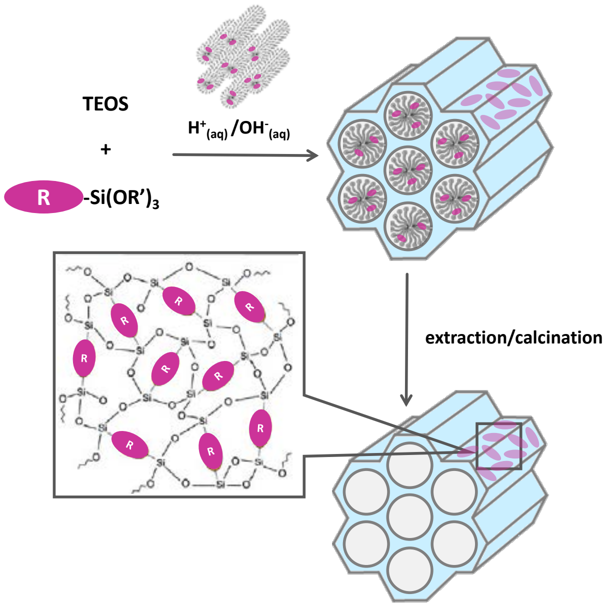

Figure 8. General synthetic pathway to PMOs that are constructed from bissilylated organic bridging units. R: organic functional group. *Adapted from Angew. Chem. Int. Ed. 2006, 45, 3216. Copyright © 2006 Wiley.*

1.3.3 Characterization of organic-inorganic mesoporous hybrid mesoporous materials

In this section, the characterization techniques that are routinely used to elucidate the structural and physico-chemical properties of hybrid mesoporous materials are detailed. In general, when characterizing a hybrid mesoporous material the main features to be considered are: i) the integrity of the mesoporous scaffold, ii) the amount of organic matter that composes the final material and, in the case of preparation of mesoporous hybrid nanoparticles, it is also convenient to analyze the iii) particle morphology and size. Table 1 summarizes the most common techniques used in the characterization of mesoporous materials.

Table 1. Characterization techniques commonly used in the determination of textural and physico-chemical properties of mesoporous materials.

Characterization technique	**Objective**
X-Ray Diffraction	Meso-scale periodicity
Transmission electron microscopy	Pore order, particle size and morphology
Nitrogen adsorption-desorption measurements	Determination of textural properties
Dynamic light scattering	Particle size
Scanning electron microscopy	Particle morphology
Thermogravimetric analysis	Quantification of organic species incorporated in the material
Elemental analysis	Chemical composition of the material
Fourier transformed infrared spectroscopy	Characterization of functional groups
UV-Vis spectroscopy	Presence of chromophore organic groups
Energy dispersive X-ray spectroscopy	Chemical composition of the material

Regarding to the analysis of the structural properties of mesoporous materials, powder X-ray diffraction (PXRD) and transmission electron microscopy (TEM) techniques are normally used to study the integrity of the mesoporous network. PXRD is commonly used to identify the crystallographic symmetry of material phases at both the nano- and meso-scale. In the case of mesoporous materials, the regular arrangement of the pores produces reflections that are evidenced as signals at low diffraction angles. In the case of MCM-41-based materials, a typical X-ray diffractogram shows four peaks which can be indexed as the (100), (110), (200) and (210) Bragg peaks of a *P6mm* space group (Figure 9a). The analysis of the X-ray diffractograms together with the Bragg law allows the calculation of the main interplanar distance d_{100}, as well as the calculation of the unit cell value a_0 (see Figure 9b). As Figure 9 shows, a_0 represents the distance between the centres of two contiguous pores in that direction. By combining this value (a_0) with the pore diameter (Dp), from the analysis of nitrogen adsorption measurements, the wall thickness can be calculated (Wt).

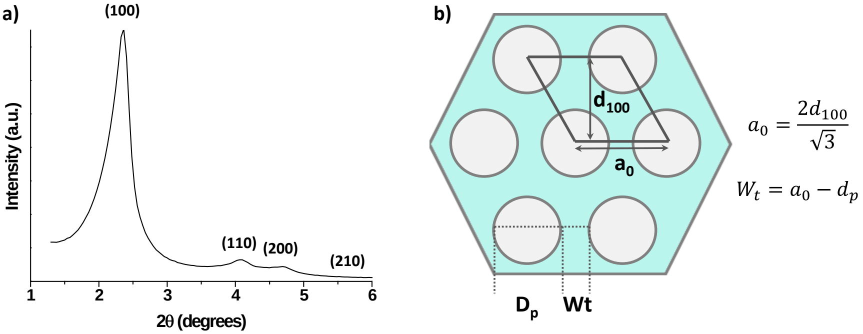

Figure 9. a) Powder small-angle X-ray pattern of MCM-41 material. b) Schematic illustration of a hexagonal structure with the d_{100} spacing and unit cell parameter a_0.

In addition, detailed analysis of pore order and symmetry at the meso-scale can be achieved by TEM image analysis. Two different examples of a) mesoporous MCM-41 material and b) silica-based nanomaterial with disordered pores are shown in Figure 10. As can be seen, the different mesophases can be clearly distinguished, the particle dimensions and morphology can be also evaluated by means of this technique. As a complement to the particle size study, dynamic light scattering (DLS) measurements are commonly performed. Furthermore, particle morphology can be also examined by scanning electron microscopy (SEM) sample analysis.

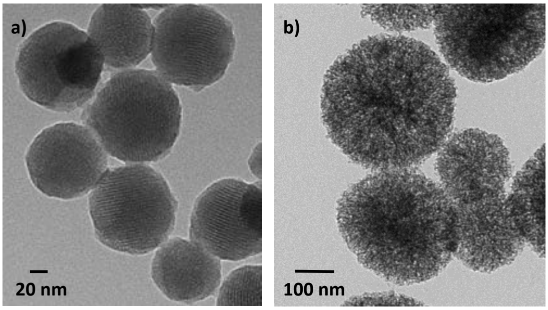

Figure 10. TEM images of MCM-41 nanoparticles a) and silica-based nanoparticles with a disordered distribution of mesopores b).

On the other hand, nitrogen adsorption is a complementary method used to obtain a comprehensive characterization of porous materials. Adsorption of nitrogen at various relative pressures on the porous matrix provides information about properties including surface area, pore volume, and pore size. According to the IUPAC classification, six types of isotherms can be distinguished.[65] Type IV isotherms are characteristic of mesoporous solids. This type of isotherms show an increase of the adsorbed amount of gas at intermediate relative pressures and occurs my means of a multilayer adsorption mechanism. Generally, the desorption of the adsorbed gas occurs at lower pressures, resulting in a hysteresis loop. These hysteresis loops have been also classified by the IUPAC in four types and it is widely accepted that there is a correlation between their shape and the textural properties of the material (i.e., pore size distribution, pore geometry and connectivity).[66] To determine the surface area of mesoporous systems, it is usually applied the Brunauer-Emmet-Teller (BET) method to the adsorption isotherm.[67] While the pore size distribution of the mesoporous material is commonly determined by applying the Barrett-Joyner Halenda (BJH) method to the nitrogen sorption isotherms.[68] Figure 11 shows a typical gas absorption isotherm of MCM-41 material and the pore size distribution.

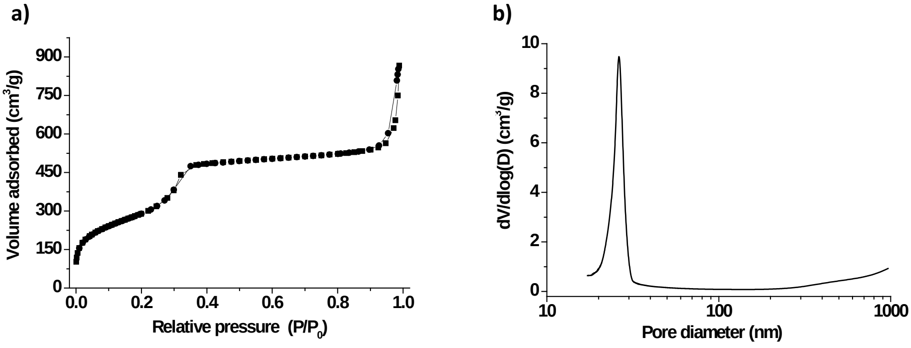

Figure 11. a) Typical N_2 adsorption Isotherm of MCM-41 material and b) pore size distribution.

Moreover, thermogravimetric (TGA) studies, elemental analysis (EA), Fourier transformed infrared spectroscopy (FT-IR) provide information of the organic-inorganic ratio of the hybrid material. In some cases, it is useful to combine these characterization methods with other techniques such as scanning electron microscopy coupled with energy dispersive X-ray spectroscopy (SEM/EDX) or UV-Vis spectroscopy.

1.4 Advanced Applications of Functional Organic-Inorganic Hybrid Supports: Gated Materials*

Among different inorganic or hybrid solids, much attention has been paid in recent years to porous materials in fundamental and applied research. One appealing concept in this fertile field is related with the design of gated materials. These gated materials are constructed for the purpose of finely tuning the movement of chemical or biochemical species from voids of porous supports to a solution, and vice versa, in response to a predefined stimulus.[69,70] By taking into account this concept, several research groups have been involved in the synthesis and characterization of imaginative nanodevices in which the delivery of a certain cargo stored in a container can be triggered by applying selected external stimulus. Such gated materials are composed mainly of two subunits: i) a porous inorganic support in which a cargo is loaded and ii) certain molecular or supramolecular entities, generally grafted onto the external surface, which can control mass transport from pores (see Figure 12).

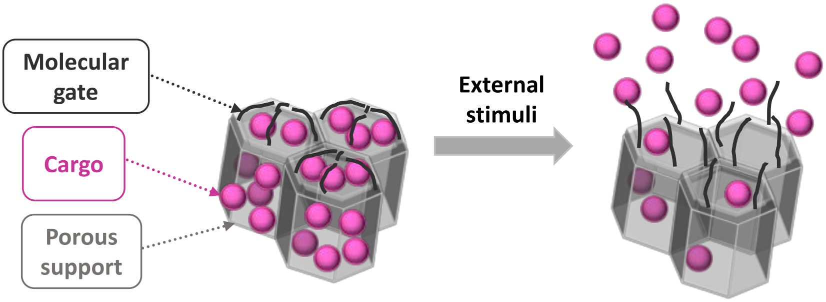

Figure 12. Schematic representation of the operation principle of a molecular gate. *Adapted from Chem. Rev. 2016, 116, 561. Copyright © 2016 American Chemical Society.*

---

* *Text fragments reproduced with permission of "Aznar, E.; Oroval, M.; Pascual, L.; Murguía, J. R.; Martínez-Máñez, R.; Sancenón, F. Gated Materials for On-Command Release of Guest Molecules. Chem. Rev., 2016, 116, 561." Copyright © 2016 American Chemical Society*

When dealing with the inorganic support, one of the most commonly used material for preparing gated nanodevices is mesoporous solids. As pointed in section 1.3, mesoporous supports can be prepared in different forms that range from micrometric to nanometric and have tailor-made pores (2–10 nm in diameter) and very large specific surface areas (up to 1200 m^2 g^{-1}).[71,72] Given these remarkable features, mesoporous materials have a huge loading capacity and can store not only small but also a wide variety of medium-sized molecules, such as proteins, oligonucleotides, and nucleic acids. These supports are also chemically inert under a wide range of conditions and are easily functionalized using well-known chemistries.[73–75]

Another key point when designing such gated nanodevices is the selection of gating entities. In line with this, imaginative molecular and supramolecular concepts have been developed to allow the controlled release of a wide range of entrapped cargos. There is a long list of clever approaches, where the driving force to switch gating mechanisms between an open state and a closed state take advantage of electrostatic or supramolecular interactions, the rupture/formation of covalent bonds, or changes in the physical properties of molecules or macromolecules.[76–84]

Gated nanochemistry has demonstrated the possibility of achieving new advanced predesigned functions by means of mass transport control. The most studied application of such systems is related with controlled release protocols, especially devoted to potential biomedical applications.[85–88] Such gated materials have also been used to develop new sensing/recognition protocols.[89] A few examples have also been reported for other applications. Nevertheless, many studies conducted to date are limited to the simple design of gated materials, and there are a number of potential applications still to be explored.

The application of gated materials in the biomedical field has been boosted in the past few years because these systems allow the release of one or several drugs upon the application of external stimuli and are promising candidates for developing new therapies to improve efficacy and safety. Moreover, anchoring biological receptors (e.g., antibodies, peptides, aptamers, or carbohydrates) onto an external surface allows targeted delivery of drugs to sites such as cells and tissues that contain overexpressed receptors.[90–99] In recent years, some more complicated architectures have been designed, mainly because of their possible application in the emerging area of "theranostic" devices.[100–105] In these systems, nanometer-sized porous inorganic supports are loaded with a therapeutic agent, a diagnostic marker, or with an indicator molecule. Then pores are closed with stimuli-responsive caps. Moreover, certain biological receptors are grafted onto the external surface for targeting purposes. These nanodevices are capable of targeting selected cells or tissues to avoid the premature degradation of the entrapped cargo and also facilitate the transfer of the payload across the cell membrane. The presence of markers also allows the release process and the accumulation of the gated nanodevice in target tissues to be traced in real time.

When dealing with the application of gated material in sensing/recognition protocols, the key point is to prepare systems capable of responding specifically to a certain target molecule which could modulate delivery of an indicator (e.g., dye or fluorophore).[106] The recognition protocol which uses these "gated materials" clearly differs from the classic supramolecular "binding site-signaling subunit" paradigm because it detaches the recognition event from the signaling step.[107] This makes signaling independent of the host–guest stoichiometry and sometimes allows signal amplification.[108] Additionally, the approach is highly flexible given the possible selection of different porous supports, distinct selective binding sites, and a wide range of indicator molecules.

Bearing in mind all the above cited, it can be assumed that gated nanochemistry is a highly topical and rapidly developing tool. [109–114] The following sections of this general introduction are devoted to illustrate some examples of relevant gated materials, selected according to their applications and in relation with the contextual framework of the present PhD thesis.

1.4.1 Gated nanomaterials for sensing applications

Despite being in its infancy, the application of hybrid organic inorganic nanomaterials has shown great promise in achieving high sensitivity and specificity in recognition assays, which are difficult to achieve by conventional methods.[106] Within this background, the use of DNA provide a broad range of opportunities in the construction of nanoscale systems for their application in molecular recognition.[78] Indeed, there are a variety of systems that take advantage of the hybridization of linear DNA for different applications including oligonucleotide sensing, multiplexed pathogen detection and aptameric diagnostics.[115,116,117,118] In this scenario, the use of nucleic acids as caps in gated nanosystems with sensing purposes is a highly topical field.[90,119,120]

From another point of view, enzymatic methods are broadly used in bioanalytical chemistry in order to determine either the enzyme itself or its substrate.[121] The use of enzymes for different applications relies on their specificity for a certain substrate. In this context, the use of enzymes in the design of gated supports is a field of interest.

The next sections show several examples of DNA-capped, DNAzyme-capped, aptamer-capped and enzyme-capped mesoporous silica nanoparticles (MSNs) able to release an entrapped reporter in the presence of a target analyte.

1.4.1.1 Oligonucleotide-capped MSNs

Within recent decades, there has been considerable interest in using hybrid nanoparticles consisting of oligonucleotides covalently or electrostatically tethered to nanoparticles as a tool for molecular diagnostics.[115,122] The immobilization of DNA includes the selection of a suitable substrate such as glass,[123] silicon,[124] glassy carbon[125] or gold[126] to which DNA is attached by physical adsorption[127] or covalent immobilization.[128] In these systems, the DNA hybridization is used to induce changes in the state of DNA nanodevices.

In the area of capped mesoporous silica supports the design of systems able to be opened in the presence of cations are relatively scarce. In a recent work Tan, Zhang, and co-workers designed a Hg^{2+} probe based on oligonucleotide-capped mesoporous silica nanoparticles (MSNs). The authors loaded MSNs with rhodamine 6G (Rh 6G) and functionalized the surface with isocyanate groups, which reacted with an amino-modified oligonucleotide.[129] Moreover, a second larger oligonucleotide complementary to the anchored one at the terminal parts was hybridized capping the pores of the MSNs as depicted in Figure 13. This second oligonucleotide strand was highly rich in thymines and displayed a high affinity to Hg^{2+}. In the presence of this cation, the strand was displaced from the surface resulting in dye delivery. The system was able to detect Hg^{2+} in water with a limit of detection (LOD) of 4 ppb. In addition, no important cargo release was observed in the presence of other cations such as Ni^{2+}, Pd^{2+}, Fe^{2+}, Fe^{3+}, Ba^{2+}, Zn^{2+}, Ca^{2+}, Mg^{2+}, Cu^{2+}, Co^{2+}, and Cd^{2+}.

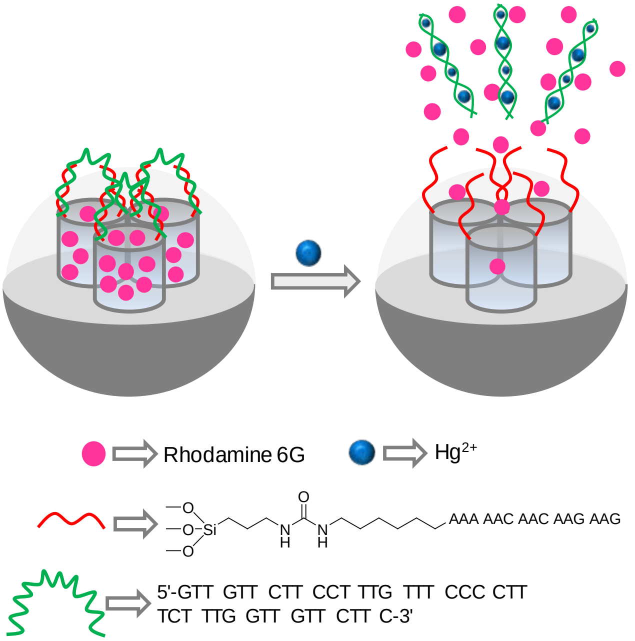

Figure 13. DNA-capped MSNs loaded with Rh 6G for the optical detection of Hg^{2+} cation.

A first example of uncapping protocol triggered by biomolecules, in particular by a certain oligonucleotide, was reported by Martínez-Máñez *et al.*[130] The system was based on MSNs loaded with fluorescein and functionalized with (3-

aminopropyl)triethoxysilane (APTES) in the outer surface. The oligonucleotide 5′-AAT GCT AGC TAA TCA ATC GGG-3′ was used to cap the pores through electrostatic interactions with the amines at the surface that were partially protonated at neutral pH. Cargo delivery was triggered in the presence of the complementary single strand of the capping oligonucleotide as consequence of the hybridization of both single oligonucleotides and detachment from the nanoparticles' surface as shown in Figure 14 a. Dye delivery was also studied in the presence of other oligonucleotides, yet in all cases a poor cargo delivery was found.

Based on an analogous design, the same authors prepared capped materials for the detection of genomic DNA.[131] For this purpose, MSNs were loaded with rhodamine B (Rh B) and functionalized with APTES on the external surface. In this case, it was used as the capping oligonucleotide a sequence highly conserved in the *Mycoplasma* genome that corresponds to a fragment of the 16S ribosomal RNA subunit. The system displayed no dye delivery until the addition of *Mycoplasma fermentans* genomic DNA (Figure 14 b). No cargo delivery was observed in the presence of genomic DNA from other bacteria such as *Candida albicans* or *Legionella pneumophilla*. A LOD as low as *ca.* 70 DNA copies μL^{-1} was found. The capped nanoparticles were used to detect *Mycoplasma* in real contaminated cell-culture media without the use of PCR techniques. In a more recent work, the same authors developed a similar system for the detection of genomic DNA using in this case nanoparticles loaded with Rh B and capped with covalently attached DNA.[132] Two single stranded oligonucleotides were selected for the gating mechanism; i) a short DNA sequence (NH_2-$(CH_2)_6$-5'-GAC TAC GAC GGT ATC-3') that was covalently anchored to the loaded scaffold via the formation of urea bonds and ii) a single stranded oligonucleotide selective for *Mycoplasma* (i.e. 5'-AAG CGT GGG GAG CAA ACA GGA TTA GAT ACC CTG GTA GTC-3'). The probe was able to detect *Mycoplasma fermentans* genomic DNA at a concentration as low as 70 DNA copies μL^{-1}. The authors also found that *Candida albicans* and *Legionella pneumophilla* genomic DNA were unable to induce dye release.

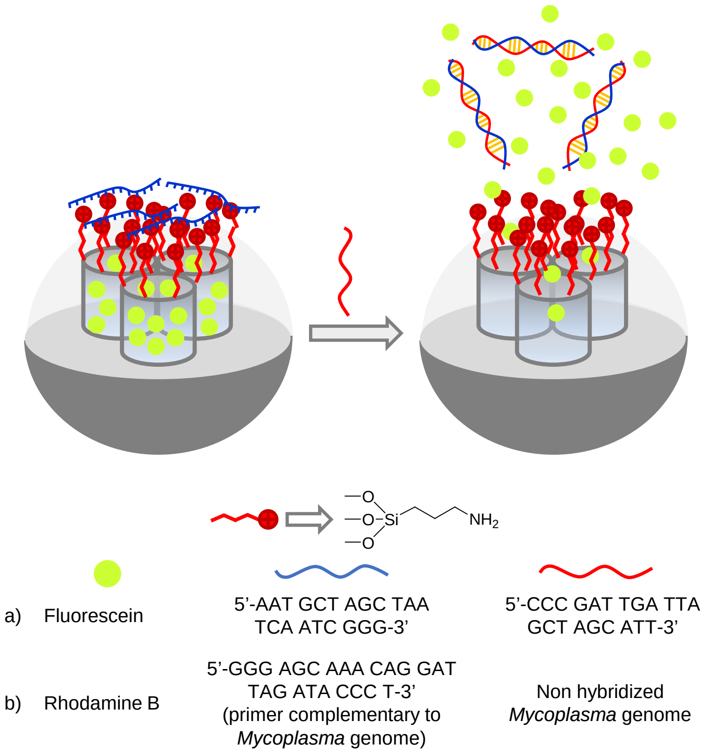

Figure 14. MSNs loaded with fluorescein or Rh B, functionalized with aminopropyl moieties, and capped with a single-strand DNA. The pores were opened upon addition of the complementary strand or *Mycoplasma fermentans* genomic DNA.

Ren, Qu, and co-workers[133] developed a new example of logic gates by building a system based on MSNs capped with long duplex DNA structures in a cascade manner. To construct such a system, bare MSNs were functionalized with APTES and amino moieties were further reacted with succinic anhydride to obtain carboxylated-MSNs. Then an amine-modified oligonucleotide (5′-GTGTT TATAG CGGAC CCC-NH_2-3′) was grafted onto the external surface of MSNs through an amide bond by the EDC/NHS coupling method, followed by loading mesopores with dye Rh B. Finally, pores were capped by adding three different oligonucleotides, which had short complementary regions among them (5′-GAA GAC TCG TAA TGT GAA ACC G-3′, 5′-CAC AT T ACG AGT CTT CGT GGC ATA TCA CTC TTG GAG-3′, 5′-GGG GTC CGC TTA AAC ACC TCC AAG AGT GAT ATG CCA C-3′) and formed a long duplex DNA structure by hybridization with the oligonucleotide grafted onto the surface of MSNs. Cargo release was triggered by DNA strand displacement by adding complementary oligonucleotides to those that capped the pores in sequence. The system’s logic response was studied by adding different input combinations of complementary DNA strands to the three capping oligonucleotides. The experimental results reflected that only the addition of the complementary oligonucleotides in sequence to the oligonucleotides that formed the long duplex DNA structure was able to open pores and release cargo. Conversely, a low dye release was observed when other input combinations were used.

Willner and co-workers prepared different DNA-capped MSNs able to be opened in the presence of certain biomarkers.[134] MSNs were functionalized with aminopropyl moieties and the amino groups in the surface were used for grafting selected single-stranded DNA sequences using sulfo-EMCS as a covalent cross-linker. In the first material (see Figure 15 a), the DNA-1 sequence was anchored. DNA-1 contained a tailored base sequence that generated at room temperature a hairpin structure that blocked the pore entrances. DNA-1 also included a single-stranded loop for the recognition of a nucleic acid biomarker (i.e., 5′-AGT GTG CAA GGG CAG TGA AGA CTT GAT TGT-3′). The pores were loaded with Rh B. Treatment of the DNA-1-capped MSNs with the biomarker induced the opening of the hairpin forming a duplex structure that also blocked the pores inhibiting dye release. Addition of Exo III enzyme induced the hydrolysis of the 3′-end of 1, allowing the release of the entrapped Rh B and the biomarker which induced the opening of additional capped pores. The same approach was used by grafting the single-stranded DNA sequence 2 and as biomarker 5′-ATC CTC AGC TTC G-3′ (see Figure 15 b). Both DNA formed a duplex structure that was able to cap the pores and inhibit dye release. In this case, the duplex included a programmed sequence for the specific nicking of one base. Upon addition of the Nb.BbvCl enzyme, the duplex was dissociated because of the nicking of the grafted DNA strand that resulted in the release of the biomarker and the entrapped Rh B. Another gated material was obtained by the grafting sequence DNA-3, which formed a hairpin structure, and that incorporated an ATP-aptamer conjugated with other sequence that ensured that Exo III enzyme was unable to hydrolyze (see Figure 15 c). Upon addition of ATP, the hairpin formed by DNA-3 opened and the 3′ end formed a duplex structure with the 5′ domain that was hydrolyzed by Exo III. This hydrolysis induced the release of the entrapped dye and ATP, which induced the opening of additional gated pores. The same methodology was used to prepare a material able to release the entrapped dye and ATP by grafting DNA-4, which contained an ATP-aptamer and a fragment able to be hydrolyzed by the Nb.BbvCl enzyme (see Figure 15 d).

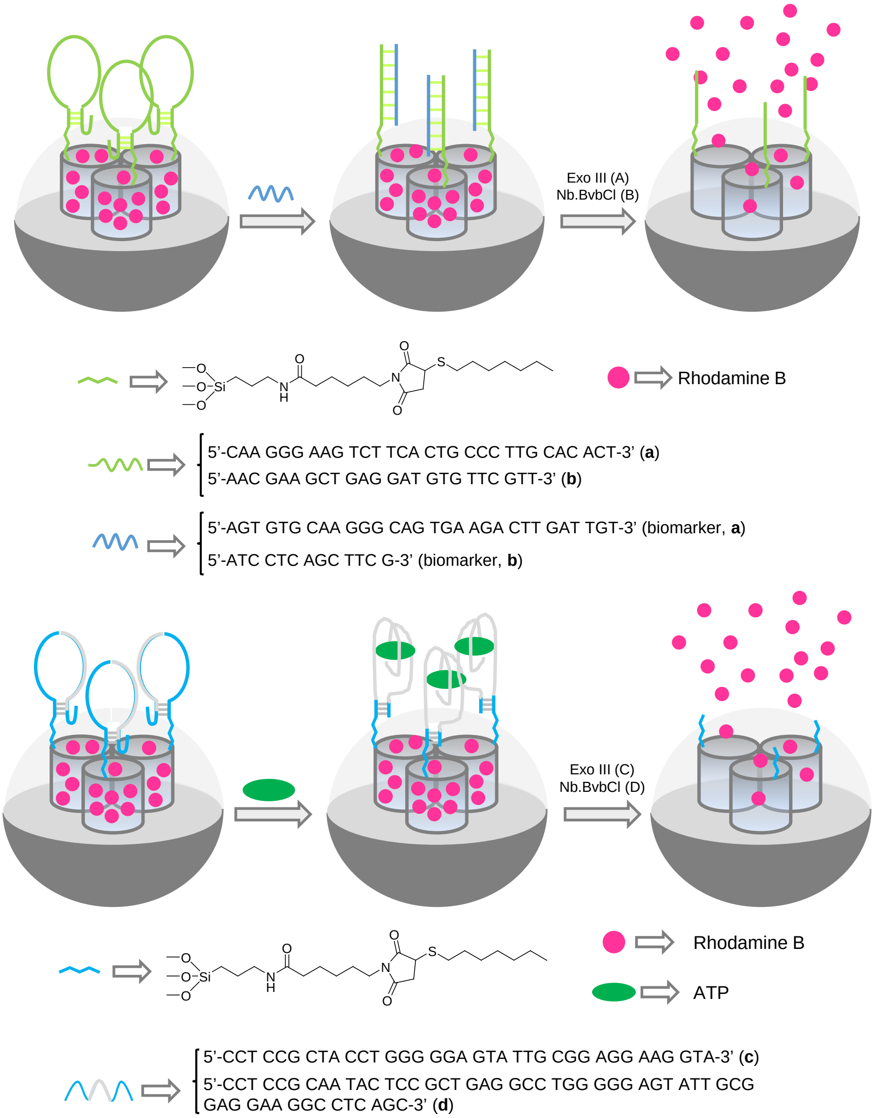

Figure 15. MSNs loaded with Rh B and capped with different DNA sequences that were opened with (a and b) certain biomarkers, (c and d) ATP, and (a, b, c, and d) enzymes.

He, Wang, and co-workers combined the catalytic properties of platinum nanoparticles (PtNPs) and capped MSNs to design a colorimetric detection system for oligonucleotides.[135] PtNPs were coated with a mesoporous silica shell, and the final gated system was prepared by functionalization of the silica shell with aminopropyl moieties and capping the pores through electrostatic interactions with a single oligonucleotide strand which contained a mutation of gene BRCA1 related with breast cancer (see Figure 16). Aqueous suspensions at pH 4.7 of the capped nanoparticles in the presence of TMB remained colorless because the molecules of the indicator were unable to access the Pt core. In contrast, in the presence of the complementary strand, a clear blue color was observed due to the displacement of the capping oligonucleotide and Pt-induced catalytic oxidation of TMB. A LOD of 3 nM was calculated. Additionally, other strands with 1, 2, or 3 mismatched bases induced no color changes.

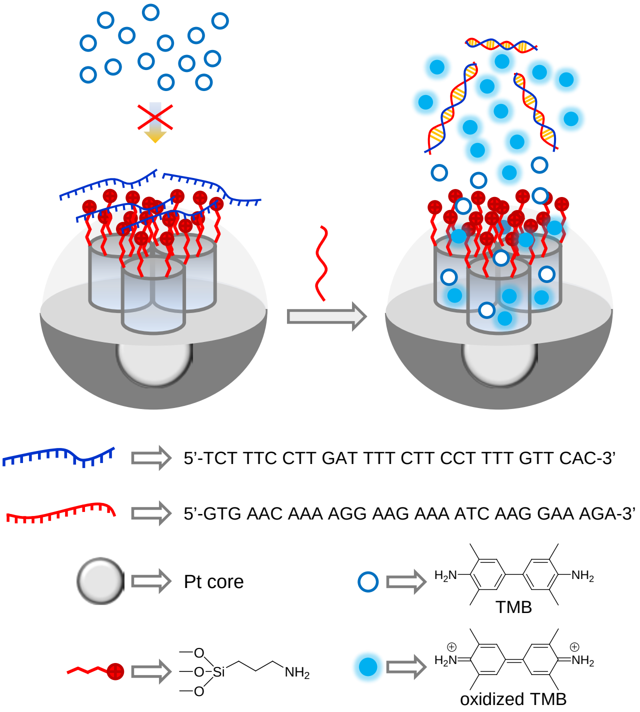

Figure 16. PtNPs coated with a silica mesoporous shell in which the pores were capped with a single DNA strand for the detection of the complementary strand.

Optical detection methods are generally used in these systems however, it is possible to find in the literature some examples in which electrochemical detection methods are used. As an example, DNA-capped MSNs have been used for the optical and electrochemical detection of the glycoprotein enzyme prostate specific antigen (PSA).[136] MSNs were functionalized with aminopropyl groups, the pores loaded with methylene blue (MB) and finally the pores capped upon addition of a single DNA strand through electrostatic interactions with the positively charged nanoparticle's surface. Moreover two antibodies, able to coordinate PSA, were labeled with two single-stranded DNA fragments (i.e., DNA1 and DNA2), which were complementary to that used for capping the MSNs (see Figure 17). In the presence of both DNA-labeled antibodies and PSA, a proximate complex was formed that hybridized with the single-stranded DNA used as a cap, resulting in MB release. Cargo delivery was measured through fluorescence or differential pulse voltammetry. PSA was detected with a linear range from 0.002 to 100 ng mL^{-1}, and a LOD of 1.3 pg mL^{-1} was determined. No interference was found in the detection of PSA when the carcinoembryonic antigen (CEA) was present in the solution.

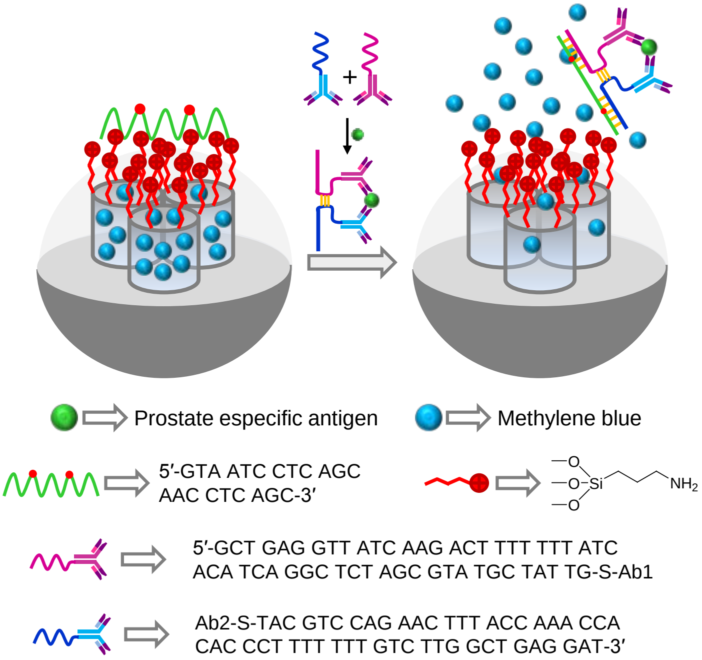

Figure 17. MSNs loaded with methylene blue and capped with a single DNA strand for the detection of prostate-specific antigen.

1.4.1.2 DNAzyme-capped MSNs

Another emerging methodology for the construction of gated MSNs-based systems for sensing applications, involves the use of DNAzymes as caps.[137] DNAzymes are DNA sequences with catalytic activity such as cleavage, ligation or phosphorylation.[138,139] Frequently these DNAzymes make use of a metal-ion cofactor in order to carry out their functions, and based on this requirement, these catalytic nucleic acids offer great promise in the development of metal-ion sensors.[140,141] In this way, some groups have developed DNAzyme-based MSNs systems that may be used for the detection of a wide range of metal ions.

Willner and co-workers reported the design of DNAzyme-capped MSNs, which were opened by the cooperative effect due to the presence of the cations Mg^{2+} and Zn^{2+}. The authors functionalized MSNs with two different thiolated single strands of DNA, using N-ε-maleimidicaproyl-oxosulfosuccinimide ester as a cross-linker, resulting in two different solids, one for Mg^{2+} and the other for Zn^{2+}.[142] Each DNA strand contained the specific sequence of basis for the respective Mg^{2+}-dependent DNAzyme and Zn^{2+}-dependent DNAzyme hydrolysis process. The DNAzyme hydrolyses a specific sequence of DNA only in the presence of a certain cation (Mg^{2+} or Zn^{2+} in this case) due to the complex formed by the cation and the particular region of the DNA (see Figure 18). Then DNA-functionalized solids were loaded with MB or thionine and were capped using the corresponding complementary DNA sequence. Both system presented release of the selected dye in the presence of the corresponding cation (Mg^{2+} or Zn^{2+}). The authors found this process selective, and no delivery was observed in the presence of other divalent cations. Furthermore, the inclusion in the DNA sequence of adenosine triphosphate (ATP)-aptamers or Hg^{2+}-depending domains was also studied. The incorporation of these foreign sequences disturbed the formation of the complexes of DNA with Mg^{2+} or Zn^{2+} due to the major flexibility of the strand. In this case, the formation of the aptamer-ATP complex or the metal ion-nucleic acid bridge (thymine-Hg^{2+}-thymine) was a required previous step to the system to form the corresponding complexes with Mg^{2+} or Zn^{2+} and finally restore the biocatalytic activity of the DNA-depending enzyme (see Figure 18). These result in systems that need two different and complementary stimuli (ATP and Mg^{2+} or $Hg^{2+}$and Zn^{2+}) to achieve the cargo release. The authors analyzed as a model system the Mg^{2+}-induced release of the anticancer drug doxorubicin (DOX), and the ATP cooperative synergetic Mg^{2+}-opening of the pores. DOX entrapped in the pores of the nanomaterial was not released by ATP alone, was inefficiently released by only Mg^{2+} ions, and efficiently released by the addition of ATP and Mg^{2+} ions.

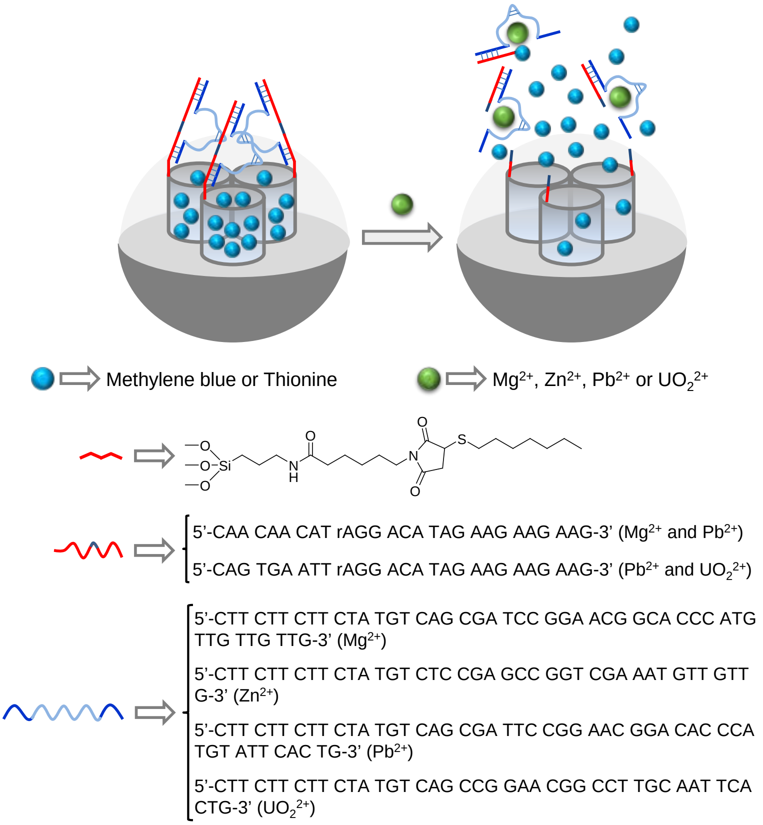

Figure 18. MSNs capped with DNAzymes for the selective detection of Mg^{2+}, Zn^{2+}, Pb^{2+}, and UO_2^{2+} cations.

DNAzymes were also used as caps by Willner *et al.* for the preparation of gated MSNs that were opened in the presence of Mg^{2+} and UO_2^{2+}cations.[143] For the preparation of the Mg^{2+}-selective capped material, MSNs were selected and were functionalized with aminopropyl moieties, and then the amino groups reacted with a cross-linker agent that yielded maleimide moieties in the external surface. Afterward, a thiolated ribonuclease, containing two complementary single-stranded DNA sequences of Mg^{2+}-dependent DNAzyme, were linked into the external surface. In order to prepare the final material, the pores of the inorganic scaffold were loaded with MB and then capped by the addition of a Mg^{2+}-dependent DNAzyme sequence through hybridization with the previously linked oligonucleotide (see Figure 18). Aqueous suspensions of the capped nanoparticles showed negligible MB delivery, whereas in the presence of the Mg^{2+} cation, a remarkable dye release was observed. Delivery was attributed to a coordination of the Mg^{2+} cation with the linked DNAzyme that induced the cleavage of the caps. The optical response was selective, and the authors found that other divalent cations such as Zn^{2+}, Pb^{2+}, Ca^{2+}, Sr^{2+}, Ba^{2+}, Cu^{2+}, Co^{2+}, Mn^{2+}, Ni^{2+}, Fe^{2+}, and Hg^{2+} were unable to induce dye release. The same experimental procedure was used for the preparation of the UO_2^{2+}-selective capped material but using as loading molecule thionine instead of MB and capping the pores with the corresponding UO_2^{2+}-dependent DNAzyme sequence.

A similar approach was used by Tang and co-workers that also used DNAzyme-capped MSNs that were selectively opened in the presence of the Pb^{2+} cation.[144] MSNs were selected as inorganic support, and the external surface was functionalized with (3-glycidyloxypropyl)trimethoxysilane (GTPMS). Then, using an epoxy-amino reaction, the Pb^{2+}-DNAzyme was anchored and the pores of the support were loaded with glucose (see Figure 19). Finally, the pores were capped by the addition of a single-stranded DNA sequence that hybridized with the grafted DNAzyme sequence. Aqueous suspensions of the capped nanoparticles showed negligible glucose release, whereas in the presence of Pb^{2+}, a remarkable release of glucose was observed. Glucose delivery was measured using a personal glucometer. Cargo delivery was related to the cleavage of the caps upon Pb^{2+} coordination with the linked DNAzyme. The authors found that other metal cations such as Cu^{2+}, Co^{2+}, Cd^{2+}, Mg^{2+}, Zn^{2+}, Fe^{3+}, Ag^{+}, and Hg^{2+} were unable to induce glucose release.

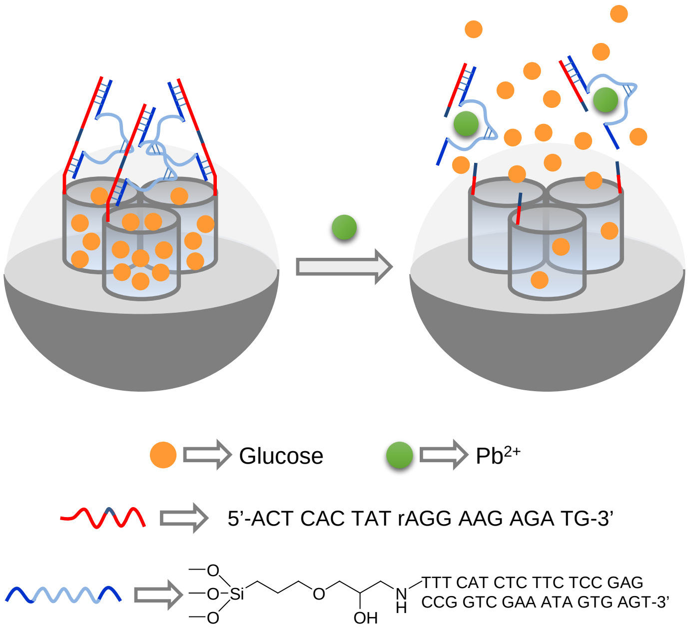

Figure 19. Nanometric silica mesoporous support loaded with glucose and capped with DNAzyme for the detection of Pb^{2+} cations.

1.4.1.3 Aptamer-capped MSNs

Aptamers are artificial specific oligonucleotides (DNA or RNA) with the ability to bind to non-nucleic acid target molecules, such as peptides, proteins, drugs, organic and inorganic molecules and even whole cells, with high affinity and specificity.[145–147] These special nucleic acid ligands have shown affinity for their targets comparable to than their monoclonal antibody counterparts, with K_d values in the picomolar range achieved.[148,149] The considerable affinity and specificity for their targets endows aptamers as a powerful tools for diagnostic applications. As a result, there has been much interest in developing aptamer-based diagnosis systems.[150–152] This section presents an outline of aptamer-based MSNs systems with sensing purposes, consisting on ligand-induced conformational changes.

An example of this was reported by Ozalp and co-workers that used ATP-aptamers to develop gated materials.[153] In their work, they used an aminoterminated oligonucleotide sequence that contained both an ATP-aptamer and a short extra sequence which was used to induce a hairpin-like structure that blocked the pores (see Figure 20). MSNs were loaded with fluorescein and functionalized in the external surface with sulfhydryl groups. The amino functionalized aptamer was then covalently anchored to the nanoparticles using the cross-linker sulfo-*N*-succinimidyl 4-maleimidobutyrate. The hairpin structure of the aptamer blocked the pores while the presence of ATP triggered the delivery of the entrapped dye. This was explained due to ATP binding that resulted in a conformational change from a duplex to a single-stranded DNA of the aptamer sequence that was close to the surface of the MSNs. Interestingly, similar nanoparticles capped with a mutated hairpin did not respond to ATP, and guanosine 5'-triphosphate (GTP) was also unable to induce dye release. In a further work, the same authors extended their studies and monitored the performance of aptamer-gated MSNs using circular dichroism.[154]

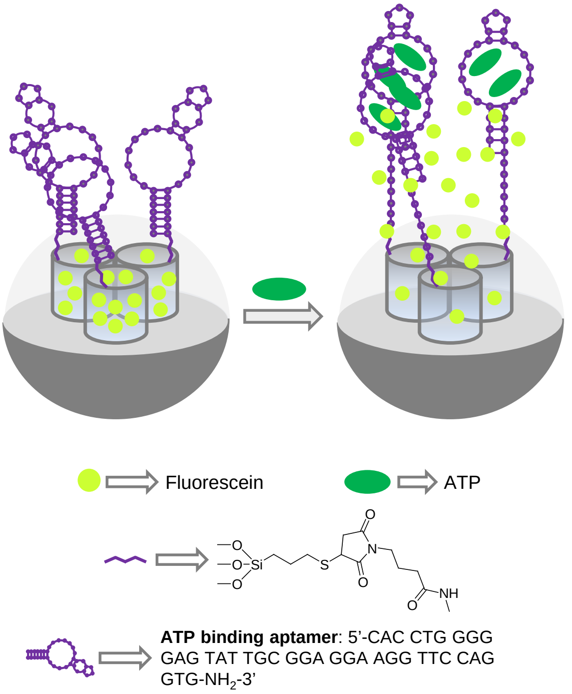

Figure 20. Aptamer-gated MSNs loaded with fluorescein and for the detection of ATP.

Wang and co-workers also designed ATP-selective delivery systems with MSNs, employing the same ATP-aptamer used by Ozalp *et al.* but based on a different configuration of the gated ensemble.[155] The authors functionalized MSNs with 3-cloropropyltrimethoxysilane and transformed the chloride atoms into azide groups by reaction with NaN_3. Moreover, the ATP aptamer was hybridized with two different single-stranded DNA (ssDNA) sequences yielding a sandwich type DNA structure. The pores of the inorganic scaffold, functionalized with azide moieties, were loaded with $Ru(bipy)_3^{2+}$, and then the system was capped with the sandwich-type DNA structure containing the ATP aptamer sequence, using a click chemistry reaction between the azide moiety in the solid and the alkyne group in the DNA ensemble. This blocked the pores. In the presence of ATP, dye release was observed and attributed to the competitive displacement of the ATP aptamer from the sandwich-type DNA. The system was selective and cytosine 5′-triphosphate (CTP), GTP, and uridine 5′-triphosphate (UTP) at 20 mM were unable to induce dye delivery.

Wang and co-workers also developed an ATP-capped material using, in this case, aptamer-containing gold nanoparticles (AuNPs) as caps.[156] In particular, the authors functionalized with amino groups the surface of MSNs and anchored adenosine-5′-carboxylic acid moieties via an amidation reaction. The pores were loaded with fluorescein isothiocyanate (FITC). Moreover the authors prepared AuNPs containing the ATP aptamer by forming an Au–S bond. The gated material was then finally prepared by capping the pores of the mesoporous silica support with the aptamer-functionalized AuNPs. Aqueous suspensions of the capped MSNs displayed negligible cargo delivery while in the presence of ATP, FITC release was observed which was proportional to the ATP concentration. The uncapping process was ascribed to a competitive displacement reaction of the AuNPs upon ATP coordination with the grafted aptamer. Other ATP analogues, such as CTP, GTP, and UTP, induced no cargo delivery.

Tang and co-workers also designed MSNs capped with AuNPs for the detection of ATP using the same ATP aptamer used above by Ozalp, Wang, and Yang.[157] The authors functionalized MSNs with aminopropyl groups and linked to the amino moieties a single-stranded oligonucleotide (DNA1) using glutaraldehyde as a linker. The pores of the MSNs were loaded with glucose. On the other hand, AuNPs coated with another single-stranded olgonucleotide (DNA2) were prepared (see Figure 21). Both DNA1 and DNA2 were complementary to adjacent areas of the ATP aptamer. In the presence of the ATP aptamer, DNA1 and DNA2 hybridized forming a three-stranded complex that resulted in pore capping. The gated nanoparticles showed no release of the entrapped glucose at neutral pH, whereas in the presence of ATP, release of glucose was detected. Glucose delivery was detected with a commercially available glucometer. Cargo delivery was attributed to the binding of ATP with the aptamer that resulted in the separation of the AuNPs from the MSNs. This material was used to sense ATP which was detected at a concentration as low as 8 µM. The presence of other nucleotides such as CTP, GTP, and UTP induced no cargo delivery. The authors also used a similar approach for the detection of cocaine, employing in this case, a cocaine aptamer.

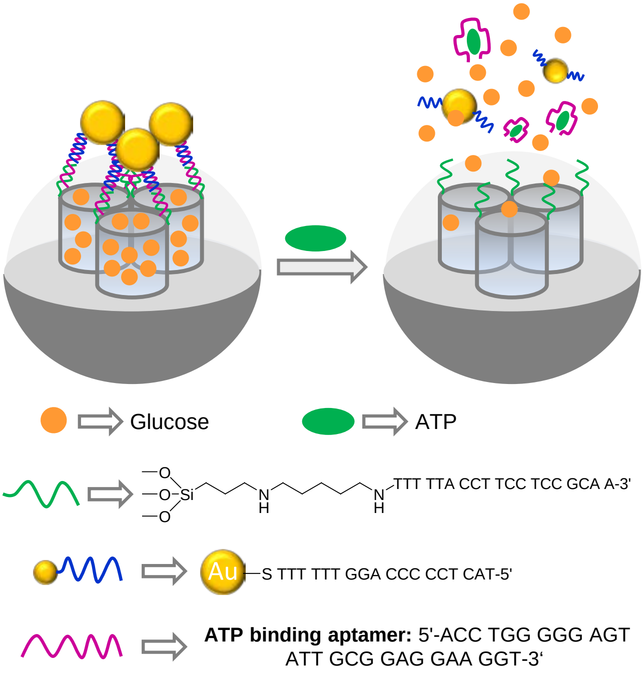

Figure 21. MSNs loaded with glucose and capped with ATP aptamer and AuNPs for the detection of ATP.

On the other hand, aptamer-capped MSNs designed to be opened in the presence of cations are relatively scarce. For instance, Wen, Song, and co-workers developed silica mesoporous supports capped with a K^+-selective aptamer and demonstrated that cargo delivery was achieved in the presence of this cation.[158] For this purpose, mesoporous silica microparticles were functionalized with aminopropyl moieties and the amino groups further reacted with succinic anhydride to prepare a carboxylate covered material. An amino-functionalized K^+-selective aptamer was grafted to the silica surface by the formation of an amide bond (see Figure 22). The pores were loaded with Rh B and capped upon addition of AuNPs coated with the oligonucleotide 5′-(DTPA) TAT TTA TAC GGG TTA GGG TTA GGG TTA GGG TTT TTT TTT TTT TTT TTT TT-3′ which contained the K^+ aptamer (DTPA: 1,2-dithiane-4-O-dimethoxytrityl-5-(2-cyanoethyl)-*N*,*N*-diisopropyl]-phosphoramidite). Aqueous suspensions of the capped microparticles showed nearly "zero release" in the absence of K^+, whereas when this cation was present in the solution a marked delivery of the entrapped Rh B dye was observed. This release was ascribed to the fact that the single-strand DNA, which coated the AuNPs, self-assembled into a G-quadruplex structure in the presence of K^+ cation with the subsequent detachment from the microparticles' surface.

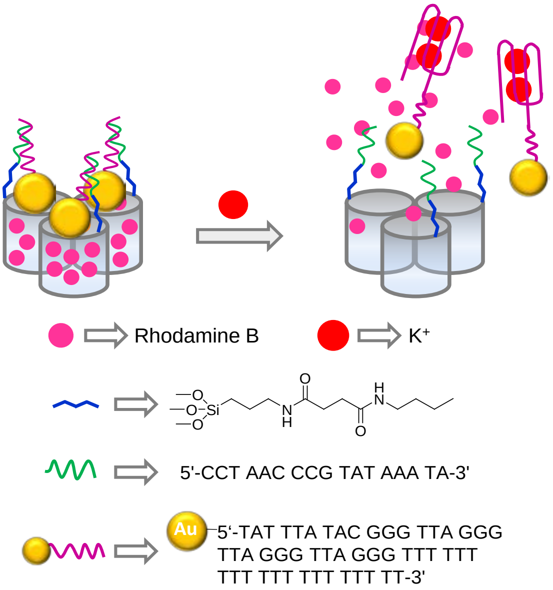

Figure 22. Mesoporous silica microparticles loaded with Rh B and capped with AuNPs coated with a K^+-aptamer for the sensing of K^+.

On the other hand, Wen and co-workers prepared AuNPs-aptamer-capped MSNs for the detection of adenosine.[159] The authors functionalized MSNs with 3-aminopropyl moieties, and the amino groups were transformed to carboxylic acids by reaction with succinic anhydride. Then, the single-stranded DNA sequence 3′-NH_2C_6-TCT CTT GGA CCC CCT-5′ was grafted in the outer surface by an amidation reaction. The pores of the hybrid material were loaded with Rh B, and the system was capped with AuNPs functionalized with a complementary aptamer for adenosine as depicted in Figure 23. The capped MSNs showed negligible dye release in water, whereas the addition of adenosine induced delivery of the entrapped Rh B due to the formation of aptamer-adenosine complexes that detached the AuNPs from the surface of the silica support. No Rh B delivery was observed upon the addition of cytidine, guanosine, and uridine.

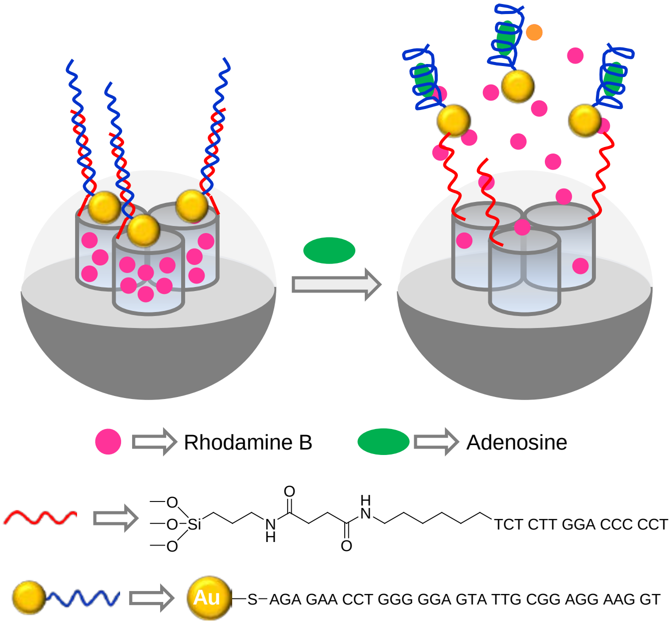

Figure 23. MSNs loaded with Rh B and capped with adenosine aptamer AuNPs for the detection of adenosine.

Ju and co-workers reported a telomerase-responsive gated system for sensitive in situ tracking of telomerase activity in living cells, which can be used to distinguish cancer cells from normal cells.[160] In their work, the authors prepared MSNs, which were functionalized with a fluorescence quencher in inner pores which were additionally loaded with fluorescein (see Figure 24). Nanoparticles were functionalized with amino groups on the external surface, and the system was capped with a DNA sequence that contained a telomerase primer. In the presence of telomerase and deoxy-nucleoside triphosphate (dNTPs) monomers, the oligonucleotide sequence was extended, and it formed a rigid hairpin-like DNA structure that moved away from the silica surface to allow the release of the entrapped cargo. The telomerase-driven response was studied by incubating the enzyme, dNTPs, and capped MSNs, and the fluorescein release by fluorescence and UV–vis spectroscopy was monitored. A gradual increase in fluorescein intensity with increasing incubation times was observed, which demonstrated the telomerase-induced cargo release. These authors also performed an extended i*n vitro* study on the gated material using HeLa cells and concluded that fluorescein release was activated by the action of intracellular telomerase. They suggested that these nanoparticles could be used for tracking intracellular telomerase activity. Moreover telomerase activity was proved using different model drugs, such as telomerase sense oligodeoxynucleotide, telomerase antisense oligodeoxynucleotide, and epigallocatechingallate. The authors also performed different assays with other cell lines, such as BEL-7402 cells (liver cancer cells) and QSG-7701 cells (liver normal cells), which confirmed that the designed strategy can be applied to distinguish cancer cells from normal cells. With a similar approach, Lu and co-workers used the same gated design, but they loaded MSNs with glucose to monitor telomerase activity with a glucometer.[161] In this case, the linear dependence between the glucometer readout and the number of HeLa cells used in the experiment was achieved within the 100–5000 cells range. The limit of detection was set at 80 HeLa cells mL^{-1}. Cui and co-workers also prepared a similar system, but in this case, they used Au@Ag nanorods coated with mesoporous silica and loaded with DOX.[162] These authors also demonstrated the telomerase-induced release of the loaded drug, and they traced the uptake of nanoparticles in HeLa cells by Surface Enhanced Raman Spectroscopy (SERS).

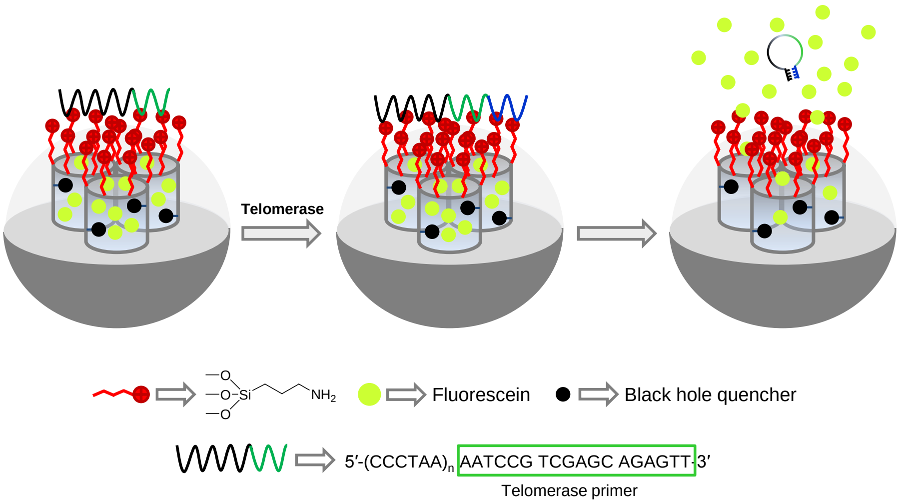

Figure 24. MSNs support capped with DNA for the detection of telomerase activity.

1.4.1.4 Enzyme-capped MSNs

Among the large number of enzymes that occur in living organisms, several have proved to be powerful tools for bioanalytical purposes and also for designing enzyme biosensors. The broad application of these biocatalysts can be ascribed to several considerations, for instance: the higher catalytic power compared to non-biological catalyst, the high degree of selectivity for a specific substrate or group of substrates and the fact that some biocatalysts can work in organic media.[163–165] It is not therefore surprising that the development of MSNs-enzyme sensing systems has resulted an attractive field to researchers in the last decade.

In this area Ren *et al.* prepared MSNs, which were covalently functionalized with cofactor flavin adenine dinucleotide (FAD).[166] Deflavined glucose oxidase (GOx) was then immobilized on the surface via interaction with FAD. Nanoparticles were loaded with Rh B. In the presence of protease K, clear dye delivery was achieved due to the proteolytic digestion of GOx caps as depicted in Figure 25. Concentration-dependent studies demonstrated that the release rate was related with the amount of added protease and was, therefore, associated with enzyme activity. Two more proteases (trypsin and chymotripsin) were also studied by the authors, and the results correlated with the expected activity due to the accessible cleavage sites in GOx for each protease. Dye delivery was also studied in the presence of protease inhibitors phenymethyl-sulfonylfluoride and Hg^{2+}, and no release was observed. The authors suggested that this protocol could be applied as a simple fast probe to evaluate protease activity and to screen its inhibitors.

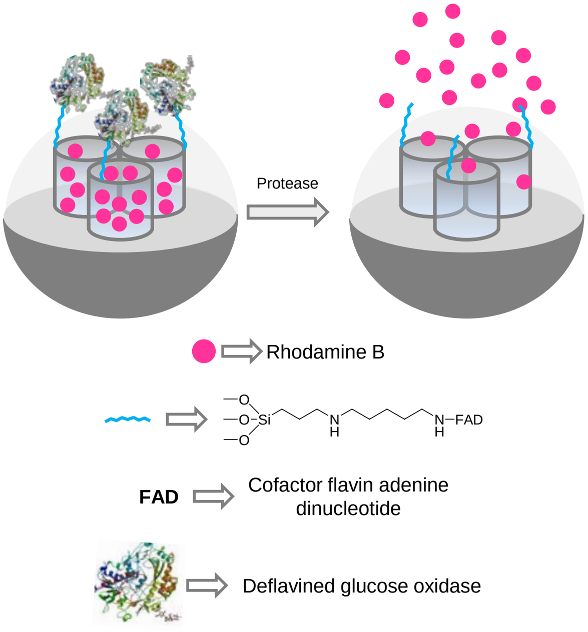

Figure 25. Protease-induced controlled release of Rh B from deflavined GOx-capped MSNs.

Lu and co-workers developed gated MSNs that were able to deliver an entrapped cargo in the presence of glucose.[167] MSNs were functionalized with prop-2-yn-1-yl(3-(triethoxysilyl)propyl)carbamate, and then the inhibitor D-(+)-glucosamine was grafted through a click chemistry reaction. The pores were loaded with Rh B and capped by the addition of the GOx enzyme through the formation of a complex with the grafted inhibitor, as depicted in Figure 26. Aqueous suspensions of the capped material showed negligible cargo release, whereas the presence of glucose induced a clear dye release. The observed delivery was proportional to the amount of glucose added, and it was a consequence of a displacement reaction of the GOx due to the presence of the glucose substrate. Cargo delivery in the presence of glucose was selective, and the authors confirmed that other monosaccharides tested (i.e., fructose, mannose, and galactose) induced no payload release.

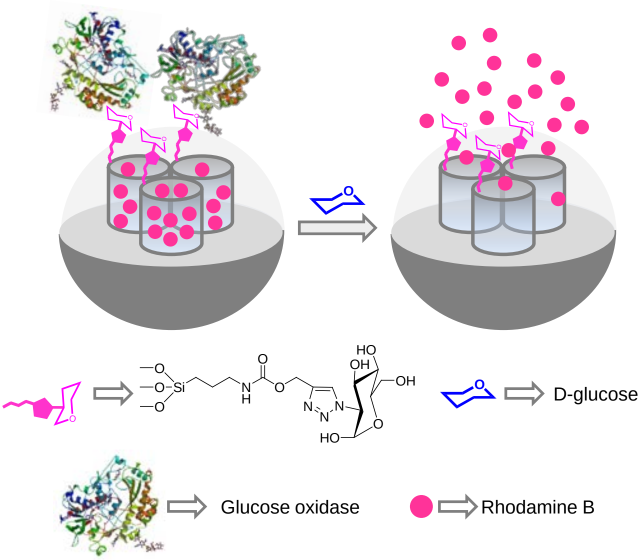

Figure 26. MSNs functionalized with D-(+)-glucosamine capped with GOx enzyme for the selective detection of D-glucose.

Villalonga and co-workers developed MSNs in which an enzyme also acted as a cap; however, in this case, the uncapping process was triggered by the product obtained by the enzyme's activity on glucose.[168] MSNs were loaded with $Ru(bipy)_3^{2+}$ and the external surface functionalized with 3-iodopropyltrimethoxysilane that was further transformed to 1-propyl-1-*H*-benzimidazole groups through a nucleophilic substitution reaction using benzimidazole. The pores were finally capped with an active CD-modified-glucose oxidase (CD-GOx) through the formation of inclusion complexes between the CDs groups in CD-GOx and the propylbenzymidazole stalks attached to the solid support. In their study, the authors confirmed that dye delivery was induced when glucose was present in the solution due to displacement of CD-GOx as a consequence of CD-GOx-induced oxidation of glucose to gluconic acid and the subsequent protonation of the benzimidazole group. The authors found a linear response to glucose in the $1\times10^{-2} - 1\times10^{-4}$ mol L^{-1} range and a LOD of 1.5×10^{-4} mol L^{-1} which was in the range of other glucose detection systems. The response to glucose was selective, and the presence of other saccharides such as mannose, fructose, galactose, maltose, and saccharose at a concentration of 1×10^{-3} mol L^{-1} induced no cargo delivery.

In a further work,[169] the same authors demonstrated that the gating mechanism and different effector ensembles can be integrated in a unique system based on the use of Janus-type nanoparticles having opposing Au and mesoporous silica faces. In particular, the porous network of the silica face was loaded with $Ru(bipy)_3^{2+}$ and the external surface grafted with 3-(2-aminoethylamino)propyltrimethoxysilane. Additionally, the gold side was functionalized with thiol modified urease enzyme as shown in Figure 27. Aqueous solution (acetate buffer pH 5) of the Janus nanoparticles showed negligible cargo release because the polyamines were protonated and the molecular gate was closed. In the presence of urea, a clear delivery of the entrapped ruthenium complex was found. This release was a consequence of the urease-catalyzed hydrolysis of urea into CO_2 and NH_3 that induced an increase in the pH of the local environment. With this increase, the polyamines became deprotonated and subsequently the gates were opened. Another gated system using Janus-type nanoparticles was recently described by the same authors.[170] In this case, the mesoporous silica face was loaded with $Ru(bipy)_3^{2+}$, functionalized with benzimidazole moieties, and the pores of the mesoporous structure blocked by the formation of inclusion complexes with β-CD. Moreover, thiol-modified esterase and GOx were covalently immobilized on the Au surface. Experimental results confirmed that the presence of either D-glucose or ethyl butyrate, or a combination of both substrates, produced a local decrease of the pH through an enzyme-catalyzed substrate conversion to gluconic acid or butyric acid which induced the opening of the β-CD-gated nanovalves and release of the entrapped dye.

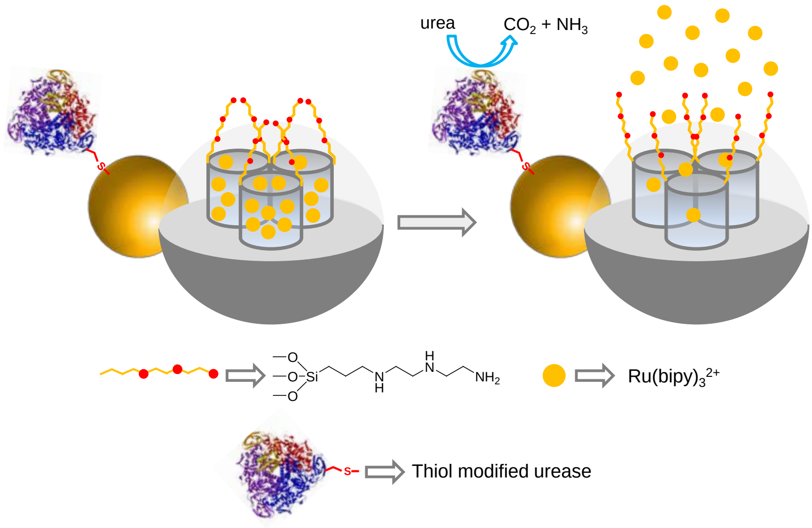

Figure 27. Janus Au-MSNs support loaded with Ru(bipy)$_3^{2+}$ and capped with polyamines for the detection of urea.

Using an enzyme-inhibitor interaction, Pascual et al have very recently developed acetylcholinesterase-capped nanoparticles able to be selectively uncapped in the presence of diisopropyl fluorophosphates (DFP), a well-known nerve agent simulant.[171] To construct such a system, MSNs were first loaded with Rh B, functionalized with a pyridostigmine derivative (an inhibitor of acetylcholinesterase) and capped with acetylcholinesterase by means of the interaction between the enzyme active-centre and pyridostigmine moieties. DFP is a stronger inhibitor than pyridostigmine and was able to displace acetylcholinesterase from the silica surface which resulted in a clear cargo delivery. The detection system responded selectively to DFP over other nerve agent simulants and organophosphorus compounds, with a LOD of 0.28 ppm.

1.4.2 Gated nanomaterials for drug delivery applications

With the advent of nanotechnology research into controlled drug delivery treatments has taken on a new dimension. Moreover, the development of molecular diagnostic tools and targeted therapeutics can be combined in order to improve the efficacy of conventional approaches.[172,173] Stimuli-responsive MSN are excellent candidates for this purpose. On one hand the efficient encapsulation and protection of the loaded drug is guaranteed. On the other hand, the possibility to immobilize suitable ligands on the MSNs surface allows to achieve a targeted delivery of the encapsulated active agents. These innovative delivery systems are able to release a drug in spatial-, temporal- and dosage-controlled manners triggered by specific physical (i.e., external triggers such as temperature,[174] magnetic field,[175] ultrasound,[176] light,[177] electric pulses[178]) or chemical (i.e., pH changes,[179] enzymes,[180] redox gradients[181]) stimuli. This section illustrates some pioneering and recent works in this field using gated-MSNs.

One of the first redox-driven capped materials was described by Lin and coworkers.[182] In their work, they used CdS nanocrystals linked with a disulfide linker to cap the pores of MSNs. To obtain the gated solid, the authors first prepared mercaptopropyl-modified MSNs via a co-condensation method. Then the external surface was functionalized with 2-(pyridyldisulfanyl)ethylamine to obtain the linker 2-(propyldisulfanyl)ethylamine. Finally, after loading pores with vancomycin or ATP, MSNs were capped with mercaptoacetic acid-coated CdS nanocrystals of *ca*. 2 nm via an amidation reaction (see Figure 28). Gated nanoparticles released less than 1.0% of cargo in the 10 mM PBS buffer solutions (pH 7.4) over a 12-hour period. On the contrary, when DTT or mercaptoethanol (ME) was added, the disulfide bridge was cleaved and allowed the rapid release of entrapped ATP or vancomycin. Cargo delivery was proportional to the concentration of the reducing agent in the solution. The biocompatibility and delivery efficiency of MSNs with neuroglial cells (astrocytes) were tested. Astrocytes cultured in the presence of CdS-capped MSNs with the ATP molecules encapsulated inside significantly increased in intracellular Ca^{2+}, which indicated that the ATP molecules released from the nanomaterial reached their receptors on the cell surface and triggered the corresponding ATP receptor-mediated increase in the intracellular calcium concentration. No changes in intracellular calcium were detected in the astrocytes incubated in the presence of CdS-capped MSNs without encapsulated ATP.

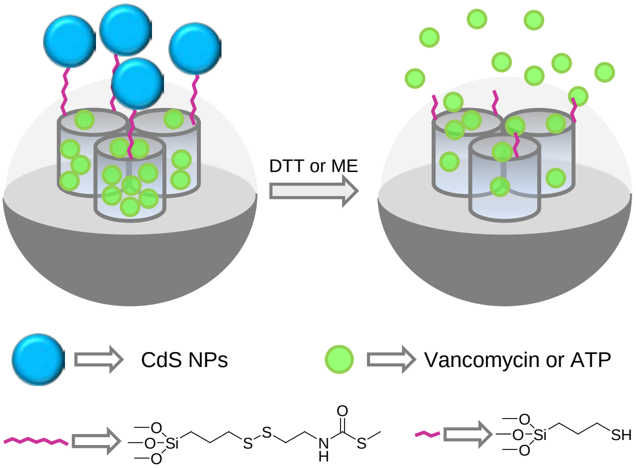

Figure 28. Delivery of vancomycin or ATP from CdS-capped MSNs due to the cleavage of disulfide bonds in the presence of reducing agents.

Regarding physical stimuli, several examples of gated materials, which were uncapped using temperature, have been described. Recently, paraffins were used by Martínez-Máñez and coworkers to develop temperature-sensitive capped MSNs.[183] The pores of the inorganic support were loaded with safranine O. Then the nanoparticles were functionalized with octadecyltrimethoxysilane to render the external surface sufficiently hydrophobic to cap the system with selected paraffins. Different solids capped with heneicosane, docosane and tetracosane were prepared. These paraffins have melting points of 39 °C, 42 °C and 49 °C, respectively. Water suspensions of the paraffin-coated MSNs at temperatures below the melting points of paraffins showed an almost "zero release" of safranine O. However, when temperature was raised above the paraffin melting point, a massive safranine O release was observed. Heneicosane-capped nanoparticles were able to release safranine O in HeLa cells when incubation was carried out at temperatures above 39 °C. Heneicosane-capped nanoparticles were also loaded with DOX and used to release this chemotherapeutic agent in HeLa cells after heating.

On the other hand, the use of DNA fragments is also a procedure to prepare temperature-controlled capped materials. In an initial example, Bein et al used double-stranded DNA to cap the pores and delivery was observed when the melting of the grafted ds-DNA was reached.[184] These authors used MSNs functionalized with azidopropyl moieties, which were then reacted with ds-DNA oligomers (containing biotin and alkyne functionalities) via a click chemistry reaction. Pores were loaded with fluorescein and the nanoparticles were capped upon avidin protein addition . The authors demonstrated that at 25 °C, the pores of the hybrid nanoparticles were tightly closed and fluorescein release was observed when the temperature went above the melting temperature for grafted ds-DNA. It was possible to fine tune the temperature at which dye release occurred by selecting grafted ds-DNA.

In other example, Ren, Qu *et al.* prepared MSNs functionalized with 3-cloropropyl moieties.[185] Chloride atoms were substituted for azide groups upon the reaction with sodium azide. The pores of the nanoparticles were loaded with Rh B and capped with the self-complementary duplex DNA sequence hexynyl-GCA TGA ATT CAT GC using a CuI-catalyzed azide-alkyne reaction (Figure 29). The suffered suspensions, pH 7.4, of the prepared nanoparticles showed negligible dye release at 25 °C, whereas remarkable Rh B delivery was observed upon heating at 50 °C. The thermal denaturation of the duplex DNA sequence was responsible for the Rh B release observed. The authors also demonstrated that cargo delivery took place in the presence of DNase I enzyme, which was able to hydrolyze the duplex DNA sequence. An analogous capped material was prepared in this case containing camptothecin (CPT) inside the pores instead of Rh B. This material was easily internalized by HepG2 cells and presented remarkable cytotoxic efficacy due to the hydrolysis of the self-complementary duplex DNA by endonucleases, which resulted in entrapped cargo release.

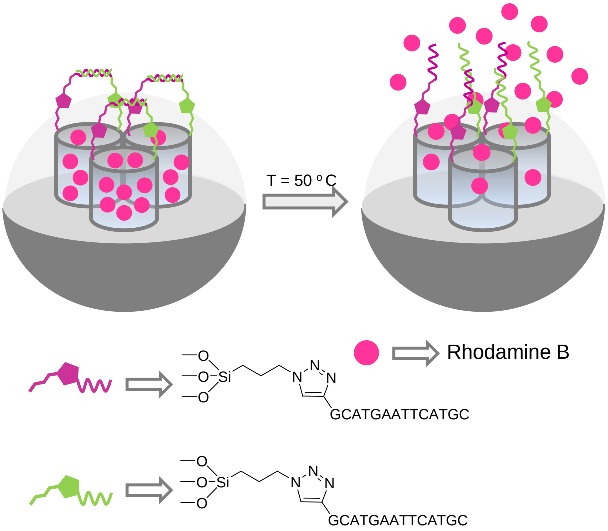

Figure 29. MSNs loaded with Rh B and capped with a ds-DNA.

From another approach, pH-driven DNA-capped systems have been also developed. For instance, Ren, Qu *et al.* used an i-motif DNA, which had a 4-stranded DNA structure at pH 5.0, as molecular cap.[186] The compact quadruplex DNA structure at pH 5.0 changed to an open random coil conformation at pH 8.0. In particular, these authors functionalized MSNs with aminopropyl moieties, which were transformed into carboxylic acid groups via the reaction with succinic anhydride. The carboxylic acids were further reacted with oligonucleotide 5'-NH_2-$(CH_2)_6$-CCC TAA CCC TAA CCC TAA CCC-3'. Nanoparticles were loaded with Rh B. Clear cargo delivery took place at pH 8, but not at pH 5.0, due to the pH-controlled conformational change, which also allowed a pulsatile release (see Figure 30).

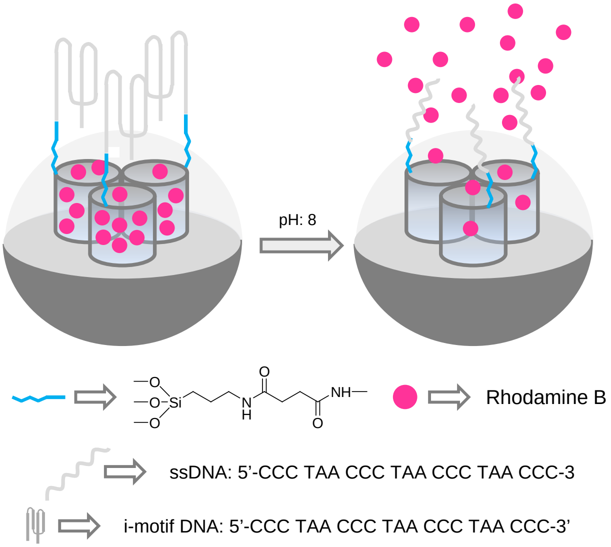

Figure 30. MSNs loaded with Rh B and capped with a quadruplex DNA structure. At pH 8, Rh B was released due to the conformational change in DNA structure.

Aiming to combine diagnostics and therapy capabilities into a single agent, some authors have developed selective glucose-responsive system and have used them for the glucose-induced release of insulin which was directly related with the amount of the glucose present in the media. In this field Lin and coworkers designed a glucose-responsive system able to stimulate insulin secretion releasing cyclic adenosine monophosphate (cAMP) and, at the same time, using gluconic acid-modified insulin (G-Ins) as capping biomolecule with the aim to overcome the common insulin release decrease of conventional glucose-responsive insulin delivery systems (Figure 31).[187] In particular, MSNs functionalized with aminopropyl and phenylboronic acid groups in the pore outlets were loaded with cAMP. To block the pores, the authors prepared FITC-labeled G-Ins which formed boroesters with the phenylboronic units. The authors tested a collection of sugars and found that the capped MSNs were opened more easily with fructose, followed by glucose. The authors studied the cAMP release at pH 7.4 and 8.5. In the absence of glucose, less than 10% of the cargo was released at both pHs. On the contrary, cAMP delivery was achieved in the presence of glucose, although delivery was higher at pH 8.5. Cell viability studies using four different cell lines i.e. rat pancreatic islet tumor (RIN-5F), mouse liver, skin fibroblast, and human cervical cancer (HeLa) cells, evidenced the non-toxicity of this material. The cellular concentration of cAMP in RIN-5F cells treated with cAMP solutions and using the capped MSNs were quantified by a Millipore cAMP HTS immunoassay evidencing that only using the solid an elevation of intracellular cAMP concentration occurred.

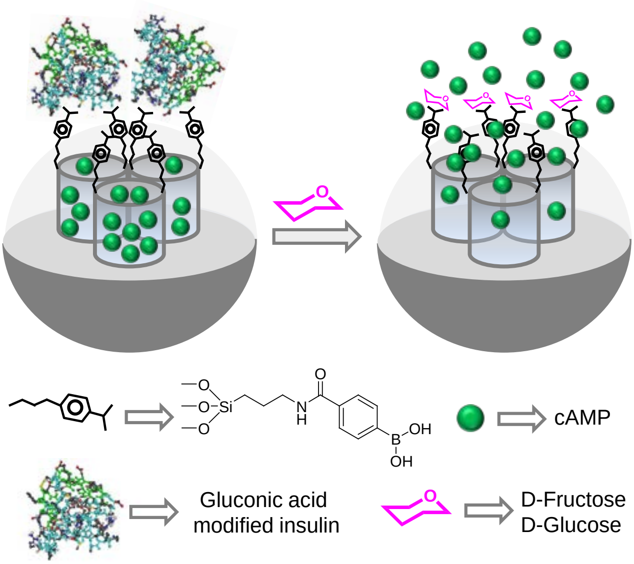

Figure 31. Glucose induced cAMP release from MSNs capped with gluconic acid-modified insulin.

The controlled release of insulin in the presence of glucose was also described by Shi and co-workers.[188] The authors used MSNs with a pore size of *ca.* 12 nm that were loaded with insulin. Then, the external surface of the particles was coated with poly(ethyleneimine), through simple electrostatic interactions, in order to include amino groups at the surface. The amino groups were cross-linked with glutaraldehyde and the obtained free aldehyde moieties reacted with GOx and catalase (CAT) enzymes to form imine bonds. PBS suspensions (pH 7.4) of the nanoparticles showed zero release of the entrapped insulin, however, when glucose was added a remarkable insulin release, directly related with the amount of the glucose present in the media, was observed. Upon addition of glucose a decrease in the pH of the microenvironment was produced due to its oxidation to gluconic acid induced by GOx enzyme. This acidic pH weakened the cross-linked multilayer structure by partly breaking imine bonds with the subsequent enhancement of insulin release. The activity of GOx was assured by the CAT enzyme that was able to decompose the hydrogen peroxide, formed in the oxidation of glucose, into water and oxygen.

Li, Zhang and coworkers also reported the design of a capped system for insulin delivery which was responsive to the presence of glucose and pH changes in a cooperative way.[189] The authors functionalized MSNs with 3-(methylacryloxy)propyltrimethoxysilane and then the nanoparticles were covered with a polymeric shell formed by 3-acrylamidophenylboronic acid and *N*-isopropylacrylamide finally obtaining two solids; in one case the polymer coated over the material was cross-linked by addition of dextran-maleic acid and in the second not. Phenyl boronic acids on the copolymer shell were sensitive to glucose and pH changes. The nanoparticles were loaded with insulin and its delivery at different pHs and in the presence or absence of glucose was studied for the two polymer-coated materials. The best results were obtained using the cross-linked polymer shell in presence of glucose at pH over 7.4. Furthermore cell viability experiments using MTT assays demonstrated both solids were nontoxic to A549 cells. In a more recent work,[190] the same authors used a similar synthesis procedure to prepare different materials with a copolymer shell of dextran-maleic acid bearing 3-amidophenylboronic acid moieties. Three solids containing different amounts of grafted copolymer were prepared and their potential *in vivo* application as oral insulin delivery systems was studied. These studies demonstrated that a thicker layer of polymer resulted in a greater capacity of drug loading and a slow delivery kinetics. The cellular uptake of the capped nanoparticles was corroborated using a similar solid loaded with insulin and capped with the same copolymer which was additionally marked with FITC. Absorption and bioavailability of protein drugs in intestine is commonly low due to the weak mucosal membrane permeability and enzymatic degradation. Therefore, the absorption properties of capped MSNs were investigated in epithelial intestinal villi. Remarkably, strong green dots in villi were observed after incubation with capped nanoparticles indicating good absorption of the nanomaterial. Finally in vivo studies, via oral administration of diverse insulin-loaded capped solids having a different polymer shell thickness, in diabetic rats were compared to free insulin oral and injected administration. Oral administration of insulin-loaded nanoparticles decreased blood glucose levels at 1.5 h, and remained low even at 7 hours after administration. These assays confirmed that the capped support was able to reduce more efficiently blood glucose levels than oral administration of insulin. A more sustained reduction of glucose was achieved when using the capped material having the thickest polymer shell.

References

1. Richard Feyman, *Eng. Sci.* **1960**, *23*, 22–36.
2. E. Drexler, *The Coming Era of Nanotechnology*, Anchor Books, Doubleday, **1986**.
3. S. L. Brock, *J. Am. Chem. Soc.* **2004**, *126*, 44, 14679-14679.
4. R. Bott, *Springer Handbook of Nanotechnology*, Springer-Verlag, Berlin Heidelberg New York, **2014**.
5. V. K. Varadan, A. S. Pillai, D. Mukherji, M. Dwivedi, L. Chen, *Nanosci. Nanotechnol. Eng.* **2010**, 71–105.
6. S. Agrawal, P. Rathore, *Int. J. Curr. Microbiol. Appl. Sci.* **2014**, *3*, 43–55.
7. S. Ershov, F. Khelifa, M.-E. Druart, Y. Habibi, M.-G. Olivier, R. Snyders, P. Dubois, *RSC Adv.* **2015**, *5*, 14256–14265.
8. S. D. F. Mihindukulasuriya, L.-T. Lim, *Trends Food Sci. Technol.* **2014**, *40*, 149–167.
9. S. Raj, S. Jose, U. S. Sumod, M. Sabitha, *J. Pharm. Bioallied Sci.* **2012**, *4*, 186–193.
10. K. J. Sankaran, S. Kunuku, B. Sundaravel, P.-Y. Hsieh, H.-C. Chen, K.-C. Leou, N.-H. Tai, I.-N. Lin, *Nanoscale* **2015**, *7*, 4377–4385.
11. N. K. A.K. Haghi, Ajseh K. Zachariah, *Nanomaterials. Synthesis, Characterization and Applications*, Aplle Academic Press, Toronto, New Jersey, **2013**.
12. L. Nicole, C. Laberty-Robert, L. Rozes, C. Sanchez, *Nanoscale* **2014**, *6*, 6267–6292.
13. H. Liu, S. Cui, Y. Guo, Y. Li, C. Huang, Z. Zuo, X. Yin, Y. Song, D. Zhu, *J. Mater. Chem.* **2009**, *19*, 1031–1036.
14. W. U. Huynh, J. J. Dittmer, A. P. Alivisatos, *Science.* **2002**, *295*, 2425–2427.
15. H. Liu, Z. Zuo, Y. Guo, Y. Li, Y. Li, *Angew. Chem. Int. Ed.* **2010**, *49*, 2705–2707.
16. Clément Sanchez, *J. Mater. Chem.* **2005**, *15*, 3557–3558.
17. Q. Zhang, E. Uchaker, S. L. Candelaria, G. Cao, *Chem. Soc. Rev.* **2013**, *42*, 3127-3171.
18. N. Linares, A. M. Silvestre-Albero, E. Serrano, J. Silvestre-Albero, J. García-Martínez, *Chem. Soc. Rev.* **2014**, *43*, 7681–7717.
19. T. Wagner, S. Haffer, C. Weinberger, D. Klaus, M. Tiemann, *Chem. Soc. Rev.* **2013**, *42*, 4036–4053.
20. C. Perego, R. Millini, *Chem. Soc. Rev.* **2013**, *42*, 3956-3676.
21. A. E. Garcia-Bennett, *Nanomedicine* **2011**, *6*, 867-877.
22. F. Sancenón, L. Pascual, M. Oroval, E. Aznar, R. Martínez-Máñez, *ChemistryOpen* **2015**, *4*, 418–437.
23. X. S. Zhao, *J. Mater. Chem.* **2006**, *16*, 623–625.
24. X. Liu, Y. Du, Z. Guo, S. Gunasekaran, C.-B. Ching, Y. Chen, S. S. J. Leong, Y. Yang, *Microporous Mesoporous Mater.* **2009**, *122*, 114–120.

25. C. Perego, R. Millini, *Chem. Soc. Rev.* **2013**, *42*, 3956–3976.
26. C. C. Cho, B. E. Gnade, D. M. Smith, J. Changming, W. C. Ackerman, G. C. Johnston, " Porous dielectric material with improved pore surface properties for electronics applications". Patent: US6140252 A, issued date October 31, **2000**.
27. W. Li, J. Liu, D. Zhao, *Nat. Rev. Mater.* **2016**, *1*, 1–17.
28. D. J. Wales, J. Grand, V. P. Ting, R. D. Burke, K. J. Edler, C. R. Bowen, S. Mintova, A. D. Burrows, *Chem. Soc. Rev.* **2015**, *44*, 4290–4321.
29. N. K. Jensen, T. E. Rufford, G. Watson, D. K. Zhang, K. I. Chan, E. F. May, *J. Chem. Eng. Data* **2012**, *57*, 106–113.
30. A. Corma, *Chem. Rev.* **1997**, *97*, 2373–2420.
31. C. T. Kresge, M. E. Leonowicz, W. J. Roth, J. C. Vartuli, "Synthetic Mesoporous Crystaline Material", Patent: US5098684 A, issued date March 24, **1992**.
32. J. S. Beck, J. C. Vartuli, W. J. Roth, M. E. Leonowicz, C. T. Kresge, K. D. Schmitt, C. T.-W. Chu, D. H. Olson, E. W. Sheppard, S. B. McCullen, et al., *J. Am. Chem. Soc.* **1992**, *114*, 10834–10843.
33. C. T. Kresge, W. J. Roth, *Chem. Soc. Rev.* **2013**, *42*, 3663–70.
34. F. Hoffmann, M. Cornelius, J. Morell, M. Fröba, *Angew. Chem. Int. Ed.* **2006**, *45*, 3216–3251.
35. A Monnier, F. Schüth, Q. Huo, D. Kumar, D. Margolese, R. S. Maxwell, G. D. Stucky, M. Krishnamurty, P. Petroff, a Firouzi, et al., *Science* **1993**, *261*, 1299–1303.
36. D. Zhao, Q. Huo, J. Feng, B. F. Chmelka, G. D. Stucky, *J. Am. Chem. Soc.* **1998**, *120*, 6024-6036**.**
37. D. Zhao, J. Feng, Q. Huo, N. Melosh, G. H. Fredrickson, B. F. Chmelka, G. D. Stucky, *Science* **1998**, *279*, 548–552.
38. C. Chen, H. Li, M. E. Davis, *Synthesis* **1993**, *2*, 17–26.
39. S. Huh, J. W. Wiench, J.-C. Yoo, M. Pruski, V. S.-Y. Lin, *Chem. Mater* **2003**, *15*, 4247–4256.
40. S. P. Naik, W. Fan, A. Toshiyuki Yokoi, Tatsuya Okubo, *Langmuir* **2006**, *22*, 6391–6397.
41. H. B. S. Chan, P. M. Budd, T. D. Naylor, *J. Mater. Chem.* **2001**, *11*, 951–957.
42. a Walcarius, E. Sibottier, M. Etienne, J. Ghanbaja, *Nat. Mater.* **2007**, *6*, 602–608.
43. D. Wang, R. A. Caruso, F. Caruso, *Chem. Mater.* **2001**, *13*, 364–371.
44. A. Corma, Q. Kan, M. T. Navarro, J. Pérez-Pariente, F. Rey, *Chem. Mater.* **1997**, *9*, 2123–2126.
45. F. Gao, P. Botella, A. Corma, J. Blesa, L. Dong, *J. Phys. Chem. B* **2009**, *113*, 1796–1804.

46. N. Z. Knezevic, J.-O. Durand, *Nanoscale* **2015**, *7*, 2199–2209.
47. G. Sponchia, R. Marin, I. Freris, M. Marchiori, E. Moretti, L. Storaro, P. Canton, A. Lausi, A. Benedetti, P. Riello, *J. Nanoparticle Res.* **2014**, *16*, 2245-1.
48. K. Yano, Y. Fukushima, *J. Mater. Chem.* **2004**, *14*, 1579-1584.
49. M. H. Kim, H. K. Na, Y. K. Kim, S. R. Ryoo, H. S. Cho, K. E. Lee, H. Jeon, R. Ryoo, D. H. Min, *ACS Nano* **2011**, *5*, 3568–3576.
50. M. Mizutani, Y. Yamada, K. Yano, *Chem. Commun.* **2007**, *18*, 1172–1174.
51. T. Kimura, Y. Sugahara, K. Kuroda, K. Kuroda, *Chem. Commun.* **1998**, 559–560.
52. B. Lefèvre, A. Galarneau, J. Iapichella, C. Petitto, F. Di Renzo, F. Fajula, Z. Bayram-Hahn, R. Skudas, K. Unger, *Chem. Mater.* **2005**, *17*, 601–607.
53. J.-H. Sun, M.-O. Coppens, *J. Mater. Chem.* **2002**, *12*, 3016–3020.
54. A. Sayari, S. Hamoudi, Y. Yang, *Chem. Mater.* **2005**, *17*, 212–216.
55. M. Mizutani, Y. Yamada, T. Nakamura, K. Yano, *Chem. Mater.* **2008**, *20*, 4777–4782.
56. K. Moller, T. Bein, *Chem. Mater.* **1998**, *10*, 2950–2963.
57. G. A. Ozin, E. Chomski, D. Khushalani, M. J. MacLachlan, *Curr. Opin. Colloid Interface Sci.* **1998**, *3*, 181–193.
58. D. M. Antonelli, J. Y. Ying, *Curr. Opin. Colloid Interface Sci.* **1996**, *1*, 523–529.
59. A. Vinu, K. Z. Hossain, K. Ariga, *J. Nanosci. Nanotechnol.* **2005**, *5*, 347–371.
60. A. Stein, B. J. Melde, R. C. Schroden, *Adv. Mater.* **2000**, *12*, 1403–1419.
61. F. de Juan, E. Ruiz-Hitzky, *Adv. Mater.* **2000**, *12*, 430–432.
62. M. H. Lim, A. Stein, *Chem. Mater.* **1999**, *11*, 3285–3295.
63. D. A. Loy, K. J. Shea, *Chem. Rev.* **1995**, *95*, 1431–1442.
64. B. Hatton, K. Landskron, W. Whitnall, D. Perovic, G. A. Ozin, *Acc. Chem. Res.* **2005**, *38*, 305–312.
65. K. S. W. Sing, D. H. Everett, R. a. W. Haul, L. Moscou, R. a. Pierotti, J. Rouquérol, T. Siemieniewska, *Pure Appl. Chem.* **1985**, *57*, 603–619.
66. F. Rouquerol, J. Rouquerol, K. Sing, Interpretation of physisorption isotherms at the gas–solid interface. Adsorption by Powders and Porous Solids, Academic Press, London, **1999**, 110-111.
67. S. Brunauer, P. H. Emmett, E. Teller, *J. Am. Chem. Soc.* **1938**, *60*, 309–319.
68. E. P. Barrett, L. G. Joyner, P. P. Halenda, *J. Am. Chem. Soc.* **1951**, *73*, 373–380.
69. K. Ariga, S. Ishihara, J. Labuta, J. P. Hill, *Curr. Org. Chem.* **2011**, *15*, 3719.
70. A. B. Descalzo, R. Martínez-Máñez, F. Sancenón, K. Hoffmann, K. Rurack, *Angew. Chem. Int. Ed.* **2006**, *45*, 5924–5948.
71. V. Valtchev, L. Tosheva, *Chem. Rev.* **2013**, *113*, 6734–6760.

72. A. Stein, *Adv. Mater.* **2003**, *15*, 763-775.
73. G. J. A. A. Soler-Illia, O. Azzaroni, *Chem. Soc. Rev.* **2011**, *40*, 1107–1150.
74. A. P. Wight, M. E. Davis, *Chem. Rev.* **2002**, *102*, 3589-3614.
75. G. Kickelbick, *Angew. Chemie - Int. Ed.* **2004**, *43*, 3102–3104.
76. S. Saha, K. C. F. Leung, T. D. Nguyen, J. F. Stoddart, J. I. Zink, *Adv. Funct. Mater.* **2007**, *17*, 685–693.
77. S. Angelos, E. Johansson, J. F. Stoddart, J. I. Zink, *Adv. Funct. Mater.* **2007**, *17*, 2261–2271.
78. F. Wang, X. Liu, I. Willner, *Angew. Chem. Int. Ed.* **2015**, *54*, 1098–1129.
79. N. Song, Y. – W. Yang, *Chem. Soc. Rev.* **2015**, *44*, 3474–3504.
80. G. Wang, J. Zhang, *J. Photochem. Photobiol. C* **2012**, *13*, 299–309.
81. A. B. Braunschweig, B. H. Northrop, J. F. Stoddart, *J. Mater. Chem.* **2006**, *16*, 32–44.
82. B. G. Trewyn, S. Giri, Slowing II, V. S. Lin, *Chem. Commun.* **2007**, 3236–3245.
83. E. Aznar, R. Martínez-Máñez, F. Sancenón, *Expert Opin. Drug Deliv.* **2009**, *6*, 643–655.
84. Y.-W. Yang, *Medchemcomm* **2011**, *2*, 1033-1049.
85. J. A. Barreto, W. O'Malley, M. Kubeil, B. Graham, H. Stephan, L. Spiccia, *Adv. Mater.* **2011**, *23*, H18–H40.
86. W. J. Stark, *Angew. Chem. Int. Ed.* **2011**, *50*, 1242–1258.
87. Z. Li, J. C. Barnes, A. Bosoy, J. F. Stoddart, J. I. Zink, *Chem. Soc. Rev.* **2012**, *41*, 2590–2605.
88. T. L. Doane, C. Burda, *Chem. Soc. Rev.* **2012**, *41*, 2885–2911.
89. C. Coll, A. Bernardos, R. Martínez-Máñez, F. Sancenón, *Acc. Chem. Res.* **2013**, *46*, 339–349.
90. C. H. Lu, B. Willner, I. Willner, *ACS Nano* **2013**, *7*, 8320–8332.
91. S. Koutsopoulos, *Adv. Drug Deliv. Rev.* **2012**, *64*, 1459–1476.
92. Y. Chen, H. Chen, J. Shi, *Adv. Mater.* **2013**, *25*, 3144–3176.
93. Q. He, J. Shi, *Adv. Mater.* **2014**, *26*, 391–411.
94. M. Vallet-Regí, E. Ruiz-Hernández, *Adv. Mater.* **2011**, *23*, 5177–5218.
95. K. M. L. Taylor-Pashow, J. Della Rocca, R. C. Huxford, W. Lin, *Chem. Commun.* **2010**, *46*, 5832–5849.
96. A. Bitar, N. M. Ahmad, H. Fessi, A. Elaissari, *Drug Discov. Today* **2012**, *17*, 1147–1154.
97. J. M. Rosenholm, C. Sahlgren, M. Lindén, *J. Mater. Chem.* **2010**, *20*, 2707-2713.
98. C. Y. Ang, S. Y. Tan, Y. Zhao, *Org. Biomol. Chem.* **2014**, *12*, 4776–4806.

99. M. Manzano, M. Vallet-Regí, *Prog. Solid State Chem.* **2012**, *40*, 17-30.
100. M. W. Ambrogio, C. R. Thomas, Y. – L. Zhao, J. I. Zink, J. F. Stoddart, *Acc. Chem. Res.* **2011**, *44*, 903–913.
101. J. Xie, S. Lee, X. Chen, *Adv. Drug Deliv. Rev.* **2010**, *62*, 1064–1079.
102. P. Rai, S. Mallidi, X. Zheng, R. Rahmanzadeh, Y. Mir, S. Elrington, A. Khurshid, T. Hasan, *Adv. Drug Deliv. Rev.* **2010**, *62*, 1094–1124.
103. J. M. Rosenholm, C. Sahlgren, M. Lindén, *Curr. Drug Targets* **2011**, *12*, 1166–1186.
104. J. M. Rosenholm, C. Sahlgren, M. Linden, *Nanoscale* **2010**, *2*, 1870–1883.
105. Y. – C. Chen, X. – C. Huang, Y. – L. Luo, Y. – C. Chang, Y. – Z. Hsieh, H. – Y. Hsu, *Sci. Technol. Adv. Mater.* **2013**, *14*, 44407.
106. F. Sancenón, L. Pascual, M. Oroval, E. Aznar, R. Martínez-Máñez, *ChemistryOpen* **2015**, *4*, 418–437.
107. R. Martínez-Máñez, F. Sancenón, *Chem. Rev.* **2003**, *103*, 4419–4476.
108. R. Martínez-Máñez, F. Sancenón, M. Hecht, M. Biyikal, K. Rurack, *Anal. Bioanal. Chem.* **2011**, *399*, 55–74.
109. B. G. Trewyn, I. I. Slowing, S. Giri, H.-T. Chen, V. S.-Y. Lin, *Acc. Chem. Res.* **2007**, *40,* 846–853.
110. D. Tarn, C. E. Ashley, M. Xue, E. C. Carnes, J. I. Zink, C. J. Brinker, *Acc. Chem. Res.* **2013**, *46*, 792-801.
111. Y. – W. Yang, Y. – L. Sun, N. Song, *Acc. Chem. Res.* **2014**, *47*, 1950-1960.
112. A. Bansal, Y. Zhang, *Acc. Chem. Res.* **2014**, *47*, 3052-3060.
113. Y. Zhao, J. L. Vivero-Escoto, I. I. Slowing, B. G. Trewyn, V. S. – Y. Lin, *Expert Opin. Drug Deliv.* **2010**, *7*, 1013–1029.
114. J. L. Vivero-Escoto, I. I. Slowing, B. G. Trewyn, V. S. – Y. Lin, *Small* **2010**, *6*, 1952–1967.
115. G. K. Darbha, E. Lee, Y. R. Anderson, P. Fowler, K. Mitchell, P. C. Ray, *IEEE Sens. J.* **2008**, *8*, 693–700.
116. L. R. Hilliard, X. Zhao, W. Tan, *Anal. Chim. Acta* **2002**, *470*, 51–56.
117. X.-F. L. and X. C. Le Feng Li, Hongquan Zhang, Zhixin Wang, Ashley M. Newbigging, Michael S. Reid, *Anal. Chem.* **2015**, *87*, 274–292.
118. A. Sett, *Open J. Appl. Biosens.* **2012**, *1*, 9–19.
119. M. Hecht, E. Climent, M. Biyikal, F. Sancenón, R. Martínez-Máñez, K. Rurack, *Coord. Chem. Rev.* **2013**, *257*, 2589–2606.
120. E. J. Cho, J.-W. Lee, A. D. Ellington, *Annu. Rev. Anal. Chem.* **2009**, *2*, 241–264.
121. G. G. Guilbault, *Handbook of Enzymatic Methods of Analysis,*M. Dekker, New York, **1976**.

122. N. L. Rosi, D. A. Giljohann, C. S. Thaxton, A. K. R. Lytton-Jean, M. S. Han, C. A. Mirkin, *Science* **2006**, *312*, 1027-1030.
123. Y.-H. Rogers, P. Jiang-Baucom, Z.-J. Huang, V. Bogdanov, S. Anderson, M. T. Boyce-Jacino, *Anal. Biochem.* **1999**, *266*, 23–30.
124. T. Böcking, K. A. Kilian, K. Gaus, J. J. Gooding, *Langmuir* **2006**, *22*, 3494–3496.
125. H. F. Teh, H. Gong, X.-D. Dong, X. Zeng, A. Lai Kuan Tan, X. Yang, S. N. Tan, *Anal. Chim. Acta* **2005**, *551*, 23–29.
126. D. Peelen, L. M. Smith, *Langmuir* **2005**, *21*, 266–271.
127. X.-H. Xu, A. J. Bard, *J. Am. Chem. Soc.* **1995**, *117*, 2627–2631.
128. S. G. Wang, R. Wang, P. J. Sellin, Q. Zhang, *Biochem. Biophys. Res. Commun.* **2004**, *325*, 1433–1437.
129. Y. Zhang, Q. Yuan, T. Chen, X. Zhang, Y. Chen, W. Tan, *Anal. Chem.* **2012**, *84*, 1956–1962.
130. E. Climent, R. Martínez-Máñez, F. Sancenón, M. D. Marcos, J. Soto, A. Maquieira, P. Amorós, *Angew. Chem. Int. Ed.* **2010**, *49*, 7281–7283.
131. E. Climent, L. Mondragón, R. Martínez-Máñez, F. Sancenón, M. D. Marcos, J. R. Murguía, P. Amorós, K. Rurack, E. Pérez-Payá, *Angew. Chem. Int. Ed.* **2013**, *52*, 8938-8942.
132. L. Pascual, I. Baroja, E. Aznar, F. Sancenón, M. D. Marcos, J. R. Murguía, P. Amorós, K. Rurack, R. Martínez-Máñez, *Chem. Commun.* **2015**, *51*, 1414–1416.
133. F. Pu, Z. Liu, J. S. Ren, X. G. Qu, *Chem. Commun.* **2013**, *49*, 2305-2307.
134. Z. Zhang, D. Balogh, F. Wang, S. Y. Sung, R. Nechushtai, I. Willner, *ACS Nano* **2013**, *7*, 8455-8468.
135. Z. Wang, X. Yang, J. Feng, Y. Tang, Y. Jiang, N. He, *Analyst* **2014**, *139*, 6088–6091.
136. K. Ren, J. Wu, Y. Zhang, F. Yan, H. Ju, *Anal. Chem.* **2014**, *86*, 7494-7499.
137. Y. Lu, J. Liu, *Curr. Opin. Biotechnol.* **2006**, *17*, 580–588.
138. I. Willner, B. Shlyahovsky, M. Zayats, B. Willner, *Chem. Soc. Rev.* **2008**, *37*, 1153–1165.
139. R. Orbach, B. Willner, I. Willner, *Chem. Commun.* **2015**, *51*, 4144–4160.
140. M. Hollenstein, C. Hipolito, C. Lam, D. Dietrich, D. M. Perrin, *Angew. Chem. Int. Ed.* **2008**, *47*, 4346–4350.
141. W. Zhou, Q. Chen, P.-J. J. Huang, J. Ding, J. Liu, *Anal. Chem.* **2015**, *87*, 4001–4007.
142. Z. X. Zhang, D. Balogh, F. A. Wang, I. Willner, *J. Am. Chem. Soc.* **2013**, *135*, 1934-1940.
143. Z. Zhang, F. Wang, D. Balogh, I. Willner, *J. Mater. Chem. B* **2014**, *2*, 4449–4455.
144. L. Fu, J. Zhuang, W. Lai, X. Que, *J. Mater. Chem. B* **2013**, *1*, 6123–6128.

145. E. Luzi, M. Minunni, S. Tombelli, M. Mascini, *TrAC Trends Anal. Chem.* **2003**, *22*, 810–818.
146. K. M. You, S. H. Lee, A. Im, S. B. Lee, *Biotechnol. Bioprocess Eng.* **2003**, *8*, 64–75.
147. A. D. Ellington, J. W. Szostak, *Nature* **1990**, *346*, 818–822.
148. M. N. Win, J. S. Klein, C. D. Smolke, *Nucleic Acids Res.* **2006**, *34*, 5670–5682.
149. R. D. Jenison, S. C. Gill, A. Pardi, B. Polisky, *Science* **1994**, *263*, 1425-1429.
150. S. Tombelli, M. Minunni, M. Mascini, *Biomol. Eng.* **2007**, *24*, 191–200.
151. M. Famulok, J. S. Hartig, G. Mayer, *Chem. Rev.* **2007**, *107*, 3715–3743.
152. D. H. J. Bunka, P. G. Stockley, *Nat Rev Micro* **2006**, *4*, 588–596.
153. V. C. Ozalp, T. Schafer, *Chem. Eur. J.* **2011**, *17*, 9893–9896.
154. V. C. Ozalp, A. Pinto, E. Nikulina, A. Chuvilin, T. Schaefer, *Part. Part. Sys. Charact.* **2014**, *31*, 161–167.
155. X. He, Y. Zhao, D. He, K. Wang, F. Xu, J. Tang, *Langmuir* **2012**, *28*, 12909–12915.
156. C. L. Zhu, C. H. Lu, X. Y. Song, H. H. Yang, X. R. Wang, *J. Am. Chem. Soc.* **2011**, *133*, 1278–1281.
157. L. Hou, C. Zhu, X. Wu, G. Chen, D. Tang, *Chem. Commun.* **2014**, *50*, 1441-1443.
158. Y. Wen, L. Xu, C. Li, H. Du, L. Chen, B. Su, Z. Zhang, X. Zhang, Y. Song, *Chem. Commun.* **2012**, *48*, 8410–8412.
159. L. Chen, Y. Wen, B. Su, J. Di, Y. Song, L. Jiang, *J. Mater. Chem.* **2011**, *21*, 13811–13811.
160. R. Qian, L. Ding, H. Ju, *J. Am. Chem. Soc.* **2013**, *135*, 13282–13285.
161. Y. Wang, M. Lu, J. Zhu, S. Tian, *J. Mater. Chem. B* **2014**, *2*, 5847–5853.
162. S. Zong, Z. Wang, H. Chen, D. Zhu, P. Chen, Y. Cui, *IEEE Trans. Nanobiosci.* **2014**, *13*, 55-60.
163. G. Marko-Varga, E. Dominguez, *Trends Anal. Chem.* **1991**, *10*, 290–297.
164. L. P. Wackett, *Microb. Biotechnol.* **2016**, *9*, 430–431.
165. E. Katz, A. F. Bückmann, I. Willner, *J. Am. Chem. Soc.* **2001**, *123*, 10752–10753.
166. A. Popat, S. Jambhrunkar, J. Zhang, J. Yang, H. Zhang, A. Meka, C. Yu, *Chem. Commun.* **2014**, *50*, 5547–5550
167. M. Chen, C. Huang, C. He, W. Zhu, Y. Xu, Y. Lu, *Chem. Commun.* **2012**, *48*, 9522–9524.
168. E. Aznar, R. Villalonga, C. Giménez, F. Sancenón, M. D. Marcos, R. Martínez-Máñez, P. Díez, J. M. Pingarrón, P. Amorós, *Chem. Commun.* **2013**, *49*, 6391–6393.
169. R. Villalonga, P. Díez, A. Sánchez, E. Aznar, R. Martínez-Máñez, J. M. Pingarrón, *Chem. Eur.J.* **2013**, *19*, 7889–7894.
170. P. Díez, A. Sánchez, M. Gamella, P. Martínez-Ruíz, E. Aznar, C. de la Torre, J. R.

Murguía, R. Martínez-Máñez, R. Villalonga, J. M. Pingarrón, *J. Am. Chem. Soc.* **2014**, *136*, 9116–9923.

171. L. Pascual, S. El Sayed, R. Martínez-Máñez, A. M. Costero, S. Gil, P. Gaviña, F. Sancenón, *Org. Lett.* **2016**, *18*, 5548–5551.
172. K. Park, *J. Control. Release* **2014**, *190*, 3–8.
173. T. Dreifuss, O. Betzer, M. Shilo, A. Popovtzer, M. Motiei, R. Popovtzer, *Nanoscale* **2015**, *7*, 15175–15184.
174. B. Jeong, S. W. Kim, Y. H. Bae, *Adv. Drug Deliv. Rev.* **2002**, *54*, 37–51.
175. E. Bringas, Ö. Köysüren, D. V Quach, M. Mahmoudi, E. Aznar, J. D. Roehling, M. D. Marcos, R. Martínez-Máñez, P. Stroeve, *Chem. Commun.* **2012**, *48*, 5647–5649.
176. J. Di, J. Price, X. Gu, X. Jiang, Y. Jing, Z. Gu, *Adv. Healthc. Mater.* **2014**, *3*, 811–816.
177. S. Shah, P. K. Sasmal, K.-B. Lee, *J. Mater. Chem. B* **2014**, *2*, 7685–7693.
178. Y. Li, R. S. Shawgo, B. Tyler, P. T. Henderson, J. S. Vogel, A. Rosenberg, P. B. Storm, R. Langer, H. Brem, M. J. Cima, *J. Control. Release* **2004**, *100*, 211–219.
179. J. Liu, Y. Huang, A. Kumar, A. Tan, S. Jin, A. Mozhi, X.-J. Liang, *Biotechnol. Adv.* **2014**, *32*, 693–710.
180. Y. Elani, R. V Law, O. Ces, *Nat. Commun.* **2014**, *5*, 5305.
181. A. F. Wang, M. Y. Guo, N. Wang, J. Y. Zhao, W. X. Qi, F. Muhammad, L. Chen, Y. J. Guo, N. T. Nguyen, G. S. Zhu, *Nanoscale* **2014**, *6*, 5270–5278.
182. C. Y. Lai, B. G. Trewyn, D. M. Jeftinija, K. Jeftinija, S. Xu, S. Jeftinija, V. S. Y. Lin*, J. Am. Chem. Soc.* **2003**, *125*, 4451-4459.
183. E. Aznar, L. Mondragón, J. V Ros-Lis, F. Sancenón, M. D. Marcos, R. Martínez-Máñez, J. Soto, E. Pérez-Payá, P. Amorós, *Angew. Chem. Int. Ed.* **2011**, *50*, 11172–11172-11175.
184. A. Schlossbauer, S. Warncke, P. M. E. Gramlich, J. Kecht, A. Manetto, T. Carell, T. Bein, *Angew. Chem. Int.* **2010**, *49*, 4734–4737.
185. C. Chen, J. Geng, F. Pu, X. Yang, J. Ren, X. Qu*, Angew. Chem. Int. Ed.* **2011**, *50*, 882–886.
186. C. E. Chen, F. Pu, Z. Z. Huang, Z. Liu, J. S. Ren, X. G. Qu, *Nucleic Acids Res.* **2011**, *39*, 1638-1644.
187. Y. N. Zhao, B. G. Trewyn, I. I. Slowing, V. S. Y. Lin, *J. Am. Chem. Soc.* **2009**, *131*, 8398–8400.
188. W. Zhao, H. Zhang, Q. He, Y. Li, J. Gu, L. Li, H. Li, J. Shi, *Chem. Commun.* **2011**, *47*, 9459–9461.
189. L. Sun, X. Zhang, C. Zheng, Z. Wu, C. Li, *J. Phys. Chem. B* **2013**, *117*, 3852–3860.
190. L. Sun, X. Zhang, Z. Wu, C. Zheng, C. Li, *Polym. Chem.* **2014**, *5*, 1999–2009.

2. Objectives

Taking into account the high potential of biogated nanomaterials as sensing systems, the possibility of designing different nanodevices for the detection of specific target analytes of biomedical or environmental interest has been considered in this Thesis. Moreover, the possibility of designing gated nanomaterials for the controlled release of insulin has also been studied. In this context, new hybrid materials based on mesoporous silica matrices and functionalized with suitable capping moieties have been prepared and characterized. Gating ensembles are expected to keep cargo confined in the mesopores yet entrapped payload is expected to be delivered in the presence of target species. The work developed in this thesis is divided in two different general sections:

✓ **Controlled delivery systems using nucleic acid-capped mesoporous silica nanoparticles.** Nucleic acid-gated mesoporous silica nanoparticles are prepared with the aim to detect, by means of optical methods, target species of biochemical or environmental interest. Specific objectives are:

  I. To design, synthetize and characterize new organic-inorganic hybrid materials based in silica mesoporous supports loaded with a dye (reporter) and capped with suitable nucleic acids (aptamers or oligonucleotides) able to selectively respond to the presence of α-thrombin, As(III), *Mycoplasma* genomic DNA and cocaine.

  II. To study the release of the loaded reporter from the capped materials in the presence of the corresponding triggering analyte.

  III. To study the sensitivity of the prepared gated sensing materials via determination of the limit of detection for the corresponding analyte.

  IV. To assess the selectivity of the developed nanoprobes in the presence of potential interfering species.

  V. To evaluate the potential detection of the target analytes in real complex samples.

- ✓ **Controlled delivery systems using enzyme-capped silica nanoparticles.** Enzyme-capped silica nanoparticles are used to design self-regulated insulin delivery system in the presence of glucose. Specific objectives are:

  I. To design, synthetize and characterize a new GOx-capped hybrid material (GOx: glucose oxidase) based in silica mesoporous nanoparticles, loaded with insulin and able to deliver the cargo as consequence of the presence of glucose in solution.

  II. To validate the aperture protocol as a function of time and glucose concentration.

  III. To assess the selectivity to glucose of the prepared capped material by testing other potential interfering saccharides.

3. An aptamer-gated silica mesoporous material for thrombin detection

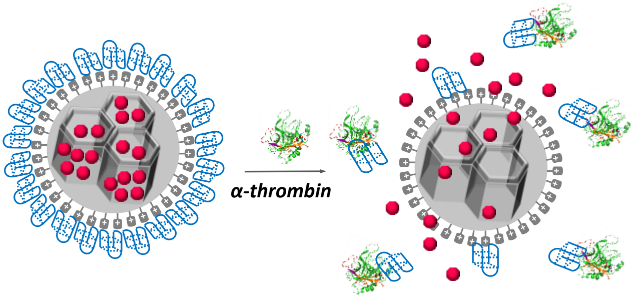

An aptamer-gated silica mesoporous material for thrombin detection.

*Mar Oroval,[a,b,c] Estela Climent,[a,b,c] Carmen Coll,[a,b,c] Ramón Eritja,[*cd] Anna Aviñó,[c,d]*
María Dolores Marcos,[a,b,c] Félix Sancenón,[a,b,c] Ramón Martínez-Máñez[a,b,c] and*
Pedro Amorós[e]

[a] Centro de Reconocimiento Molecular y Desarrollo Tecnológico (IDM). Unidad Mixta Universitat Politècnica de València - Universitat de València, Spain
[b] Departamento de Química, Universidad Politécnica de Valencia, Camino de Vera s/n, 46022, Valencia, Spain. Email: rmaez@quim.upv.es
[c] CIBER de Bioingeniería, Biomateriales y Nanomedicina (CIBER-BBN), Spain
[d] Institute for Advanced Chemistry of Catalonia (IQAC), CSIC, Jordi Girona 18-26, E-08034 Barcelona, Spain
[e] Institut de Ciència del Materials (ICMUV), Universitat de València. P.O. Box 2085, E-46071 València, Spain

Received 25th March 2013, Accepted 25th April 2013
First published on the web 25th April 2013

Chem. Commun., ***2013****, 49, 5480 – 5482*
Reproduced with permission of Royal Society of Chemistry.

Chem. Commun., 2013, 49, 5480-5482.

An aptamer-capped mesoporous material for the selective and sensitive detection of α-thrombin in human plasma and serum has been prepared and characterised.

The design of stimuli-responsive nanoscopic gated systems involving biomolecules has recently drawn much attention. In particular, some biomolecules, especially enzymes,[1] have been used as stimuli to uncap gated-scaffolds, whereas others, such as saccharides,[2] antibodies,[3] peptides[4] or DNA,[5] have acted as capping agents. Capped materials have been used mainly in drug delivery applications. However, there are by far fewer examples of their use in sensing.[3] In the latter approach, the carrier system is loaded with a dye and the capped mechanism is designed so that only a target analyte is able to trigger the delivery of the cargo. Among the different biomolecules that could act as caps, aptamers are especially appealing to design gated nanodevices for sensing and targeting applications.[6]

Furthermore, α-thrombin is a coagulation protein that has many effects on the coagulation cascade and its determination can be used to understand thrombosis and homeostasis processes. This protein, also known as coagulation factor II, is a serine protease that converts soluble fibrinogen (factor I) into insoluble strands of fibrin (factor Ia).[7,8] The concentration of α-thrombin in blood varies considerably and can be virtually absent in healthy subjects. However in the coagulation process, the concentration of thrombin in blood ranges from nM to low µM levels.[9] Moreover, it is important to detect thrombin in blood serum for clinical and diagnostic applications.[10]

Recently, various aptasensors based on electrochemistry,[11] colorimetry,[12] fluorescence,[13] electrochemiluminescence,[14] and other techniques[15] for thrombin detection have been developed. For instance, electrochemical aptasensors for thrombin detection based on nanoparticle labeling have also been described. For labeling purposes, gold nanoparticles,[16] quantum dots[17] or carbon nanotubes[18] have been widely used. One of the most commonly used aptamers in the development of thrombin aptasensors is the 15-mer DNA aptamer d(5'-GGT TGG

TGT GGT TGG-3′), also known as the thrombin-binding aptamer (TBA),[19] which is able to bind selectively onto exosite I thrombin (fibrinogen-binding sites) with a high specificity versus other substances.[20]

Despite the above examples, as far as we know, the use of TBA gated-hybrid mesoporous materials to recognize thrombin has not yet been reported. By taking these facts into account, this work presents a new hybrid gated material for the fluorometric detection of α-thrombin. Based on our experience in the field of bio-gated hybrid materials for sensing applications[21] we report herein the preparation of aptamer-gated silica mesoporous supports for the selective and sensitive fluorogenic signaling of α-thrombin.

Scheme 1 shows the proposed paradigm for thrombin detection using capped mesoporous materials. MCM-41 mesoporous nanoparticles (diameter of *ca.* 100 nm) were selected as inorganic scaffolds and pores were loaded with a fluorophore (rhodamine B). Then the external surface of the loaded support was functionalised with 3-aminopropyltriethoxysilane (APTS) (solid **S1**). Aminopropyl moieties are partially charged at a neutral pH and should display electrostatic interactions with the negatively charged TBA aptamer. Addition of TBA yielded the final capped hybrid material **S1–TBA**. Specifically for the preparation of the gated material **S1–TBA**, 1.5 mg of **S1** were suspended in 1.5 mL of simulated human blood plasma (pH 7.25).[22] Then, 60 µL of TBA (28 µM) were added to 150 µL of the **S1** suspension. The final **S1–TBA** solid was isolated by centrifugation and washed with 300 µL of simulated human blood plasma to eliminate the residual dye and the free TBA.

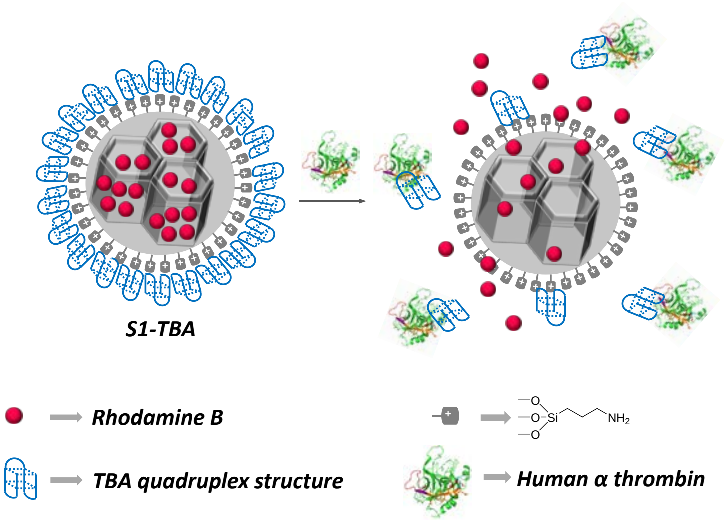

Scheme 1 Schematic representation of the gated material **S1** functionalised with 3-aminopropyltriethoxysilane and capped with a TBA aptamer in the quadruplex state (**S1–TBA**). The delivery of the entrapped guest (rhodamine B) is observed in the presence of α-thrombin.

S1 was characterised by standard procedures. The X-ray pattern of **S1** shows the mesoporous characteristic (100) peak diffraction, indicating that the loading process with the dye and the further functionalisation with APTS did not damage the mesoporous scaffolding (see Fig. S2, ESI†). The presence of the mesoporous structure in the final functionalised solids is also clearly observed from the TEM analysis (see Fig. S2, ESI†). The N_2 adsorption–desorption isotherms of the calcined MCM-41 nanoparticles (Fig. S3, ESI†) show an adsorption step with an intermediate P/P_0 value (0.1–0.3). From this curve, a pore volume of 0.84 cm^3 g^{-1} was calculated by the BJH model on the adsorption branch of the isotherm. The application of the BET model resulted in a value for the total specific surface area of 1066.8 m^2 g^{-1}. From the PXRD, porosimetry and TEM measurements, a pore diameter of 2.57 nm was determined. The N_2 adsorption–desorption isotherm of **S1** is typical of mesoporous systems with filled mesopores (see Fig. S3, ESI†), with the N_2 volume adsorbed and a surface area (77 m^2 g^{-1}) significantly decreased.

The dye and APTS contents on solid **S1** were determined by elemental analysis and thermogravimetric studies, and amounted to 0.092 and 1.65 mmol g^{-1} solid, respectively. Additionally, the TBA content in solid **S1–TBA** was determined by using aptamer TBA-flu (5′-GGT TGG TGT GGT TGG-fluorescein-3′), which is similar to TBA, but is functionalised with a fluorescein dye. By following the decreased absorbance of TBA-flu in the solution after the capping process and by monitoring the TBA-flu release in the uncapping experiments (see ESI† for details), we were able to calculate the TBA content to be 0.016 mmol per g of solid.

In order to investigate the gating properties of **S1–TBA**, 150 μg of **S1–TBA** were suspended in 1.5 mL of simulated human blood plasma and the suspension was divided into two fractions. The first fraction was diluted with 286 µL of Milli-Q water, whereas the second one was treated with 286 µL of an aqueous solution containing 2.89 μM of α-thrombin. In both cases, suspensions were stirred for 90 minutes at 37 °C and at certain times, interval fractions were taken and centrifuged to remove the solid. Dye delivery at a certain time was then measured by the fluorescence emission of rhodamine in the solution at 572 nm (λ_{exc} 555 nm). The delivery kinetics profile of rhodamine B in the presence and absence of target protein α-thrombin is shown in Fig. 1. In the absence of α-thrombin (curve a), solid **S1–TBA** showed negligible dye release, indicating tight pore closure. The delivery of the dye was induced when α-thrombin was present in the solution due to the displacement of the aptamer from the nanoparticles as a result of aptamer–thrombin recognition (curve b). After 60 minutes, *ca.* 80% of delivery was reached (31% of the total adsorbed rhodamine B in solid **S1–TBA**).

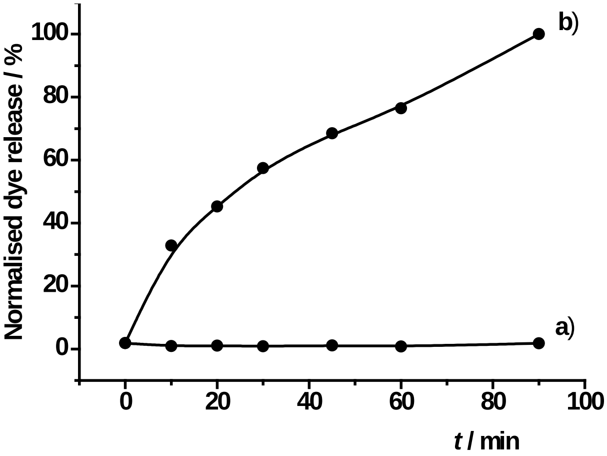

Fig. 1 Release profile of rhodamine B from the **S1–TBA** solid in the absence (a) and presence (b) of α-thrombin (2.89 μM) in simulated human blood plasma (pH 7.25).

Following a similar procedure, the delivery of rhodamine B from **S1–TBA** took place in accordance with the amount of α-thrombin; the results are shown in Fig. 2. As seen, the delivered cargo was proportional to the α-thrombin concentration, which is in agreement with the uncapping protocol detailed above. The maximum delivery was observed at an α-thrombin concentration of 1700 nM. Finally, a limit of detection of 2 nM (3*σ*) of α-thrombin was observed. One special feature of using gated materials for sensing applications is that it separates the recognition protocol (in our case, TBA–protein pair formation) from the signaling event, which means that sensing is independent of the stoichiometry of the host–guest complex, and sometimes, signal enhancement features are displayed. In our particular case, one molecule of α-thrombin was able to deliver *ca.* 115 molecules of dye at low α-thrombin concentrations (*ca.* 4 nM), which is a remarkable sign of signal amplification.

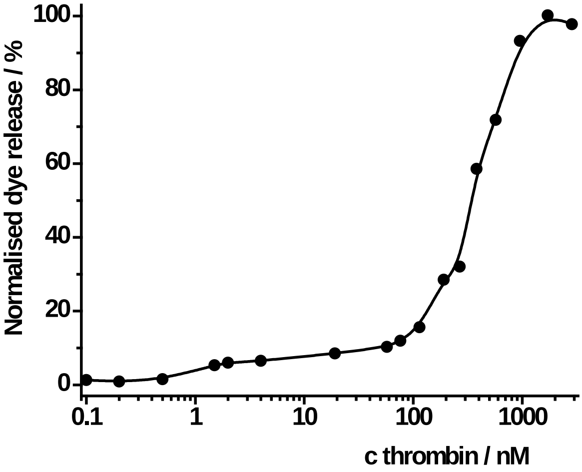

Fig. 2 Release of rhodamine B from **S1–TBA** in accordance with the concentration of α-thrombin added (after 60 min of reaction) in simulated human blood plasma (pH 7.25).

The *in vitro* characterisation of the nanodevice suggests that **S1–TBA** nanomaterial is sensitive to the presence of α-thrombin. Moreover, in order to study the possible application in the detection of α-thrombin in biological samples, **S1–TBA** was tested using commercially available human serum (from human male AB plasma). In a first step, the tolerance of the solid to human serum was studied by suspending 1 mg of **S1–TBA** in 1 mL of serum diluted with PBS (40, 20, 10 and 5%). From these measurements a 10% serum dilution showed the best response with a limit of detection as low as 4 nM for α-thrombin (3*σ*; see Fig. S4 and the experimental details in the ESI†). In a second step, and in order to verify the feasibility of the developed method, we prospectively used solid **S1–TBA** to determine α-thrombin in human serum. For this purpose, and in a typical experiment, human serum samples were spiked with 75, 150 and 300 nM of α-thrombin, respectively. Samples were diluted with PBS for a final amount of 10%, and the human α-thrombin contents were determined with **S1–TBA** material by the addition standard method. The obtained results are shown in Table S4 (ESI†). Remarkable recoveries in the range of 91–120% of thrombin were achieved.

In order to further investigate the selectivity of the **S1–TBA** material, control release experiments were carried out in the presence of other non-specific binding proteins (OVA and BSA). In particular, the PBS containing 10% human serum was spiked with 56 nM of OVA and BSA and rhodamine B released after 15 min was measured. Fig. 3 shows that a mixture of OVA and BSA was unable to induce the uncapping of pores, which reinforces the selective thrombin–TBA interaction as the mechanism of the fluorogenic response observed.

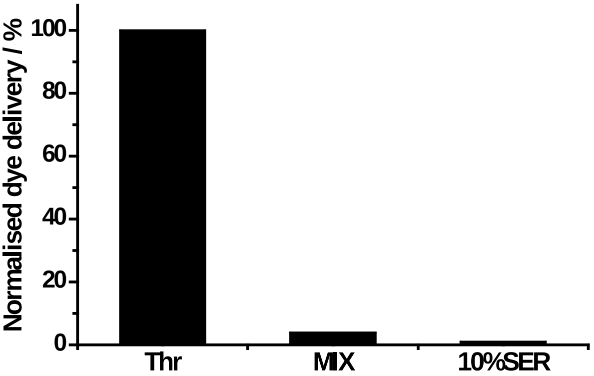

Fig. 3 Fluorescence of rhodamine B released from **S1–TBA** suspensions (in PBS containing 10% human serum) in the presence of α-thrombin (56 nM), and a mixture of OVA and BSA (56 nM) after 15 minutes of the addition. For comparative purposes, the release of rhodamine B from the **S1–TBA** suspensions in PBS containing 10% human serum is also shown.

In conclusion, we have prepared an aptamer-gated delivery system (**S1–TBA**) for the fluorogenic detection of thrombin. The sensing mechanism arises from the high affinity between an aptamer (TBA) and its target protein (α-thrombin). *In vitro* studies on **S1–TBA** showed a limit of detection of 2 nM (3σ) for α-thrombin. In addition, the hybrid nanomaterial allowed accurate α-thrombin detection in human serum diluted with PBS, also with high sensitivity (limit of detection of 4 nM (3σ)). The method, based on a simple competitive procedure, is undemanding and suggests that the use of aptamers can be a suitable approach to develop gated nanoparticles for simple chromo-fluorogenic assays for a wide range of bio-applications.

Acknowledgements

The authors thank the Spanish Government (project MAT2012-38429-C04-01, CTQ2010-20541) the Generalitat Valenciana (project PROMETEO/2009/016) and the CIBER-BBN for their support. C.C. thanks the Universitat Politècnica de València (UPV PAID-06-11) for support. M.O. is grateful to the Universitat Politècnica de València for her grant.

References

1. a) K. Patel, S. Angelos, W. R. Dichtel, A. Coskun, Y.–W. Yang, J. I. Zink and J. F. Stoddart, *J. Am. Chem. Soc.,*2008*,* **130**, 2382; b) A. Schlossbauer, J. Kecht and T. Bein, *Angew. Chem. Int. Ed.*, 2009,**48**, 3092; c) A. Bernardos, E. Aznar, M. D. Marcos, R. Martínez-Máñez, F. Sancenón, J. Soto, J. M. Barat and P. Amorós, P. *Angew. Chem. Int. Ed.*, 2009,**48**, 5884; d) C. Park, H. Kim, S. Kim and C. Kim, *J. Am. Chem. Soc.,*2009*,* **131**, 16614; e)P. D. Thornton and A. Heise, *J. Am. Chem. Soc.,*2010,**132**, 2024.
2. A. Bernardos, L. Mondragón, E. Aznar, M. D. Marcos, R. Martínez-Máñez, F. Sancenón, J. Soto, J. M. Barat, E. Pérez-Payá, C. Guillem and P. Amorós, *ACS Nano*, 2010, **4**, 6353.
3. a) E. Climent, A. Bernardos, R. Martínez-Máñez, A. Maquieira, M. D. Marcos, N. Pastor-Navarro, R. Puchades, F. Sancenón, J. Soto and P. Amorós, *J. Am. Chem. Soc.,* 2009, **131**, 14075; b) E. Climent, R. Martínez-Máñez, A. Maquieira, F. Sancenón, M. D. Marcos, E. M. Brun, J. Soto, P. Amorós, *ChemistryOpen*, 2012, **1**, 251; c) E. Climent, D. Gröninger, M. Hecht, M. A. Walter, R. Martínez-Máñez, M. G. Weller, F. Sancenón, P. Amorós, and K. Rurack, *Chem. -Eur. J.*, 2013, **19**, 4117.
4. a) C. Coll, L. Mondragón, R. Martínez-Máñez, F. Sancenón, M. D. Marcos, J. Soto, P. Amorós and E. Pérez-Payá, *Angew. Chem. Int. Ed.*, 2011, **50**, 2138; b) F. Porta, G. E. M. Lamers, J. I. Zink and A. Kros, *Phys. Chem. Chem. Phys.,* 2011, **13**, 9982.
5. a) A. Schossbauer, S. Warncke, P. M. E. Gramlich, J. Kecht, A. Manetto, T. Carell and T. Bein, *Angew. Chem.Int. Ed.*, 2010, **49**, 4734; b) Y. Zhang, Q. Yuan, T. Chen, X. Zhang, Y. Chen and W. Tan, *Anal. Chem.*, 2012, **84**, 1956.
6. a) C.-L. Zhu, C.–H. Lu, X.–Y. Song, H.–H. Yang and X.–R. Wang, *J. Am. Chem. Soc.*, 2011, **133**, 1278; b) V. C. Özalp and T. Schäfer, *Chem.-Eur. J.,* 2011, **17**, 9893; c) L. Gao, Y. Cui, Q. He, Y. Yang, J. Fei and J. Li, Chem.–Eur. J., 2011, **17**, 13170; d) X. B Fu, F Qu, N. B. Li and H. Q Luo, Analyst , 2015, **137**, 1097.
7. C. A. Holland, A. T. Henry, H. C. Whinna and F.C. Church, *FEBS Lett.*, 2000,**484**, 87.

8. L. Francois and F.W. David, *Physiol. Rev.,* 1954, **34**, 722.
9. M.A. Shuman and P.W. Majerus, *J. Clin. Invest.*, 1976, **58**, 1249.
10. a) J. Zheng, G.-F. Chen, P.-G. He and Y.-Z.Fang, *Talanta*, 2010, **80**, 1868; b) Y. Wang, X.He, K. Wang, X. Ni, J. Su and Z. Chen, *Biosens. Bioelectron.*, 2011, **26**, 3536.
11. a) P.L. He, L. Shen, Y.H. Cao and D.F. Li, *Anal. Chem.,* 2007, **79**, 8024; b) J. Zhao, Y. Zhang, H. Li, Y. Wen, X. Fan, F. Lin, L. Tan and S. Yao, *Biosens. Bioelectron.,* 2011, **26**, 2297.
12. a) C.-K. Chen, C.-C. Huang and H.-T. Chang, *Biosens. Bioelectron*., 2010, **25**, 1922; b) T. Li, E. Wang and S. Dong, *Chem. Commun.*, 2008, 3654.
13. a) H.X. Chang, L.H. Tang, Y. Wang, J. H. Jiang and J.H. Li, *Anal.Chem.***2010**, **82**, 2341; b) K. A. Edwards, Y. Wang and A. J. Baeumner, *Anal Bioanal. Chem,* 2010, **398**, 2645.
14. a) X.-B.Yin, Y.-Y.Xin and Y. Zhao, *Anal. Chem.*, 2009, **81**, 9299; b) L. Fang, Z. Lü, H. Wei and E. Wang, *Anal. Chim. Acta,* 2008, **628**, 80; c) J.Wang, Y-Y. Shan, W. Zhao, J-J. Xu and H-Y. Chen, *Anal. Chem.,* 2011, **83**, 4004.
15. a) Q. Zhao, X.F. Lu, C.-G. Yuan, X.-F. Li and X.C. Le, *Anal.Chem.*, 2009, **81**, 7484; b) J. Hu, P.-C. Zheng, J.-H. Jiang, G.-L.Shen, R.-Q. Yu and G.-K. Liu, . *Anal. Chem.*, 2009, **81**, 87.
16. C.F. Ding, Y. Ge and J. –M. Lin, *Biosens. Bioelectron.*, 2010, **25**, 1290.
17. a) C.F. Ding, Y. Ge and S.S. Zhang, *Chem.-Eur. J.,* 2010, **16**, 10707; b) Y. H. Tennico, D. Hutanu, M. T. Koesdjojo, C. M. Bartel and V. T. Remcho, *Anal. Chem.,* 2010, **82**, 5591.
18. M.T. Teresa, Y.-C. Tseng, N. Ormategui, I. Loinaz, R. Eritja and J. Bokor, *Nano Lett.,* 2009, **9**, 530.
19. L. C. Bock, L. C. Griffin, J. A. Latham and E. H. Vermaas, J. J. Toole, *Nature*, 1992, **355**, 564.
20. a) W. Bode, D. Turk and A. Karshikov, *Protein Sci.,* 1992, **1**, 426; b) M.T. Stubbs and W. Bode, *Thromb. Res.,* 1993, **69**, 1.
21. E. Climent, R. Martínez-Máñez, F. Sancenón, M. D. Marcos, J. Soto, A. Maquieira and P. Amorós, *Angew. Chem. Int. Ed.*, 2010, **49**, 7281.
22. M. R. C. Marques, R. Loebenberg and M. Almukainzi, *Dissolution Technol.,* 2011, **18**, 15.

Chem. Commun., 2013, 49, 5480-5482.

An aptamer-gated silica mesoporous material for thrombin detection.

SUPPORTING INFORMATION

Mar Oroval, Estela Climet, Carmen Coll, Ramón Eritja, Anna Aviñó,María Dolores Marcos, Félix Sancenón, Ramón Martínez-Máñez and Pedro Amorós.

Chemicals

The chemicals tetraethylorthosilicate (TEOS), n-cetyltrimethylammonium bromide (CTABr), sodium hydroxide (NaOH), rhodamine B, 3-aminopropyltriethoxysilane and human serum–from human male AB plasma (sterile-filtered) were provided by Aldrich. Human α-thrombin was provided by Haematologic Technologies Inc. Analytical-grade solvents were from Scharlab (Barcelona, Spain). All reactives were used as received.

General Techniques

PXRD, TG analysis, elemental analysis, TEM microscopy, N_2 adsorption-desorption and UV-visible spectroscopy techniques were used to characterize the prepared materials. X-ray measurements were performed on a Brücher AXS D8 Advance diffractometer using Cu-Kα radiation. Thermogravimetric analysis were carried out on a TGA/SDTA 851e Mettler Toledo equipment, using an oxidant atmosphere (Air, 80 mL/min) with a heating program consisting on a heating ramp of 10 °C per minute from 393 K to 1273 K and an isothermal heating step at this temperature during 30 minutes. TEM images were taken with a JEOL TEM-1010 Electron microscope working at 100 kV. N_2 adsorption-desorption isotherms were recorded on a Micromeritics ASAP2010 automated sorption analyser. The samples were degassed at 120 °C in vacuum overnight. The specific surfaces areas were calculated from the adsorption data in the low pressures range using the BET model. Pore size was determined following the BJH method. UV-visible spectroscopy was carried out with a Jasco V-630 Spectrometer. Fluorescence spectroscopy was carried out on a Jasco FP-8300 Spectrometer.

Buffer solutions

Phosphate buffered saline 1x (PBS 1x) consisting in 137 mM NaCl, 1.47 mM KH_2PO_4, 7.85 mM Na_2HPO_4, 2.68 mM KCl (pH: 7.5) was used for controlled release experiences.

Synthesis of the silica mesoporous nanoparticles support

The MCM-41 mesoporous nanoparticles were synthesized by the following procedure: *n*-cetyltrimethylammoniumbromide (CTABr, 1.00 g, 2.74 mmol) was first dissolved in 480 mL of deionized water. Then a 3.5 mL of NaOH 2.00 M in deionized water was added to the CTABr solution, followed by adjusting the solution temperature to 80 °C. TEOS (5 mL, 2.57. 10^{-2} mol) was then added dropwise to the surfactant solution. The mixture was allowed stirred for 2 h to give a white precipitate. Finally the solid product was centrifuged, washed with deionized water and dried at 60 °C (MCM-41 as-synthesized). To prepare the final porous material (MCM-41), the as-synthesized solid was calcinated at 550 °C using oxidant atmosphere for 5 h in order to remove the template phase.

Synthesis of S1

The amino-functionalised solid **S1** was prepared following literature procedures.[1] 500 mg of calcinated MCM-41 and 33.2 mg (0.10 mmol) of dye rhodamine B were suspended in 40 mL of acetonitrile inside a round-bottom flask connected to a Dean-Stark in an inert atmosphere. The suspension was refluxed (110 °C) in azeotropic distillation, collecting 10 mL in the trap in order to remove the adsorbed water. Then, the mixture was stirred during 24 hours at 36°C with the aim of achieving maximum loading in the pores of the MCM-41 scaffolding. Afterward an excess of 3-aminopropyltriethoxysilane (APTS, 0.936 mL, 4.0 mmol) was added, and the suspension was stirred for 5.5 h. Finally, the pink solid (**S1**) was filtered off and dried at 70 °C for 12h.

Synthesis of aptamers

The aptamers TBA d(5'-GGT TGG TGT GGT TGG-3') and TBA-flu d(5'-GGT TGG TGT GGT TGG-fluorescein-3') were synthesized in a 1 µmol scale using a 3400 Applied Biosystems DNA synthesizer following standard protocols. Ammonia deprotection was performed overnight at 55 °C. The resulting products were desalted by Sephadex G-25 (NAP-10, GE Healthcare) and used without further purification. Controlled pore glass (CPG) functionalised with fluorescein (3'-(6-FAM)-CPG, Link Technologies) was used for the introduction of fluorescein at the 3'-end of TBA.

Synthesis and optimization of solid S1-TBA

In order to estimate the proper amount of TBA for the preparation of **S1-TBA**, capping and release experiments in presence of different amounts of TBA were carried out. First of all, portions of 50 µL of a suspension of 1 mg **S1**/ mL PBS were added to a solution containing the aptamer TBA-flu d(5'-GGT TGG TGT GGT TGG-fluorescein-3') in concentrations of (0.02, 0.04, 0.06 and 0.08 µmol of TBA-flu g solid^{-1}) in Milli-Q water, and each suspension was stirred for 30 min at 37 °C, respectively. Afterwards, the absorbance of TBA-flu in the solution after the capping process was measured, in order to estimate the content of TBA-flu retained into solid. Results are shown in Table S1.

Table S1. Content of TBA added for the synthesis of **S1-TBA** and TBA retained during the process in mmol g^{-1} **S1**.

TBA added (mmol g^{-1} S1)	TBA retained (mmol g^{-1} S1)	% retained (mmol g^{-1} S1)
0.02	0.0123	61.55
0.04	0.0123	44.25
0.06	0.0123	22.44
0.08	0.0123	3.43

Some release studies were carried out. The isolated solids were divided in two parts. To one part, a solution of 250 µL PBS 1x containing human α-thrombin in concentrations of: 0.04, 0.06 and 0.08 µmol of thrombin g solid^{-1} were added and to the other part 250 µL PBS 1x were added. The suspensions were stirred for one hour; during this period two aliquots of the suspensions were taken. Finally, after centrifugation of all the aliquots the fluorescence of rhodamine B emission at 572 nm (λ_{ex} = 555nm) delivered to the solution was measured. It was found that all the concentrations were able to induce an effective capping of the pores, but in terms of dye release the concentration of the TBA at 0.04 mmol g solid^{-1}, showed more dye delivery than the others two TBA concentrations (0.06 and 0.08 mmol g solid^{-1}). Results are collected in Figure S1.

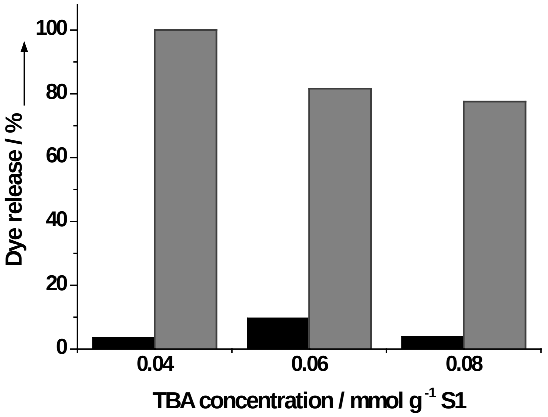

Figure S1. Optimization of the concentration of TBA to reach an effective capping of the pores. The black bars represent the blanks (absence of thrombin) and the grey bars represent the samples in presence of thrombin 0.04, 0.06 and 0.08 µmol of α-thrombin g solid^{-1}, respectively. All the measurements were carried out in PBS 1x (pH 7.5).

With the aim to obtain solid **S1-TBA,** 50 µL of a suspension of 1 mg **S1** in 1 mL PBS were suspended in 20 µL of a solution containing the aptamer TBA d(5'-GGT TGG TGT GGT TGG-3') in a concentration of 28.6 µM in Milli-Q water, and the suspension was stirred at 37 °C for 30 min. The final **S1-TBA** solid was isolated by centrifugation and washed with 100 µL of PBS buffer (pH 7.5) in order to remove the residual dye and the free aptamer TBA.

Materials Characterization

Solid **S1** was characterised using standard procedures. Figure S2 shows powder X-ray patterns of the nanoparticulated MCM-41 as synthesized support, calcinated MCM-41 and the **S1** functionalised material. The PXRD of siliceous nanoparticulated MCM-41 as-synthesized (curve a) shows four low-angle reflections typical of a hexagonal array that can be indexed as (100), (110), (200), and (210) Bragg peaks. A significant displacement of the (100) peak in the XRD powder of the nanoparticulated MCM-41 calcinated sample is clearly appreciated in the curve b, corresponding to an approximate cell contraction of 6.6 Å. This displacement and the broadening of the (110) and (200) peaks are related to further condensation of silanol groups during the calcination step. Finally, curve c corresponds to the **S1** XRD pattern. In this case, a loss of the (110) and (200) reflections is observed, most likely related to a loss of contrast due to the filling of the pore voids with the rhodamine B dye. Nevertheless, the value and intensity of the (100) peak in this pattern strongly evidences that the loading process with the dye and the further functionalisation with APTS have not damaged the mesoporous 3D MCM-41 scaffolding. The presence in the final functionalised solids of the mesoporous structure is also confirmed from the TEM analysis, in which the typical channels of the MCM-41 matrix are visualized as alternate black and white stripes (see Figure S2 for MCM-41 calcinated and solid **S1**). The figure also shows that the prepared MCM-41 and solid **S1** are obtained as spherical particles with diameters ranging from 100 to 200 nm.

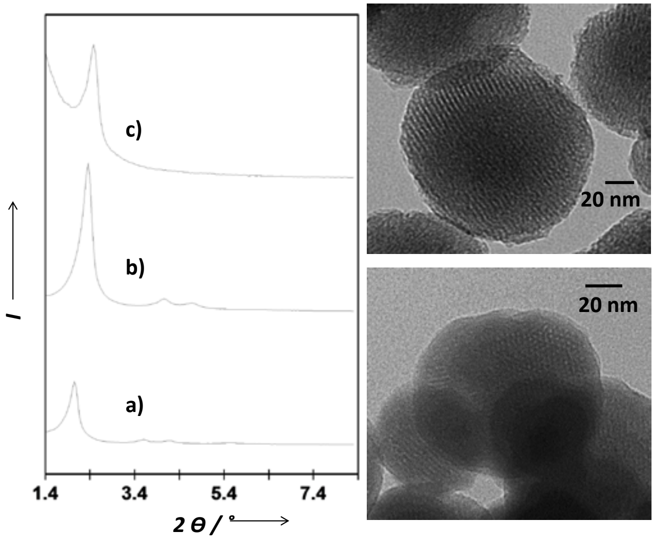

Figure S2. Left: powder X-ray patterns of the solids (a) MCM-41 as synthesized (b) calcinated MCM-41 and (c) solid **S1** containing the dye rhodamine B and functionalized with 3-aminopropyltriethoxysilane. **Right:** TEM images of (a) calcinated MCM-41 sample and (b) solid **S1** showing the typical hexagonal porosity of the MCM-41 mesoporous matrix.

The N_2 adsorption-desorption isotherms of the nanoparticulated MCM-41 calcinated material shows two sharp adsorption steps. The isotherm shows a first step at intermediate P/P_0 value (0.1-0.3) typical of these solids (see Figure S3, curve a). This step can be related to the nitrogen condensation inside the mesopores by capillarity. The absence of a hysteresis loop in this interval and the narrow BJH pore distribution suggests the existence of uniform cylindrical mesopores with pore volume of 0.84 $cm^3\ g^{-1}$ calculated by using the BJH model on the adsorption branch of the isotherm. The application of the BET model resulted in a value for the total specific surface of 1066.8 $m^2\ g^{-1}$. From the XRD, porosimetry and TEM studies, the a_0 cell parameter (43.16 Å), the pore diameter (2.57 nm) and a value for the wall thickness (1.74 nm) were calculated. In addition to this adsorption step associated to the micelle generated mesopores, a second feature appears in the isotherm at a high relative pressure ($P/P_0 > 0.8$). This adsorption correspond to the filling of the large voids among the particles and present a volume of 0.47 $cm^3\ g^{-1}$ (calculated by using the BJH model) and then must be considered as a textural-like porosity. In this case, the curves show a characteristic H1 hysteresis loop and a wide pore size distribution.

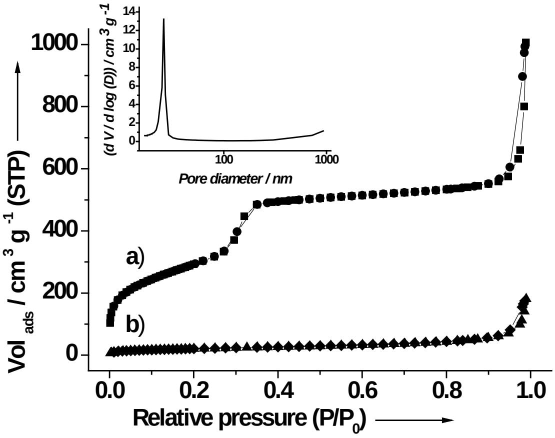

Figure S3. Nitrogen adsorption-desorption isotherms for (a) MCM-41 mesoporous material and (b) **S1** material. **Inset:** Pore size distribution of MCM-41 mesoporous material.

The N_2 adsorption-desorption isotherm of **S1** is typical of mesoporous systems with filled mesopores (see Figure S3, curve b), and a significant decrease in the N_2 volume adsorbed and surface area (0.06 cm^3 g^{-1} and 77.1 m^2 g^{-1} respectively) is observed. The most relevant feature is the absence of a sharp step at low-medium relative pressure ($0.1 < P/P_0 < 0.4$). In fact, this solid shows flat curves when compared (at the same scale) to those of the MCM-41 parent material, this indicates a significant pore blocking and the subsequent absence of appreciable mesoporosity. Additionally, a certain textural porosity is preserved. BET specific surface values, pore volumes, and pore sizes calculated from the N_2 adsorption-desorption isotherms for MCM-41 and **S1** are listed in Table S2.

Table S2. BET specific surface values, pore volumes and pore sizes calculated from the N_2 adsorption-desorption isotherms for selected materials.

Sample	S_{BET} (m^2 g^{-1})	Pore volume^a (cm^{-3} g^{-1})	Pore diameter ^{a}(nm)
MCM-41	1066.8	0.84	2.57
S1	77.1	0.06	-

^{a}Volume (V) and diameter (D) of mesopore.

The content of APTS and rhodamine B in the prepared solids **S1** and **S1-TBA** were determined by elemental analysis, thermogravimetric and delivery studies. Values of content are detailed in Table S3. The thermal analysis of the **S1** shows typical behaviour in functionalised mesoporous materials; i.e. a first weight loss between 25 and 150 °C related to the solvent evolution, a second step, between 150 and 800 °C due to the combustion of the organics and a final loss in the 800 - 1000 °C range related to the condensation of the silanol groups. In addition, from elemental analysis of C, H, N, S it is possible to determine the amount 3-aminopropyltriethoxysilane and rhodamine B contained in the materials calculated in millimole per gram of **S1** (mmol g^{-1} **S1**) using equation 1:

$$\alpha_A = \frac{\Delta W_i\% \times 1000}{\Delta W_{SiO_2}\% \times nM_i}\left(\frac{mmol}{g\,S1}\right)(1)$$

where $\Delta Wi\%$ (i = C, N, S) are the weight percentages of carbon, nitrogen or sulphur, M_i is the corresponding atomic weight and n is the number of the corresponding atom type in one molecule. $\Delta W_{SiO2}\%$ is the inorganic SiO_2 content in weight percentage. In addition, the content of dye in solid **S1-TBA** was determined from the dye content in **S1** after interaction with TBA aptamer, and determining the amount of dye delivered when washing the solids. Also, the amount of dye delivered from **S1-TBA** in the presence of thrombin was determined by using values of intensity of the fluorescence bearing in mind that, at low concentrations, relation between concentration and intensity are linear. Values of content are detailed in Table S3.

Table S3. Content of APTS and rhodamine B in the prepared solids **S1** and **S1-TBA** in mmol g^{-1} SiO_2.

Solid	α_{APTS} (mmol g^{-1} SiO_2)	$\alpha_{Rhodamine\ B}$ (mmol g^{-1} SiO_2)	α_{TBA} (mmol g^{-1} SiO_2)
S1	1.65	0.092	-
S1-TBA	1.65	0.057	0.0164

Taking into account the different amounts of APTS and aptamer TBA in solid **S1-TBA** it is possible to estimate the distribution of aptamer onto surface. Using these values, we can estimate that **S1-TBA** material contains 9.87 x 10^{18} oligonucleotide molecules/g solid. Additionally, considering surface value of **S1** calculated from N_2 adsorption measurements (77.1 m^2 g^{-1}) and the aptamer content calculated previously, the average surface coverage on solid **S1-TBA** by aptamer molecules is 0.36 molecules nm^{-2}. This aptamer surface coverage resulted in an average distance between aptamer molecules of about 2.8 nm. On the other hand, and bearing in mind again a typical value of external surface of **S1** (77.1 m^2 g^{-1}) and the content of APTS (in mmol g^{-1} SiO_2) calculated with elemental analysis and thermogravimetric studies, the average surface coverage on solid **S1-TBA** by APTS molecules is 12.8 molecules nm^{-2}. Finally, using the aptamer and APTS contents calculated previously a ratio of 100 APTS molecules aptamer $molecule^{-1}$ was estimated.

In vitro characterisation of S1-TBA in simulated human blood plasma

With the aim to study the possible application of **S1-TBA** for real sample analysis, we tested **S1-TBA** in simulated human blood plasma. Thus, the response of **S1-TBA** in presence of several amounts of α-thrombin in simulated human blood plasma[2] was studied. In the absence of α-thrombin, solid **S1-TBA** showed negligible dye release, whereas an enhancement in the emission intensity at 572 nm was observed upon addition of increasing quantities of α-thrombin. In this case, the maximum delivery of the dye was observed at an α-thrombin concentration of 1700 nM, showing a limit of detection of 2 nM. Figure S4 shows the fluorescence emission spectra of rhodamine B from **S1-TBA** in absence and in presence of different amounts of α-thrombin.

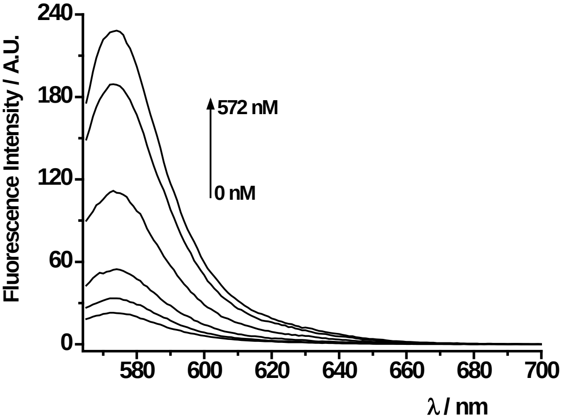

Figure S4. Fluorescence emission spectra of the rhodamine B delivered from **S1-TBA** in the presence of different concentrations of α-thrombin in simulated human blood plasma (pH 7.25). From top to bottom: 572, 381, 267, 190, 114, 19 and 0 nM. (λ_{exc} = 555 nm).

In vitro characterisation of S1-TBA in human serum

The delivery experiments of **S1-TBA** in human blood plasma showed faster response than the response observed in simulated human blood plasma (related with stronger ionic strength), showing a tolerance of the system using 10% of human serum. Calibration curve for thrombin containing 10% of human serum was obtained (Figure S5), showing the maximum delivery of the dye at 15 min employing 98.82 nM of thrombin.

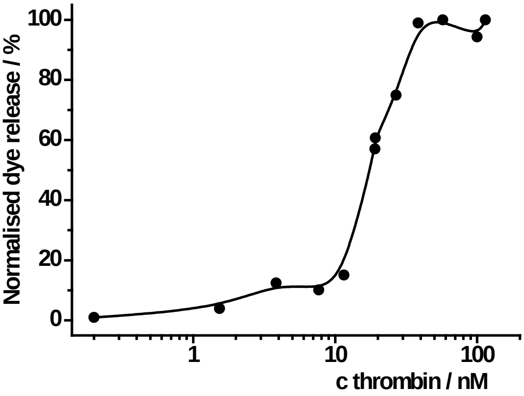

Figure S5. Release of rhodamine B from solid **S1-TBA** as a function of the concentration of human α-thrombin in PBS containing 10% of human serum – from human male AB plasma.

Determination of thrombin in human serum I

With the aim to verify the feasibility of the developed method, we prospectively used solid **S1-TBA** for the determination of thrombin in human serum. For this purpose, in a typical experiment, three portions of 1 mL of human serum sample were spiked with 75, 150 and 300 nM of thrombin, respectively. Samples were diluted with PBS for a final amount of 10%, and finally each sample was doped with different amounts of human thrombin in order to obtain a calibration curve by standard addition. Then, 40 µL of each doped sample was carefully added to 100 µL of **S1-TBA** suspension (12 µg in 140 µL) in order to prepare a calibration curve. After 15 minutes, the suspensions were centrifuged (3 min at 7000 rpm) and the emission intensity of rhodamine B (λ_{ex} = 555 nm) at 572 nm was measured in the solution. These fluorescence intensities at 572 nm plotted vs. human thrombin concentration yielded three calibration curves (data not shown). The content of α-thrombin spiked in human serum was calculated through the difference between the y-intercept of the calibration curve and the residual emission of a blank solution divided by the slope of the calibration curve. The obtained results are shown in Table S4. As can be seen, remarkable recoveries in the range of 91-120% of thrombin were achieved.

Table S4. Determination of thrombin in 10% human serum samples.

Thrombin added (nM)	**Thrombin found (nM)**	**Recovery (%)**
75	68.35 ± 5.56	091
150	147.32 ± 4.08	98
300	361.22 ± 60.47	120

References

1. E. Climent, R. Martínez-Máñez, F. Sancenón, M. D. Marcos, J. Soto, A. Maquieira, P. Amorós, *Angew. Chem. Int. Ed.* 2010, **49**, 7281.
2. M. R. C. Marques, R. Loebenberg and M. Almukainzi, *Dissolution Technol.,* 2011, **18**, 15.

3. Selective fluorogenic sensing of As(III) using aptamer-capped nanomaterials

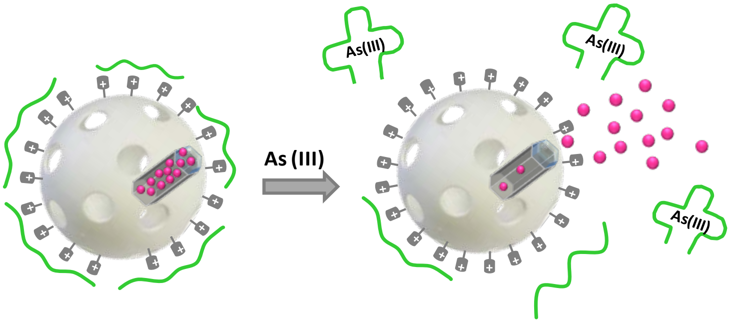

Selective fluorogenic sensing of As(III) using aptamer-capped nanomaterials.

Mar Oroval, [‡,†,∥] *Carmen Coll,* [‡,†,∥] *Andrea Bernardos,* [‡,†,∥] *María D. Marcos,* [‡,†,∥]
*Ramón Martínez-Máñez,** [‡,†,∥] *Dmitry G. Shchukin**[⊥] *and Félix Sancenón*[‡,†,∥]

[‡]. Instituto Interuniversitario de Investigación de Reconocimiento Molecular y Desarrollo Tecnológico. Unidad Mixta Universitat Politècnica de València - Universitat de València. Camino de Vera s/n, 46022, Valencia, Spain.
[†]. CIBER de Bioingeniería, Biomateriales y Nanomedicina (CIBER-BBN).
[∥]. Departamento de Química, Universitat Politècnica de València, Camino de Vera s/n, 46022, València, Spain.
[⊥]. Chemistry Department, Stephenson Institute for Renewable Energy, The University of Liverpool, Chadwick Building, Peach Street, Liverpool, L69 7ZF (UK).

Submitted to ACS Applied Materials and Interfaces

Organic-inorganic hybrid nanomaterials offer extremely valuable tools for monitoring many types of analytes in solution. Within this framework, aptamer-based nanomaterials for heavy metal detection are still very scarce. Herein, a novel sensing nanoprobe for the selective and sensitive detection of As(III) based on the combination of aptamers with mesoporous silica nanoparticles has been developed. The efficiency of the sensor is demonstrated in environmental conditions, showing a great potential in As(III) monitoring assays.

Arsenic poisoning is becoming a severe worldwide threat to human health, due to the numerous diseases, including high risk of cancer, associated with drinking water contaminated with arsenic.[1] The U.S. Environmental Protection Agency (EPA) recently readjusted the maximum contaminant level for arsenic in drinking water from 50 µg L^{-1} to 10 µg L^{-1}.[2] This change motivated many researchers to develop new sensitive techniques for monitoring arsenic that can accomplish with the new standard.[3] The predominant forms of arsenic found in aqueous environments are arsenite (As(III) as H_3AsO_3,) and arsenate (As(V) as H_3AsO_4).[4] Between these two most common forms of arsenic species in water, As(III) has been identified as the most harmful and in fact it is 100 times more toxic than As(V).[5] Traditional methods for arsenic detection are atomic fluorescence spectrometry, atomic absorption spectrometry and inductively coupled plasma optical emission spectrometry.[6,7] Although, these methods can accurately measure arsenic, most of them require expensive and sophisticated equipment accompanied with complex sample pre-treatments. In this scenario, the development of simple, sensitive and reliable procedures for As(III) sensing in drinking water becomes to be a necessity. Very recently, as an alternative to these traditional methods, chromogenic and fluorogenic chemosensors for an accurate and sensitive As(III) detection using quantum dots,[8] cysteine-functionalized tetraphenylethenes[9] and coumarin-appended benzothiazolines[10] have been described.

In this context, nanostructured sensors have been reported to offer many advantages, to such an extent, that they can be considered as the new generation of sensing systems able to provide rapid and sensitive responses.[11] Compared with other potential nanomaterials used in sensing protocols, mesoporous silica nanoparticles (MSNs) are ones of the most promising supports due to their remarkable properties such as high inner surface area and flexible surface-modification chemistry.[12–14] Moreover, MSNs can be functionalized with (bio)chemical or supramolecular ensembles than acted as “molecular gates” for the development of stimuli-responsive systems able to release an entrapped cargo due to the presence of certain and well defined stimuli.[15,16] These capped materials have been recently applied in sensing protocols. For this purpose, gated MSNs are loaded with a reporter which is selectively delivered to the solution in the presence of a target analyte.[13,17]

On the other hand, the development of sensory systems using aptamers has attracted a great interest to detect trace amounts of many different type of analytes.[18] Aptamers are DNA sequences with long-term stability, high affinity and selectivity for target proteins, small molecules or ions.[18–20] Aptamer production is based on a selection method called SELEX (Systematic Evolution of Ligands by Exponential enrichment) and their use in the sensing field has resulted in the design of ultrasensitive systems to detect a number of different analytes. In the field of gated chemistry, aptamers-containing materials for the recognition of ATP, potassium, adenosine and thrombin have been recently reported.[21–24]

Taking into account the above mentioned facts we envisioned the use of aptamer-capped MSNs as potential supports for the design of As(III) sensing systems. Our proposed sensing paradigm is showed in Scheme 1. As inorganic scaffold, MCM-41 mesoporous silica nanoparticles (*ca.* 100 nm) were selected due to their remarkable features for the design of capped materials.[25] The pores of the MCM-41 inorganic support were loaded with rhodamine B and then the external surface was functionalized with aminopropyl moieties. The final capped solid was prepared by addition of an As(III) aptamer. The presence of As(III) is expected to induce unblocking of the pores, via an effective displacement of the aptamer from the MSNs surface, with subsequent dye delivery.

MCM-41 nanoparticles were obtained in alkaline media using previously described procedure.[26] To prepare **S1** solid, calcined MCM-41 was suspended in a solution of rhodamine B in acetonitrilie and the mixture was stirred to achieve the maximum loading of the pores. Afterwards, (3-aminopropyl)triethoxysilane (APTES) was grafted onto the external nanoparticles' surface to produce **S1** (see Supporting Information for details). To cap the pores we used a 100-mer DNA aptamer (Ars-3) which possesses a very high affinity to As(III) (K_d = 7.05 nM).[27] This aptamer has been used for the detection of As(III) using gold nanoparticles[28–31] but, as far as we know, the use of Ars-3 in gated-hybrid mesoporous materials has not been reported. Addition of Ars-3 aptamer to a suspension of S1 in HEPES buffer (pH 7.2) resulted in the capping of the pores by means of electrostatic interactions between the positively charged aminopropyl moieties and the negatively charged aptamer, yielding the final material **S1-Ars-3** (Scheme 1 and see Supporting Information for detailed description).

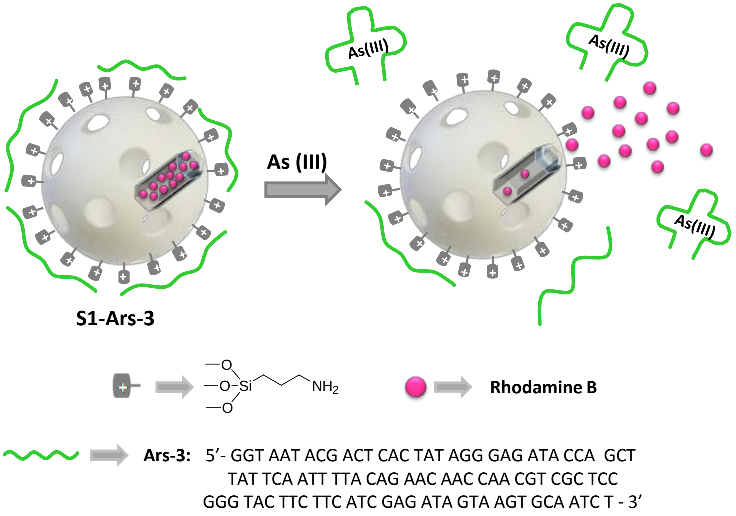

Scheme 1. Representation of the gated material **S1-Ars-3** functionalized with aminopropyl moieties and capped with Ars-3 aptamer. Delivery of the entrapped dye (rhodamine B) is specifically accomplished in the presence of As(III).

The starting MCM-41 mesoporous nanoparticles and solid **S1** were characterized following standard procedures (see Supporting Information for details). Powder X-ray diffraction (PXRD) and transmission electron microscopy

(TEM), carried out on the starting MCM-41 mesoporous nanoparticles, clearly showed the presence of a mesoporous structure that persisted in solid **S1** regardless of the loading process with rhodamine B and further functionalization with (3-aminopropyl)triethoxysilane (see Figure 1). The size of the prepared nanoparticles was assessed by TEM images, which gave an average particle diameter of *ca.* 100 ± 13 nm (see also Figure 1). BET specific surface area, pore volume and pore size were calculated from the N_2 adsorption-desorption measurements. Table 1 summarizes the most relevant structural features obtained from these studies. Particle diameter (studied by DLS in HEPES buffer at pH 7.2) increased after each surface modification. Diameters of 123.5, 165.1 and 190.0 nm were found for MCM-41, **S1** and **S1-Ars-3,** respectively. Moreover, from elemental analysis and thermogravimetric studies the contents of rhodamine B and aminopropyl moieties in solid **S1** were calculated to be 0.12 and 2.73 mmol $gSiO_2^{-1}$, respectively.

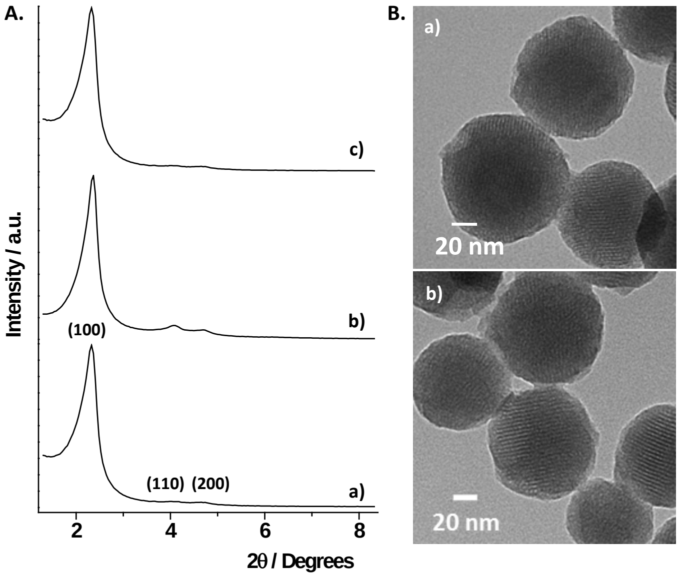

Figure 1. A: Powder X-ray patterns of the solids: (a) MCM-41 as synthesized, (b) calcined MCM-41 and (c) solid **S1**. B: Representative TEM images of: (a) calcined MCM-41 sample and (b) solid **S1**.

Table 1. Main structural properties calculated from TEM, PXRD and N_2 adsorption-desorption analysis of MCM-41 and S1.

Sample	S_{BET} ($m^2 g^{-1}$)	Pore Volume [a] ($cm^3 g^{-1}$)	Pore size [a] (nm)
MCM-41	888	0.72	2.59
S1	227	014	-

To assess the feasibility of the proposed sensing paradigm, controlled release experiments from **S1-Ars-3** in the presence of As(III) dissolved in aqueous media were carried out. In a typical experiment, 150 µg of **S1-Ars-3** were suspended in 1.5 mL of HEPES buffer (pH 7.2) and the suspension was divided in two fractions. The first fraction was diluted to 900 µL with Milli-Q water as a control experiment. On the other hand, the second fraction was diluted with a stock solution of As(III) in Milli-Q water to reach a concentration of 100 ppb of As(III) in a final volume of 900 µL. Both suspensions were stirred at room temperature and aliquots were taken at certain programmed times (0, 5, 10, 15 25, 30 and 35 min). The aliquots were centrifuged to eliminate the solid, and cargo release was evaluated by measuring the fluorescence emission of rhodamine B in the supernatant centred at 572 nm (λ_{ex}= 555). Delivery kinetic profiles of rhodamine B both in the presence and absence of As(III) are shown in Figure 2a. As could be seen, in the absence of the target analyte, solid **S1-Ars-3** showed poor rhodamine B release of 1.2 µmol g **S1-Ars-3**$^{-1}$ (*ca.* 5% of the maximum dye delivered after 25 min) indicating a tight pore closure (curve a in Figure 2). However, in the presence of 100 ppb of As(III), a clear rhodamine B delivery was observed (curve b in Figure 2) that reaches nearly 80% (*ca*. 22 µmol/g **S1-Ars-3**) of the maximum dye delivered after *ca*. 25 min. The observed rhodamine B release was a result of the As(III)-induced displacement of the capping aptamer from the nanoparticles' surface. As(III) has been reported to form highly stable complexes with Ars-3 through strong hydrogen bond interactions of the hydroxyl groups of aqueous As(III) with amine groups of nucleobases in the aptamer chain.[27]

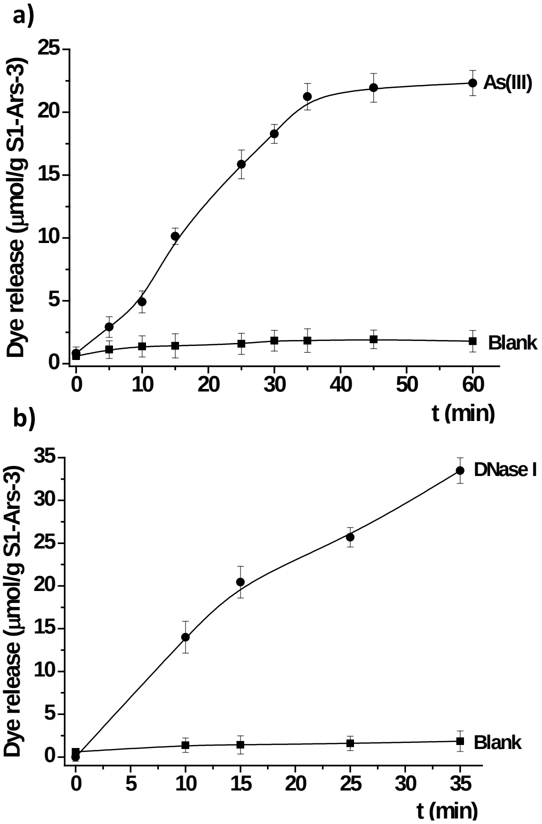

Figure 2. (a) Release profile of rhodamine B from **S1-Ars-3** in the absence (blank) and in the presence of As(III) (100 ppb) (As(III)) in HEPES buffer (pH 7.2). (b) Delivery of rhodamine B from solid **S1-Ars-3** in the absence (blank) and in the presence of 55 U µL^{-1} of DNAse I enzyme (DNase I).

To reinforce the demonstration of the proper interaction of aptamer Ars-3 with solid **S1**, release experiments in presence of DNAse I enzyme were carried out. Results in the presence of DNAse I enzyme, showed a remarkable dye release from solid **S1-Ars-3**, indicating the essential role of the Ars-3 aptamer in the capping mechanism (see Figure 2b).

In a further step, the sensitivity of the prepared nanocarrier towards As(III) was evaluated. In this experiment dye released after 35 min from **S1-Ars-3** in the presence of different amounts of As(III) was studied. As seen in Figure 3 rhodamine B delivery was proportional to the As(III) concentration, which is in agreement with the proposed uncapping protocol involving the displacement of Ars-3 from the surface of solid **S1-Ars-3**. From these experiments a linear response in the 4–60 ppb As(III) concentration range was found. Furthermore, a limit of detection (LOD) as low as 0.9 ppb was determined. This LOD is *ca.*10-fold below the EPA toxicity level of arsenic in drinking water (10 ppb).[2] The calculated LOD indicates a noteworthy sensitivity of the nanoprobe, and confers our system a competitive basis with other As(III) aptameric sensors based on colorimetric,[28–30] fluorometric[31] and resonance Rayleigh scattering[28,33] measurements (see Table S5 in Supporting Information).

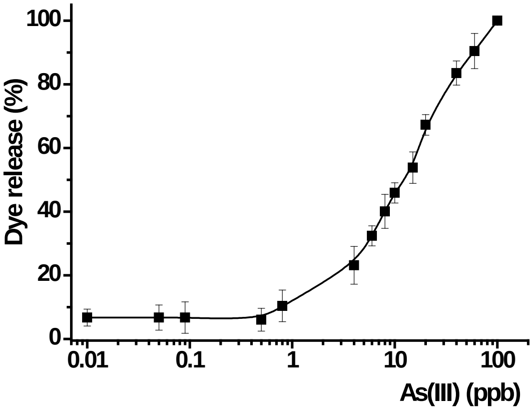

Figure 3. Release of rhodamine B from solid **S1-Ars-3** in the presence of increasing quantities of As(III) in HEPES buffer (pH 7.2) after 35 min of addition.

The next step was to verify the selectivity of **S1-Ars-3** solid. For this purpose, cargo release from **S1-Ars-3** was tested in water containing 50 ppb of As(III), As(V), Ag(I), Pb(II), K(I), Na(I), Fe(III), Fe(II), Mg(II) and Ca(II) cations. As shown in Figure. 4, As(III) is the only cation able to induce a remarkable payload delivery, whereas other metal ions tested induced poor pore opening and negligible dye release. This observation corroborates the selective As(III)-aptamer interaction as the main mechanism of the fluorogenic response observed.

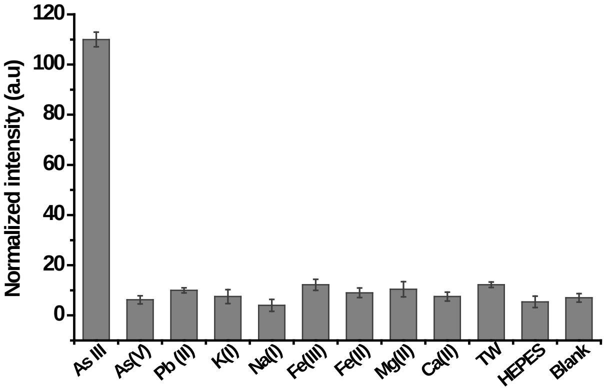

Figure 4. Release or rhodamine B from **S1-Ars-3** in the presence of different ions at a concentration of 50 ppb after 35 min of addition. Two control experiments were carried out with Milli-Q water (blank), with HEPES buffer at pH 7.2 (HEPES), and with tap water (TW).

Motivated by the excellent properties displayed by **S1-Ars-3**, we took a step forward and tested the performance of the capped material for the determination of As(III) in an environment conditions. With this aim, in a typical experiment, tap water samples were spiked with 4, 6 and 10 ppb of As(III), respectively and the concentration of As(III) was determined using a calibration curve obtained using **S1-Ars-3** solid. Table 2 shows the concentration of As(III) determined in the spiked samples using **S1-Ars-3**. Recovery levels were within the 91-109%range indicating the suitability of **S1-Ars-3** nanoparticles for the determination of As(III) ions in a real environment.

Table 2. Determination of As(III) in tap water samples.

As(III) added (ppb)	As(III) found (ppb)	Recovery %
4	3.6 ± 0.1	91
6	6.5 ± 0.2	108
10	11.0 ± 1.2	109

In summary, we have successfully developed a novel fluorogenic sensing probe for As(III) by combining MSNs with aptamers as capping agents. The sensing mechanism relies on the specific interaction between the capping aptamer (Ars-3) and the As(III). The prepared nanoprobe showed a remarkable LOD of 0.9 ppb. In

addition, the hybrid nanomaterial allowed accurate As(III) determination in tap water samples. As far as we know, this is the first time that aptamer-capped mesoporous supports are used for the detection of As(III). The presented approach is simple and undemanding, and we believe that possesses the potential of finding application in environmental analysis protocols.

Keywords: Hybrid materials, sensing, silica nanoparticles, arsenic, nanomaterials.

Acknowledgements

The authors thank the financial support from the Spanish Government (projects MAT2015-64139-C4-1-R and AGL2015-70235-C2-2-R) and the Generalitat Valenciana (project GVA/2014/13). M.O. is grateful to the Universitat Politècnica for her PhD grant. A.B. thanks the Spanish Government for the finantial support "Juan de la Cierva-Incorporación" (IJCI-2014-21534). C.C. thanks the Generalitat Valenciana for her postdoctoral contract VALi+D.

References.

1. Mandal, B. K.; Suzuki, K. T. Arsenic Round the World: A Review. *Talanta* **2002**, *58* (1), 201–235.
2. *United States Environ. Prot. Agency. Arsen. Clarifications to Compliance New Source Monit. Rule A Quick Ref. Guide. EPA 816-F-01-004; US EPA Washington, DC, 2001; http//www.epa.gov/safewater/arsenic/compliance.html (accessed* 10/ **2015)**.
3. Yang, B.; Chen, X.; Liu, R.; Liu, B.; Jiang, C. Target Induced Aggregation of Modified Au@Ag Nanoparticles for Surface Enhanced Raman Scattering and its Ultrasensitive Detection of Arsenic in Aqueous Solution. *RSC Adv.* **2015**, *5* (95), 77755–77759.
4. Bissen, M.; Frimmel, F. H.; Ag, C. Arsenic – A Review . Part I : Occurrence , Toxicity , Speciation , Mobility. *Acta Hydrochim. Hydrobiol.* **2003**, *31*, 9–18.
5. Tuzen, M.; Saygi, K. O.; Karaman, I.; Soylak, M. Selective Speciation and Determination of Inorganic Arsenic in Water, Food and Biological Samples. *Food Chem. Toxicol.* **2010**, *48* (1), 41–46.
6. Aggett, J.; Aspell, A. C. The Determination of Arsenic(III) and Total Arsenic by Atomic-Absorption Spectroscopy. *Analyst* **1976**, *101* (1202), 341–347.

7. Yan, X.-P.; Kerrich, R.; Hendry, M. J. Determination of (Ultra)trace Amounts of Arsenic(III) and Arsenic(V) in Water by Inductively Coupled Plasma Mass Spectrometry Coupled with Flow Injection On-Line Sorption Preconcentration and Separation in a Knotted Reactor. *Anal. Chem.* **1998**, *70* (22), 4736–4742.
8. Zhou, Y.; Huang, X.; Liu, C.; Zhang, R.; Gu, X.; Guan, G.; Jiang, C.; Zhang, L.; Du, S.; Liu, B.; Han, M. –Y.; Zhang, Z. Color-Multiplexing-Based Fluorescent Test Paper: Dosage-Sensitive Visualization of Arsenic(III) with Discernable Scale as Low as 5 ppb. *Anal. Chem.* **2016**, *88*, 6105-6109.
11. Li, M.; Gou, H.; Al-Ogaidi, I.; Wu, N. Nanostructured Sensors for Detection of Heavy Metals: A Review. *ACS Sustainable Chem. Eng.* **2013**, *1* (7), 713–723.
12. Zheng, Z.; Huang, X.; Shchukin, D. A Cost-Effective pHSensitive Release System for Water Source pH Detection. *Chem. Commun.* **2014**, *50*, 13936.
13. Sancenón, F.; Pascual, L.; Oroval, M.; Aznar, E.; Martínez-Máñez, R. Gated Silica Mesoporous Materials in Sensing Applications. *ChemistryOpen* **2015**, *4*, 418–437.
14. Aznar, E.; Oroval, M.; Pascual, L.; Murguía, J. R.; Martínez-Máñez, R.; Sancenón, F. Gated Materials for On-Command Release of Guest Molecules. *Chem. Rev.* **2016**, *116* (2), 561–718.
15. Zheng, Z.; Huang, X.; Schenderlein, M.; Moehwald, H.; Xu, G.; Shchukin, D. G. Bioinspired Nanovalves with Selective Permeability Andand pH Sensitivity. *Nanoscale* **2015**, *7*, 2409–2416.
16. Zheng, Z.; Huang, X.; Schenderlein, M.; Borisova, D.; Cao, R.; Möhwald, H.; Shchukin, D. Self-Healing and Antifouling Multifunctional Coatings Based on pH and Sulfide Ion Sensitive Nanocontainers. *Adv. Funct. Mater.* **2013**, *23* (26), 3307–3314.
17. Choi, Y. L.; Jaworski, J.; Seo, M. L.; Lee, S. J.; Jung, J. H. Controlled Release Using Mesoporous Silica Nanoparticles Functionalized with 18-Crown-6 Derivative. *J. Mater. Chem.* **2011**, *21* (22), 7882–7885.
18. Li, F.; Zhang, H.; Wang, Z.; Newbigging, A. M.; Reid, M. S.; X.-F. L.; X. C. Le. Aptamers Facilitating Amplified Detection of Biomolecules. *Anal. Chem.* **2015**, *87*, 274–292.
19. Oroval, M.; Coronado-Puchau, M.; Langer, J.; Sanz-Ortiz, M. N.; Ribes, Angela; Aznar, E.; Coll, C.; Marcos, M. D.; Sancenón, F.; Liz-Marzán, L. M.; Martínez-Máñez, R. Surface Enhanced Raman Scattering and Gated Materials for Sensing Applications: The Ultrasensitive Detection of Mycoplasma and Cocaine. *Chem. Eur. J.* **2016**, 13488–13495.
20. Özalp, V. C.; Çam, D.; Hernandez, F. J.; Hernandez, L. I.; Schäfer, T.; Öktem, H. a. Small Molecule Detection by Lateral Flow Strips via Aptamer-Gated Silica Nanoprobes. *Analyst* **2016**, *141*, 2595–2599.

21. He, X.; Zhao, Y.; He, D.; Wang, K.; Xu, F.; Tang, J. ATP-Responsive Controlled Release System Using Aptamer-Functionalized Mesoporous Silica Nanoparticles. *Langmuir* **2012**, *28* (35), 12909–12915.

22. Wen, Y.; Xu, L.; Li, C.; Du, H.; Chen, L.; Su, B.; Zhang, Z.; Zhang, X.; Song, Y. DNA-Based Intelligent Logic Controlled Release Systems. *Chem. Commun.* **2012**, *48* (67), 8410–8412.

23. Chen, L.; Wen, Y.; Su, B.; Di, J.; Song, Y.; Jiang, L. Programmable DNA Switch for Bioresponsive Controlled Release. *J. Mater. Chem.* **2011**, *21* (36), 13811–13811.

24. Oroval, M.; Climent, E.; Coll, C.; Eritja, R.; Aviñó, A.; Marcos, M. D.; Sancenón, F.; Martínez-Máñez, R.; Amorós, P. An Aptamer-Gated Silica Mesoporous Material for Thrombin Detection. *Chem. Commun.* **2013**, *49* (48), 5480–5482.

25. Argyo, C.; Weiss, V.; Bräuchle, C.; Bein, T. Multifunctional Mesoporous Silica Nanoparticles as a Universal Platform for Drug Delivery. *Chem. Mater.* **2014**, *26* (1), 435–451.

26. Coll, C.; Mondragón, L.; Martínez-Máñez, R.; Sancenón, F.; Marcos, M. D.; Soto, J.; Amorós, P.; Pérez-Payá, E. Enzyme-Mediated Controlled Release Systems by Anchoring Peptide Sequences on Mesoporous Silica Supports. *Angew. Chem. Int. Ed.* **2011**, *50* (9), 2138–2140.

27. Kim, M.; Um, H. J.; Bang, S.; Lee, S. H.; Oh, S. J.; Han, J. H.; Kim, K. W.; Min, J.; Kim, Y. H. Arsenic Removal from Vietnamese Groundwater Using the Arsenic-Binding DNA Aptamer. *Environ. Sci. Technol.* **2009**, *43* (24), 9335–9340.

28. Wu, Y.; Liu, L.; Zhan, S.; Wang, F.; Zhou, P. Ultrasensitive Aptamer Biosensor for Arsenic(III) Detection in Aqueous Solution Based on Surfactant-Induced Aggregation of Gold Nanoparticles. *Analyst* **2012**, *137* (18), 4171–4178.

29. Zhan, S.; Yu, M.; Lv, J.; Wang, L.; Zhou, P. Colorimetric Detection of Trace Arsenic(III) in Aqueous Solution Using Arsenic Aptamer and Gold Nanoparticles. *Aust. J. Chem.* **2014**, *67* (5), 813–818.

30. Divsar, F.; Habibzadeh, K.; Shariati, S.; Shahriarinour, M. Aptamer Conjugated Silver Nanoparticles for the Colorimetric Detection of Arsenic Ions Using Response Surface Methodology. *Anal. Methods* **2015**, *7* (11), 4568–4576.

31. Ensafi, A. A.; Kazemifard, N.; Rezaei, B. A Simple and Sensitive Fluorimetric Aptasensor for the Ultrasensitive Detection of Arsenic(III) Based on Cysteamine Stabilized CdTe/ZnS Quantum Dots Aggregation. *Biosens. Bioelectron.* **2015**, *77*, 499–504.

32. Kaur, H.; Kumar, R.; Babu, J. N.; Mittal, S. Advances in Arsenic Biosensor Development – A Comprehensive Review. *Biosens. Bioelectron.* **2015**, *63* (0), 533–545.
33. Wu, Y.; Zhan, S.; Xing, H.; He, L.; Xu, L.; Zhou, P. Nanoparticles Assembled by Aptamers and Crystal Violet for Arsenic(III) Detection in Aqueous Solution Based on a Resonance Rayleigh Scattering Spectral Assay. *Nanoscale* **2012**, *4* (21), 6841–6849.

Selective fluorogenic sensing of As(III) using aptamer-capped nanomaterials

SUPPORTING INFORMATION

Mar Oroval,[‡,†,∥] *Carmen Coll,*[‡,†,∥] *Andrea Bernardos,*[‡,†,∥] *María D. Marcos,*[‡,†,∥] *Ramón Mar-tínez-Máñez,*[*,‡,†,∥] *Dmitry G. Shchukin*[*⊥] *and Félix Sancenón*[‡,†,∥]

‡. Instituto Interuniversitario de Investigación de Reconocimiento Molecular y Desarrollo Tecnológico. Universitat Politècnica de València - Universitat de València. Camino de Vera s/n, 46022, Valencia, Spain.
†. CIBER de Bioingeniería, Biomateriales y Nanomedicina (CIBER-BBN).
∥. Departamento de Química, Universitat Politècnica de València, Camino de Vera s/n, 46022, València, Spain.
⊥. Chemistry Department, Stephenson Institute for Renewable Energy, The University of Liverpool, Chadwick Building, Peach Street, Liverpool, L69 7ZF (UK).

Chemicals

Tetraethylorthosilicate (TEOS), sodium hydroxide (NaOH), *n*-cetyltrimethylammonium bromide (CTAB), tris(hydroxymethyl)aminomethane (TRIS), (3-aminopropyl)triethoxysilane (APTES), *N*-(2-hydroxyethyl)piperazine-*N*'-(2-ethanesulfonic acid) (HEPES), rhodamine B, sodium arsenate dibasic heptahydrate ($Na_2HAsO_4\cdot 7H_2O$) and sodium (meta)arsenite ($NaAsO_2$) were purchased from Aldrich. Milli-Q water (resistivity 18.2 MΩ·cm at 25°C) was used in all experiments. The aptamer Ars-3 (5'- GGT AAT ACG ACT CAC TAT AGG GAG ATA

CCA GCT TAT TCA ATT TTA CAG AAC AAC CAA CGT CGC TCC GGG TAC TTC TTC ATC GAG ATA GTA AGT GCA ATC T-3') were provided by Isogen Life Science. Analytical-grade solvents were purchased from Scharlab (Barcelona, Spain). All chemicals were used as received.

General Techniques

Powder X-ray diffraction (PXRD), thermogravimetric analysis (TGA), elemental analysis (EA), Fourier transform infrared spectroscopy (FTIR), transmission electron microscopy (TEM), N_2 adsorption-desorption, dynamic light scattering (DLS) and ultraviolet-visible (UV-Vis) spectroscopy techniques were used to characterize the prepared materials. X-ray measurements were performed on a Bruker AXS D8 Advance diffractometer using Cu-Kα radiation. TGA analysis were carried out on a TGA/SDTA 851e Mettler Toledo equipment, using an oxidant atmosphere (Air, 80 mL/min) with a heating program consisting on in a heating ramp of 10 °C per minute from 273 to 373 K followed by an isothermal heating step at this temperature for 60 min in a nitrogen atmosphere (80 mL min^{-1}). Then, the program was allowed to continue with a dynamic heating segment from 373 to 1273 K in an oxidant atmosphere (air, 80 mL min^{-1}) and with an isothermal heating step at this temperature for 30 min. FTIR spectra were acquired with a Bruker tensor II Platinum ATR spectrometer. TEM images of MSNs were taken with a JEOL TEM-1010 Electron Microscope working at 100 kV. N_2 adsorption-desorption isotherms were recorded on a Micromeritics ASAP2010 automated sorption analyser. The samples were degassed at 120 °C in vacuum overnight. The specific surfaces areas were calculated from the adsorption data in the low pressures range using the BET model. Pore size was determined following the BJH method. UV-Vis spectroscopy was carried out with a Thermo scientific Evolution 201 UV-Vis spectrometer and fluorescence studies were carried out on a Jasco FP-8300 fluorescence spectrophotometer.

Materials synthesis

Synthesis of MCM-41 mesoporous nanoparticles: An aqueous solution of NaOH (2 M, 3.5 mL) was added to a solution of CTAB (1.00 g, 2.74 mmol) in deionized H_2O

(480 mL). Followed by adjusting the solution temperature to 80 °C, TEOS (5 mL, 2.57 x 10^{-2} mol) was added dropwise to the surfactant solution. The mixture was stirred for 2 h to yield a white precipitate. The final solid was centrifuged, washed with deionized water and dried at 70 °C for 18 h (MCM-41 as-synthesized). Finally, to obtain the final porous material (MCM-41) the as-synthesized solid was calcined at 550 °C under oxidizing atmosphere for 5 h in order to remove the template phase.

Synthesis of S1: To prepare the amino functionalized solid **S1**, calcined MCM-41 (610 mg) and rhodamine B (237 mg, 0.5 mmol) were soaked in acetonitrile (30 mL). The suspension was stirred at room temperature for 24 h to load the MCM-41 pores. Afterward an excess of APTES (571 µL, 2.77 mmol) was added, and the suspension was stirred at room temperature for 5.5 h. Finally, the resulting solid was isolated by filtration, washed with acetonitrile (3 mL) and dried at 37 °C for 18 h.

Optimization for the synthesis of S1-Ars-3: In order to estimate the proper amount of Ars-3 for the preparation of **S1-Ars-3**, capping experiments in presence of different amounts of Ars-3 were carried out. First of all, portions of a suspension of 1 mg **S1** mL^{-1} HEPES were added to a solution containing the aptamer Ars-3 in concentrations of 20, 40 and 60 µmol g **S1**$^{-1}$ in Milli-Q water, and each suspension was stirred for 30 min at 37 °C. An estimation of the content of Ars-3 retained in during the solid before and after the capping process was done by measuring the absorbance of Ars-3 at 260 nm and of rhodamine B at 555 nm and taking into account the molar extinction coefficients of rhodamine B and Ars-3 at these wavelengths. Following this procedure, an optimum amount of 0.04 mmol Ars-3 g **S1**$^{-1}$ was selected. Results obtained from these studies are summarized in Table S1.

Table S1. Content of Ars-3 added for the synthesis of **S1-Ars-3** and Ars-3 retained during the process.

Ars-3 added ($mmol\ g^{-1}$ S1)	**Ars-3 retained ($mmol\ g^{-1}$ S1)**	**% retained ($mmol\ g^{-1}$ S1)[a]**
0.02	0.002	10.81
0.04	0.013	32.13
0.06	0.004	6.36

[a] Ars-3 content in **S1-Ars-3** estimated by absorbance measurements of diluted Ars-3 solutions in HEPES buffer (pH 7.2) before and after the capping process (Rhodamine B $\varepsilon_{260nm} = 25400\ M^{-1}\ cm^{-1}$ and $\varepsilon_{555nm} = 94600\ M^{-1}$ Ars-3 $\varepsilon_{260nm} = 990900\ M^{-1}\ cm^{-1}$ and $\varepsilon_{555nm} = 1000\ M^{-1}\ cm^{-1}$).

Synthesis of S1-Ars-3: With the aim to obtain solid **S1-Ars-3**, 150 µL of a suspension of 1 mg **S1** mL^{-1} in HEPES buffer were suspended in 60 µL of a solution containing the aptamer Ars-3 in a concentration of 28.6 µM in Milli-Q water, and the suspension was stirred at 37 °C for 30 min. The final **S1-Ars-3** solid was isolated by centrifugation and washed with 300 µL of 50 mM HEPES buffer (pH 7.2) in order to remove the residual dye and the free aptamer.

Materials Characterization

The characterization of the MSNs-based materials (MCM-41, **S1** and **S1-Ars-3**) was carried out using standard techniques including: TEM, PXRD, N_2 adsorption-desorption analysis, DLS and FTIR. PXRD patterns of the nanoparticulated MCM-41 as-synthesized, calcined MCM-41 and S1 can be found in Figure 1A. The PXRD of MCM-41 as-synthesized (curve a in Figure 1A) showed four low-angle reflections, typical of a hexagonal ordered array that can be indexed as (100), (110), (200) and (210) Bragg peaks. The a_0 cell parameter was calculated to be 43 Å (d_{100} spacing = 37 Å). The condensation of silanol groups during the calcination step is clearly reflected in a significant shift of the (100) peak to higher 2θ values, corresponding to a cell contraction of 4.8 Å. The existence of the (100) reflection peak in the PXRD pattern of solids **S1** evidences that the loading and the functionalization processes did not alter the 3D mesoporous structure of the scaffold (curve c in Figure 1A). Analysis of TEM images of the materials also confirmed the preservation of the mesoporous structure as the typical channels of the MCM-41 network were visualized as alternate dark and light stripes (see Figure 1B). TEM images also show that MCM-41 support and solid S1 are spherical particles with diameters ranging from 100 to 150 nm.

N_2 adsorption-desorption measurements were carried out, as a complement to PXRD patterns and TEM analysis, in order to elucidate the porous structure of the prepared nanomaterials. The N_2 adsorption-desorption isotherms of the calcined MCM-41 material showed two sharp adsorption steps (curve b in Figure S1). The first step, at an intermediate P/P_0 value (0.1-0.3), is typical of this type of materials and attributed to nitrogen condensation inside the mesopores by capillarity. The absence of a hysteresis loop in this range and the tight BJH pore distribution (inset, Figure S1), suggested the presence of uniform cylindrical mesopores with pore volume of 0.74 cm^3 g^{-1} calculated by using the BJH model on the adsorption branch of the isotherm.[1] Moreover, the total specific surface was calculated to be 888.41 m^2 g^{-1} by the application of the BET model.[2] From the PXRD and porosimetry studies, a pore diameter of 2.59 nm and a wall thickness of 1.72 nm were estimated. On the other hand, N_2 adsorption-desorption isotherms of **S1** was typical of mesoporous systems with filled mesopores (see Figure S1 curve a). Consequently, a significant decrease in the adsorbed N_2 volume (0.14 cm^3 g^{-1}) and surface area (226.85 m^2 g^{-1}) was observed. Parameters calculated from N_2 adsorption-desorption isotherms of calcined MCM-41 and solid **S1** are listed in Table 1.

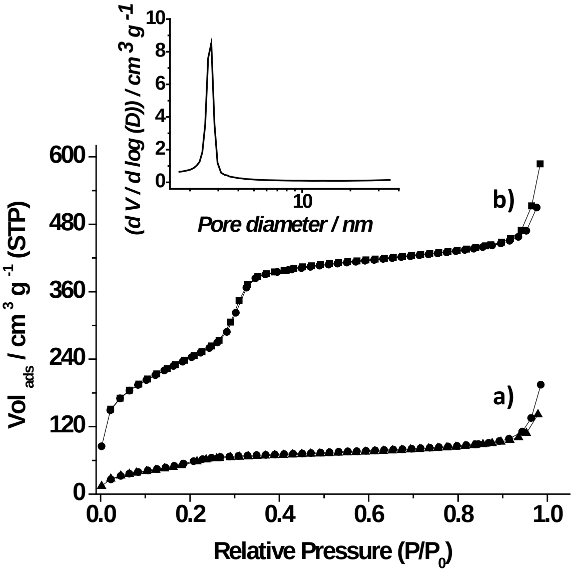

Figure S1. Nitrogen adsorption-desorption isotherms for (a) **S1** and (b) calcined MCM-41 materials. Inset: Pore size distribution of calcined MCM-41 mesoporous material.

DLS studies were conducted at 25 °C on previously sonicated suspensions of the nanomaterials in HEPES buffer at a concentration of 0.01 mg mL^{-1}. Results are listed in Table S2. As can be seen, the particle diameter increases after each surface modification. On the other hand, the efficiency of the different surface modifications was followed by Zeta potential measurements of the suspended materials (Table S2). Bare MCM-41 exhibited a negative Zeta potential value that changed to positive after functionalization with APTES (**S1**). Zeta potential changed again to negative upon interaction of **S1** with the aptamer Ars-3.

Table S2. Hydrodynamic diameter of MCM-41, **S1** and **S1-Ars-3** solids measured by DLS.

Solid	Hydrodynamic particle diameter (nm)	Zeta potential (mV)
MCM-41	123.5 ± 20.7	-38.53 ± 1.28
S1	165.1 ± 17.1	48.65 ± 0.92
S1-Ars-3	190.0 ± 26.3	-30.77 ± 2.75

The surface modifications of the prepared materials were also studied by means of FTIR spectroscopy. Figure S2 shows the FTIR spectra of solids **S1** and **S1-Ars-3** (curve a and b, respectively). The two spectra showed the characteristic IR absorption bands of siliceous materials: 456 cm^{-1} attributed to the vibration of Si-O bonds, a shoulder at 576 cm^{-1} ascribed to cyclic Si-O-Si structures, a band at 803 cm^{-1} attributed to SiO_4 tetrahedrons, a band at 946 cm^{-1} attributed to the Si-O-H stretching, and a band at 1080 cm^{-1} with a shoulder at 1200 cm^{-1} related to the bond stretching vibrations of Si-O-Si. The broad band at 3700–3000 cm^{-1} can be attributed to the O-H bonding vibration of adsorbed water and SiO-H groups, and the band at 1629 cm^{-1} is ascribed to the deformation vibration of the HO-H bond in water molecules. [3,4]

Moreover, the FTIR spectrum of nanomaterials **S1** and **S1-Ars-3** showed the antisymmetric vibrations of the CH_2 groups at 2947 cm^{-1} confirming the modification of the scaffold surface with APTES. The loading of the pores with rhodamine B and the further functionalization of the outer surface in solid **S1** was also confirmed by the appearance of the bands characteristic to the C-H bond in the range of 1400-1500 cm^{-1}. The presence of the aptamer Ars-3 in **S1-Ars-3** solid is evidenced by the appearance of the peak at 2854 cm^{-1} attributed to stretching vibration of CH_2 groups.[3] In addition, the interaction of the amine groups with Ars-3 aptamer is evidenced by the shift of the antisymmetric vibrations of the CH_2 groups at 2947 to 2927 cm^{-1} in **S1-Ars-3** spectrum.

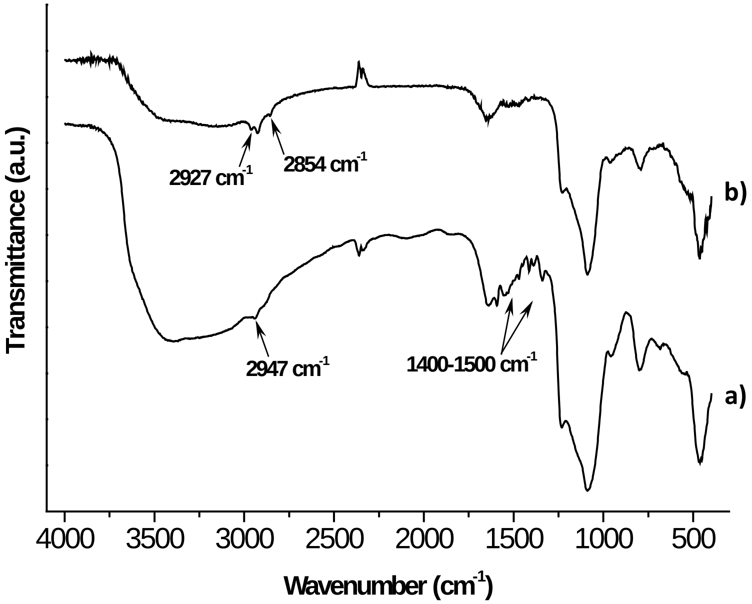

Figure S2. FTIR spectra of solids (a) **S1** and (b) **S1-Ars-3**.

Moreover, UV-Vis and fluorescence spectra change before and after the capping process of **S1** pores with Ars-3 were measured (see Figure S3). As could be seen, the fluorescence of suspensions of **S1** and **S1-Ars-3** showed the typical rhodamine B band centered at 572 nm. On the other hand, UV-Vis spectra of **S1** showed the typical rhodamine B absorption centered at 555 nm. Suspensions of **S1-Ars-3** also showed rhodamine B absorption and an intense band centered at 260 nm indicating the presence of Ars-3 aptamer in the solid.

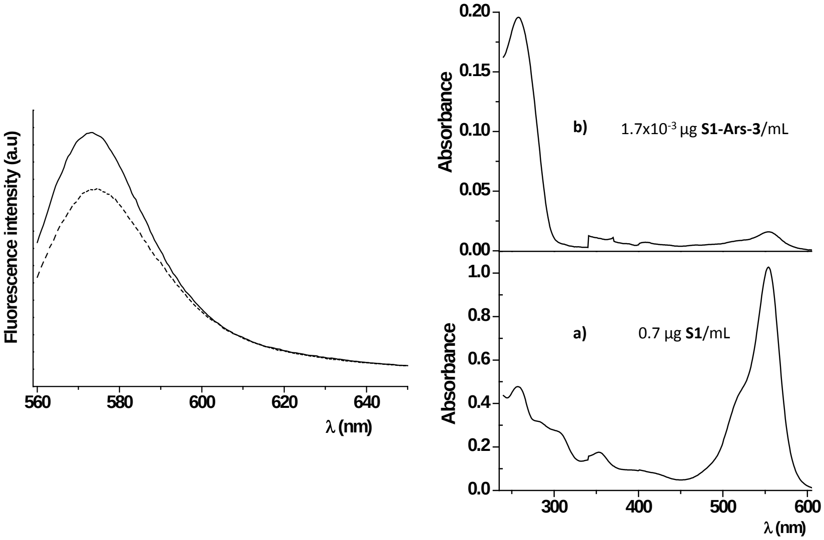

Figure S3. Left panel: rhodamine B emission bands (excitation at 555 nm) of aqueous suspensions of solid **S1** (straight line) and **S1-Ars-3** (dashed line). Right panel: (a) UV spectra of an aqueous suspension of **S1** and (b) of **S1-Ars-3**.

In addition, the degree of functionalization and loading efficacy were determined by elemental analysis and thermogravimetric studies. The thermogravimetric analysis of solid **S1** showed a typical behaviour in functionalized mesoporous materials; i.e. a first weight loss between 25 and 150 ^{o}C related to the solvent evolution, a second step, between 150 and 800 ^{o}C due to the combustion of the organics and a final loss in the 800 - 1000 ^{o}C range related to the condensation of the silanol groups (see Table S3).

Table S3. Results of thermogravimetric analysis of solid **S1**.

Solid	**Solvent** (%wt)	**Organics** (%wt)	**Silanols** (%wt)
S1	0.15	17.64	0.90

In addition, from elemental analysis of C, H and N it is possible to determine the amount of APTES and rhodamine B contained in the materials calculated in millimole per gram of **S1** (mmol g^{-1} **S1**) using equation 1:

$$\alpha_A = \frac{\Delta W_i\% \times 1000}{\Delta W_{SiO_2}\% \times nM_i}\left(\frac{mmol}{g\ \boldsymbol{S1}}\right) \qquad (1)$$

where $\Delta Wi\%$ (i = C, N, S) is the weight percentages of carbon, nitrogen or sulphur, Mi is the corresponding atomic weight and n is the number of the corresponding atom type in one molecule. $\Delta WSiO_2\%$ is the inorganic SiO_2 content in weight percentage. From elemental analysis of solid **S1** quantities of 10.07, 2.64 and 3.28% of C, H and N were found. In addition, the content of dye in solid **S1-Ars-3** was determined from the dye content in **S1** after interaction with Ars-3 aptamer, and determining the amount of dye delivered during the washing process. Moreover, the content of oligonucleotide in **S1-Ars-3** was calculated by measuring the absorbance of the aptamer Ars-3 at 260 nm after the capping process. Results are shown in table S4.

Table S4. Content of APTES, Rh B and Ars-3 in the prepared materials **S1** and **S1-Ars-3.**

Solid	$\alpha_{Rh\ B}$ (mmol g^{-1} SiO_2)	α_{APTES} (mmol g^{-1} SiO_2)	α_{Ars-3} (mmol g^{-1} SiO_2)
S1	0.076 ± 0.006	2.729 ± 0.004	-
S1-Ars-3	0.071 ± 0.005	2.729 ± 0.004	0.0016 ± 0.005

Additionally, taking into account the previously calculated quantities of APTES and aptamer Ars-3 we estimated that **S1-Ars-3** contains 9.52 x 10^{18} Ars-3 molecules g SiO_2^{-1}. Furthermore, considering the obtained values of the specific surface of **S1** (227 m^2 g^{-1}) and the aptamer content, it is possible to estimate that the average surface coverage on solid **S1-Ars-3** by Ars-3 aptamer molecules amount to 0.034 molecules nm^{-1}. This aptamer surface coverage value results in an average distance between neighboring aptamer molecules of *ca.* 54 nm. Likewise, the average surface coverage on solid **S1-Ars-3** by APTES molecules was estimated to be 5.9 molecules nm^{-1}. Lastly, using the aptamer and APTES contents previously calculates a ratio of 173 APTES molecules Ars-3^{-1} molecules was estimated.

Release experiments

Release experiments of S1-Ars-3: 150 µg of **S1-Ars-3** were suspended in 1.5 mL of HEPES (50 mM, pH 7.2) and the suspension was divided into two fractions. The first fraction was diluted with 150 µL of Milli-Q, whereas the second one was treated with 50 µL of an aqueous solution containing 2 x 10^4 ppb of As(III) and diluted with 100 µL of Milli-Q. In both cases, suspensions were stirred for 35 minutes at room temperature and at certain times, intervals fractions were taken and centrifuged to remove the solid. Dye delivery at a certain time was then measured by the fluorescence emission of rhodamine B, centered at 572 nm, in the solution (λ_{exc} = 555 nm).

Controlled release of material S1-Ars-3 in the presence of DNAse I enzyme: In a typical experiment, 150 µg of **S1-Ars-3** were suspended in 1.5 mL of HEPES (50 mM, pH 7.2) and the suspension was divided into two fractions. The first fraction was diluted with 150 µL of Milli-Q, whereas the second one was treated with 50 µL of an aqueous solution containing 55 U µL^{-1} of DNAse I and diluted with 100 µL of Milli-Q. In both cases, suspensions were stirred for 35 minutes at room temperature and at certain times, intervals fractions were taken and centrifuged to remove the solid. Dye delivery at a certain time was then measured by the fluorescence emission of rhodamine B, centered at 572 nm, in the solution (λ_{exc} = 555 nm).

Recognition features reported materials for As(III) sensing

A comparion of our sensing material with different As(III) reported sensors is shown in Table S5. From this table, it can be seen that both the limit of detection (LOD) and analysis time for probe **S1-Ars-3** are in the ranges of other materials-based systems reported for As(III) detection.

Table S5. Sensing features for reported materials for sensing As(III)

Material	Detection method	LOD (ppb)	Time (min)	Ref.
AuNPs	DLS	3.0×10^{-3}	10	5
	Colorimetric	0.6	35	
	Resonance scattering	0.8	35	6
	Colorimetric	5.3	35	7
	Colorimetric	2.0	420	8
	Resonance Rayleigh Scattering (RSS)	1.9	15	9
	Colorimetric	1.3	20	10
	SERS	0.1	15	11
Au@Ag NPs	SERS	5.9×10^{-2}	65	12
	SERS	0.1	30	13
Au /Fe_3O_4 NPs	Electrochemical	1.0	13	14
AgNPs	Colorimetric	6.0	Not reported	15
CdTe QDs	Fluorimetric	2.6	10	16
	Fluorimetric	1.7	Not reported	17
CdTe/ZnS QDs	Fluorimetric	10^{-7}	10	18
Ag doped hollow CdS/ZnS bi-layer NPs	Fluorimetric	0.2	Not reported	19
Fe_3O_4 microspheres	Electrochemical	8.0×10^{-4}	2	20
CNTs	Electrochemical	0.5	120	21
S1-Ars-3	Fluorimetric	0.9	35	This work

References

1. Barrett, E. P.; Joyner, L. G.; Halenda, P. P. The Determination of Pore Volume and Area Distributions in Porous Substances. I. Computations from Nitrogen Isotherms. *J. Am. Chem. Soc.* **1951**, *73* (1), 373–380.
2. Brunauer, S.; Emmett, P. H.; Teller, E. Adsorption of Gases in Multimolecular Layers. *J. Am. Chem. Soc.* **1938**, *60* (2), 309–319.
3. Stefanescu, M.; Stoia, M.; Stefanescu, O. Thermal and FT-IR Study of the Hybrid Ethylene-Glycol-Silica Matrix. *J. Sol-Gel Sci. Technol.* **2007**, *41* (1), 71–78.
4. Villalonga, R.; Díez, P.; Sánchez, A.; Aznar, E.; Martínez-Máñez, R.; Pingarrón, J. M. Enzyme-Controlled Sensing-Actuating Nanomachine Based on Janus Au-Mesoporous Silica Nanoparticles. *Chem. Eur. J.* **2013**, *19* (24), 7889–7894.
5. Kalluri, J. R.; Arbneshi, T.; Khan, S. A.; Neely, A.; Candice, P.; Varisli, B.; Washington, M.; McAfee, S.; Robinson, B.; Banerjee, S.; Singh, A. K.; Senapati, D.; Ray, P. C. Use of Gold Nanoparticles in a Simple Colorimetric and Ultrasensitive Dynamic Light Scattering Assay: Selective Detection of Arsenic in Groundwater. *Angew. Chem. Int. Ed.* **2009**, *48* (51), 9668–9671.
6. Wu, Y.; Liu, L.; Zhan, S.; Wang, F.; Zhou, P. Ultrasensitive Aptamer Biosensor for Arsenic(III) Detection in Aqueous Solution Based on Surfactant-Induced Aggregation of Gold Nanoparticles. *Analyst* **2012**, *137* (18), 4171–4178.
7. Wu, Y.; Zhan, S.; Wang, F.; He, L.; Zhi, W.; Zhou, P. Cationic Polymers and Aptamers Mediated Aggregation of Gold Nanoparticles for the Colorimetric Detection of Arsenic(III) in Aqueous Solution. *Chem. Commun.* **2012**, *48* (37), 4459–4461.
8. Liang, R.-P.; Wang, Z.-X.; Zhang, L.; Qiu, J.-D. Label-Free Colorimetric Detection of Arsenite Utilizing G-/T-Rich Oligonucleotides and Unmodified Au Nanoparticles. *Chem. Eur. J.* **2013**, *19* (16), 5029–5033.
9. Tang, M.; Wen, G.; Liang, A.; Jiang, Z. A Simple and Sensitive Resonance Rayleigh Scattering Method for Determination of As(III) Using Aptamer-Modified Nanogold as a Probe. *Luminescence* **2014**, *29*, 603–608.
10. Zhan, S.; Yu, M.; Lv, J.; Wang, L.; Zhou, P. Colorimetric Detection of Trace Arsenic(III) in Aqueous Solution Using Arsenic Aptamer and Gold Nanoparticles. *Aust. J. Chem.* **2014**, *67* (5), 813–818.
11. Ye, L. L.; Wen, G. Q.; Dong, J. C.; Luo, Y. H.; Liu, Q. Y.; Liang, A. H.; Jiang, Z. L. A Simple Label-Free Rhodamine 6G SERS Probe for Quantitative Analysis of Trace As3+ in an Aptamer-Nanosol. *Rsc Adv.* **2014**, *4* (62), 32960–32964.

12. Yang, B.; Chen, X.; Liu, R.; Liu, B.; Jiang, C. Target Induced Aggregation of Modified Au@Ag Nanoparticles for Surface Enhanced Raman Scattering and Its Ultrasensitive Detection of Arsenic(III) in Aqueous Solution. *RSC Adv.* **2015**, *5* (95), 77755–77759.
13. Song, L.; Mao, K.; Zhou, X.; Hu, J. A Novel Biosensor Based on Au@Ag Core-Shell Nanoparticles for SERS Detection of Arsenic(III). *Talanta* **2016**, *146*, 285–290.
14. Cui, H.; Yang, W.; Li, X.; Zhao, H.; Yuan, Z. An Electrochemical Sensor Based on a Magnetic Fe3O4 Nanoparticles and Gold Nanoparticles Modified Electrode for Sensitive Determination of Trace Amounts of Arsenic(III). *Anal. Methods* **2012**, *4* (12), 4176-4181.
15. Divsar, F.; Habibzadeh, K.; Shariati, S.; Shahriarinour, M. Aptamer Conjugated Silver Nanoparticles for the Colorimetric Detection of Arsenic Ions Using Response Surface Methodology. *Anal. Methods* **2015**, *7* (11), 4568–4576.
16. Wang, X.; Lv, Y.; Hou, X. A Potential Visual Fluorescence Probe for Ultratrace Arsenic(III) Detection by Using Glutathione-Capped CdTe Quantum Dots. *Talanta* **2011**, *84* (2), 382–386.
17. Zhou, Y.; Huang, X.; Liu, C.; Zhang, R.; Gu, X.; Guan, G.; Jiang, C.; Zhang, L.; Du, S.; Liu, B.; Han, M. Y.; Zhang, Z. Color-Multiplexing-Based Fluorescent Test Paper: Dosage-Sensitive Visualization of Arsenic(III) with Discernable Scale as Low as 5 ppb. *Anal. Chem.* **2016**, *88* (12), 6105–6109.

4. Surface Enhanced Raman Scattering and Gated Materials for Sensing Applications. The Ultrasensitive Detection of *Mycoplasma* and Cocaine

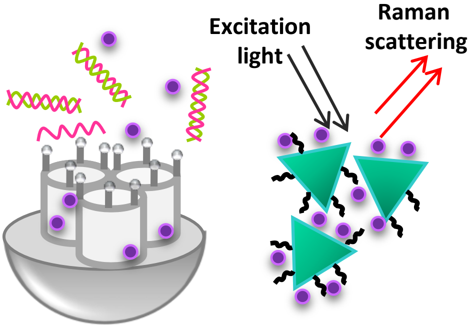

Surface Enhanced Raman Scattering and Gated Materials for Sensing Applications. The Ultrasensitive Detection of Mycoplasma and Cocaine.

Mar Oroval[+],[a,e] Marc Coronado-Puchau[+],[c] Judith Langer,[c] Marta Norah Sanz-Ortiz,[c] Ángela Ribes,[a,e] Elena Aznar,[a,e] Carmen Coll,[a] María Dolores Marcos,[a,b,e] Félix Sancenón,[a,b,e] Luis M. Liz-Marzán[c,d,e] and Ramón Martínez-Máñez*[a,b,e]*

[a] Instituto Interuniversitario de Investigación de Reconocimiento Molecular y Desarrollo Tecnológico. Unidad Mixta Universitat Politècnica de València - Universitat de València. Camino de Vera s/n, 46022, Valencia, Spain.
[b] Departamento de Química, Universidad Politécnica de Valencia.
[c] Bionanoplasmonics Laboratory, CIC biomaGUNE, Paseo de Miramón 182, 20009 Donostia - San Sebastián, Spain.
[d] Ikerbasque, Basque Foundation for Science, 48013 Bilbao, Spain.
[e] CIBER de Bioingeniería, Biomateriales y Nanomedicina (CIBER-BBN), Spain.
[+]These authors contributed equally to this work.

Received 23th May 2016
First published on the web 9th August 2016

Chem. Eur. J., ***2016****, 22, 13488 – 13495*
Reproduced with permission of Wiley-VCH VerlagGmbH&Co. KGaA.

Chem. Eur. J., 2016, 22, 13488 – 13495

Abstract

We present herein a novel combination of gated mesoporous silica nanoparticles (MSNs) and surface-enhanced Raman scattering (SERS) for sensing applications. As a proof-of-concept, we show the design of a system comprising MSNs loaded with crystal violet (CV), a molecule with high Raman cross section acting as SERS reporter, and capped with either a suitable DNA sequence for the detection of *Mycoplasma* genomic DNA or with an aptamer that selectively coordinates cocaine. In both cases the presence of the corresponding target analyte in solution (i.e., genomic DNA or cocaine) resulted in the release of CV. CV delivery was detected by SERS upon adsorption on gold nanotriangles (AuNTs), which display an efficient electromagnetic field enhancement and a high colloidal stability. By using this novel procedure a limit of detection of at least 30 copies DNA per µL was determined for the detection of *Mycoplasma* genomic DNA, whereas cocaine was detected at concentrations as low as 10 nM.

Introduction

Recent advances in nanotechnology and molecular and biomolecular chemistry have resulted in significant advances in areas such as bioengineering, biosensing, and bionanotechnology.[1–3] In this scenario materials obtained by anchoring organic molecules to pre-designed inorganic scaffolds resulted in the design of hybrid systems with a wide variety of new functionalities.[4,5] An interesting application in this field is the development of gated nanodevices that can deliver an entrapped cargo when selected external stimuli are applied. These gated materials consist of a suitable inorganic support that acts as a nanocontainer and a switchable "gate-like" ensemble capable of being "opened" or "closed" at-will.[6,7] Mesoporous silica nanoparticles (MSNs) are suitable inorganic scaffolds in gated ensembles because they contain tailor-made homogeneous pores of approximately 2–10 nm in diameter, are highly inert, easy to functionalize through known chemistries, and have a remarkable load capacity dictated by large specific surface areas and specific volumes.[8,9] MSNs have been functionalized with a wide variety of switchable molecular, supramolecular and biomolecular pore-capping systems to develop gated materials capable of showing "zero release". These capped materials have been used mainly in drug-delivery applications.[10–12] In contrast, their use in sensing protocols is still uncommon and relatively few examples are available.[13,14] For the development of sensory nanoprobes based on MSNs, the inorganic scaffold is loaded with a suitable reporter and the capping mechanism is designed in a way that only the target analyte is able to induce pore opening and delivery of the reporter (usually a fluorophore).[13,15–17]

On the other hand, surface enhanced Raman scattering (SERS) is a highly sensitive, vibrational spectroscopic technique that allows the detection of molecules at very low concentrations, additionally providing structural information.[18–22] The efficiency of SERS is dependent on two effects: 1) the electromagnetic field enhancement provided by excitation of localized surface plasmon resonances (LSPRs) and 2) the chemical enhancement provided by the electronic interaction between adsorbed molecules and the surface. Gold nanoparticles (AuNPs) in particular have been extensively used because of their high chemical stability and the possibility to tailor their LSPRs over the visible and near infrared (NIR) wavelength ranges,[23] which are most appropriate for Raman scattering measurements.[24–26] As a consequence, AuNPs have been used for SERS detection of many different biological targets including simple biomolecules, proteins, and living cells.[27–38]

In this scenario, we envisioned SERS as a complementary detection technique, in combination with capped MSNs, as a suitable approach for the design of novel sensing applications. In previous reports on capped materials for sensing, the recognition event was typically monitored by changes in the fluorescence or color induced by the selective delivery of a dye from the mesoporous support.[13,39] By using a different approach, we were interested in taking advantage of the high performance that SERS offers for the development of sensing platforms, definitely rivaling with other optical measurements such as fluorescence.[40,41] Based on these concepts, a convenient design of a SERS-based capped system can be envisioned, so that selective uncapping of the MSNs in the presence of the target analyte leads to release of a highly Raman-active molecule (acting as Raman reporter) that is readily detected by using suitable dispersed plasmonic nanoparticles (here acting as a SERS sensor). When the Raman reporters are stored in the MSN carriers, they are too far away from the metal nanoparticle surface and the SERS effect does not occur, but when they are released upon analyte-triggered uncapping, SERS signals arise. We propose that this simple design could contribute to the development of highly specific and ultra-sensitive nanodevices for a quick identification of a wide variety of target molecules and biomolecules. To demonstrate the general proof-of-concept of this approach, we present here two different detection systems. Both of them comprise MSN carriers loaded with crystal violet (CV), as efficient Raman reporter with an excitation energy of $\lambda = 633$ nm, and capped with an oligonucleotide, which was specifically devised for the detection of either *Mycoplasma fermentans* genomic DNA or cocaine. In both cases, the addition of the corresponding target analyte (i.e., genomic DNA or cocaine) induces the displacement of the oligonucleotide from the MSNs (due to preferential oligonucleotide coordination with the analytes) and CV release, which is detected by SERS in the presence of gold nanotriangles (AuNTs). A representation of the sensing paradigm is illustrated in Scheme 1.

Results and discussion

Design of the detection protocol and sensing material

Mesoporous MCM-41 nanoparticles were synthesized in alkaline media following known procedures that make use of the cationic surfactant *n*-cetyltrimethylammonium bromide (CTABr) as directing agent for the condensation of the inorganic precursor tetraethylorthosilicate (TEOS).[42] The obtained powder was washed and the surfactant was subsequently removed by calcination. Then, the obtained MSNs were loaded with a dye (i.e., CV), followed by grafting of (3-aminopropyl)triethoxysilane (APTES) on the external surface (**S1**). Aminopropyl moieties are partially charged at neutral pH and display electrostatic interactions with negatively charged oligonucleotides. Addition of the oligonucleotide **O1** (see Table 3), a sequence highly conserved in the *Mycoplasma* genome that corresponds to a fragment of the 16S ribosomal RNA subunit,[43,44] resulted in capping of the pores (solid **S1**–**O1**). Hybridization of the capping oligonucleotide with *Mycoplasma* genomic DNA is expected to induce pore opening of the MSNs[45,46] and dye release, which would be then adsorbed on the Au nanoparticles, thereby facilitating detection by SERS spectroscopy. As cargo for the mesoporous carrier CV was chosen, which is an efficient Raman scatterer when illuminated at λ = 633 nm because of 1) the matching of molecular resonance and excitation wavelength and 2) quenching of the fluorescence background contribution due to the open, non-radiative relaxation channels.

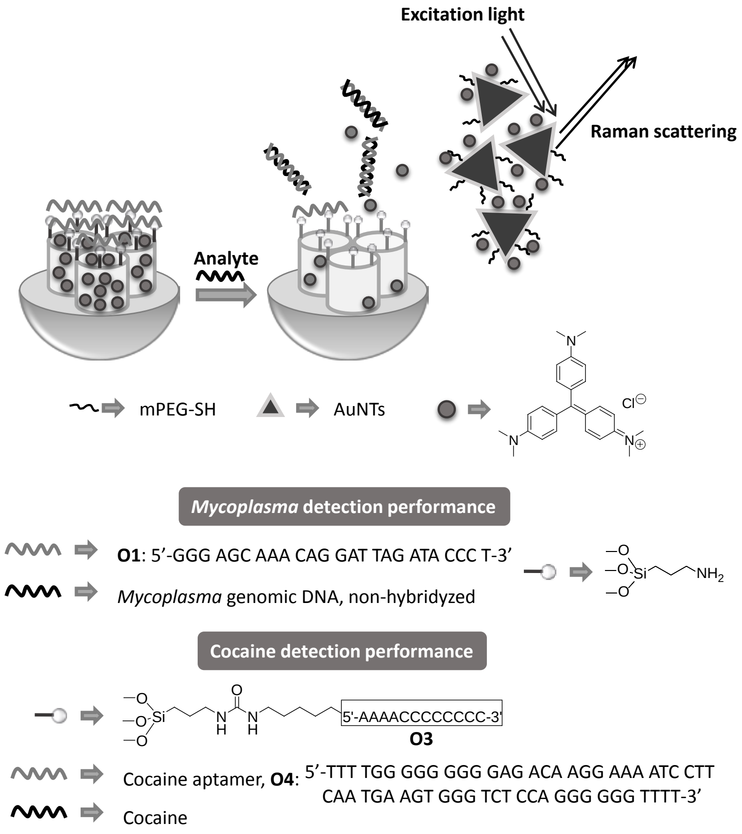

Scheme 1. Representation of the sensing paradigm for Mycoplasma genomic DNA and cocaine detection by means of capped MSNs and SERS. mPEG-SH=thiolated polyethyleneglycol ligand.

The approach followed for cocaine detection was identical, except that the CV-loaded MCM-41 support was functionalized on the external surface with (3-isocyanatopropyl)triethoxysilane (**S2**) and then, a short DNA sequence functionalized with an aminohexyl moiety at the 5′-end position, that is, oligonucleotide **O3** (see Table 3), was covalently attached through formation of urea bonds (solid **S2**–**O3**). Finally, addition of the sequence **O4** (which binds specifically to cocaine with high affinity, K_d = 0.4-10 µM[47]) blocked the pore outlets by hybridization with the immobilized oligonucleotide **O3**. This resulted in the final solid **S2**–**O4**. The presence of cocaine in solution was expected to displace the aptamer from the MSN surface, due to the selective aptamer–drug interaction, with subsequent pore opening and dye release. Again, the signaling event is recorded through the SERS signal of CV.

An additional task toward the design of the detection system was the optimization of the plasmonic SERS sensor. The SERS efficiency is highly dependent on the morphology of the nanoparticles, as it governs the resulting surface plasmon resonance properties. Among the different available shapes, spherical gold nanoparticles are easy to prepare and to functionalize but anisotropic gold nanoparticles have been shown to display more efficient SERS activity due to larger electromagnetic field enhancement at sharp edges or corners compared to those in smooth gold spheres.[48,49] In order to overlap the plasmon band with the laser excitation wavelength, we prepared gold nanotriangles (AuNTs) as a promising candidate for Raman signal amplification. Figure 1 shows the morphology and morphology-dependent LSPR band position for AuNTs (λ_{max} = 630 nm) and 13 nm Au nanospheres (λ_{max} = 520 nm). Moreover, the corresponding SERS performance of these two nanoparticle morphologies was tested in solutions containing CV at a concentration of 1μM (Figure 1D). This experiment confirmed that SERS of even the highly Raman-active CV, was below the detection threshold when using Au nanospheres, due to the moderate electromagnetic field enhancement,[50] but SERS signals were clearly observed when anisotropic AuNTs were used. Thus, AuNTs were selected and applied in the subsequent experiments. An additional challenge, however, was the stabilization of (relatively large) AuNTs in a medium with high ionic strength (20 mm tris(hydroxymethyl)aminomethane (Tris)/37.5 mM $MgCl_2$), which was required to facilitate DNA hybridization. We therefore investigated the stabilization of the nanoparticles functionalized with a thiolated polyethyleneglycol ligand (mPEG-SH). In particular, the AuNTs were functionalized with approximately ten mPEG-SH molecules per nanoparticle (AuNT@PEG), which was found to be enough to preserve the stability of the nanoparticles without affecting the adsorption of CV. As shown in Figure S4 in the Supporting Information, quenching of the fluorescence of CV was observed in the presence of AuNT@PEG indicating that the dye was indeed located in the proximity of the nanoparticles.

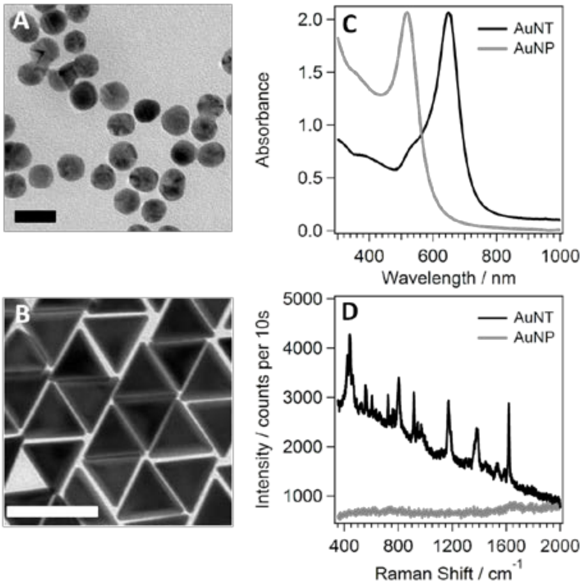

Figure 1. A) TEM image of (13±1) nm AuNPs. Scale bar=20 nm. **B)** TEM image of (66±3)×25 nm^2 AuNTs. Scale bar=100 nm. **C)** UV/Vis/NIR spectra of gold nanoparticle colloids, that is, gold nanospheres (AuNPs, gray curve) and gold nanotriangles (AuNTs, black curve). **D)** SERS performance of isotropic versus anisotropic gold nanoparticles. The SERS signal of a 1 µM solutions of CV containing AuNT@PEG (black line) and 13 nm AuNP@PEG (gray line). Both spectra were not background corrected. Measurement parameters: laser power=1.2 mW, integration time=10 s (extended scan).

Prior to applying the detection procedure to relevant biomolecules by CV release, we verified the expected linear relationship between the dye concentration and the SERS intensity by using pure aqueous solutions of CV within a concentration range of 5.00 – 0.05 µM with AuNTs at a concentration of 0.04 mM Au^0, corresponding to [AuNT] = 2.4 × 10^{-10} M (Figure S1 A in the Supporting Information). All characteristic vibrations at $\bar{\upsilon}$ = 1619, 914, 1382, 1171, and 800 cm^{-1} corresponding to two C−C ring stretch vibrations, a C center−C stretch vibration, and the C−H ring deformation in-plane and out-of-plane modes, respectively, were detected.[51] The intensity of the most prominent vibration at $\bar{\upsilon}$= 1619 cm^{-1} was found to follow a linear response within the concentration ranges of 5.0 to 0.4 µM and 0.4 to 0.05 µM (Figure S1B in the Supporting Information).

Characterization of the gated mesoporous silica nanoparticles

The MSN-based materials were characterized by using standard techniques. Powder X-ray diffraction of MCM-41 as-synthesized (curve A in Figure 2) showed four low-angle reflections, typical of a hexagonal mesoporous array that can be indexed as (100), (110), (200), and (210) Bragg peaks. Moreover, the presence and high intensity values of the (100) reflections in calcined MCM-41 and in the solids **S1** and **S2** (curves B–D in Figure 2) evidenced that the loading with CV and further functionalization processes of the external surface did not modify the 3D mesoporous structure. Furthermore, analysis of TEM images of all the materials confirmed the presence of the mesoporous structure and the typical channels of the MCM-41 network were visualized as alternate dark and light stripes (see Figure 2). The TEM images also showed that the MCM-41 support and the solids **S1** and **S2** consist of spherical particles of approximately 100 nm in diameter.

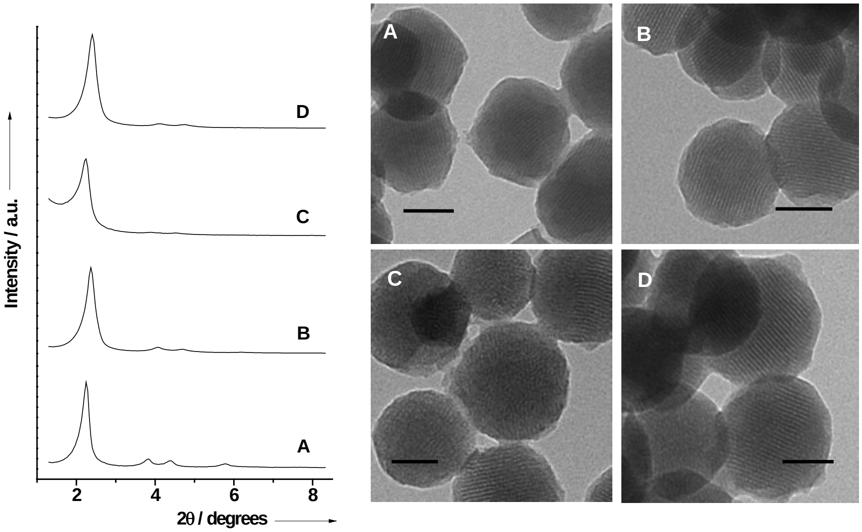

Figure 2. Left: Powder X-ray patterns of the solids **A)** MCM-41 as synthesized, **B)** calcined MCM-41, **C) S1** containing CV and functionalized with APTES, and **D) S2** containing CV and functionalized with (3-isocyanatopropyl)triethoxysilane. **Right:** TEM images of the solids **A)** MCM-41 as prepared, **B)** a calcined MCM-41 sample, **C) S1**, and **D) S2**, showing the typical hexagonal porosity of the MCM-41 mesoporous matrix. Scale bars=50 nm.

In order to complete the characterization of the MSNs, N_2 adsorption–desorption measurements were carried out. For all materials, the pore volume was calculated by applying the Barrett–Joyner–Halenda (BJH) model[52] on the adsorption branch of the isotherm (Figure S2 in the Supporting Information) and the total specific surface was calculated by using the Brunauer–Emmett–Teller (BET) model[53] (values are listed in Table 1). On the other hand, the N_2 adsorption–desorption isotherms of the solids **S1** and **S2** were typical of mesoporous systems with partially filled mesopores (see Figure S2 in the Supporting Information), and a significant decrease in the adsorbed N_2 volume and surface area was observed (see Table 1) as a consequence of pore loading (with CV) and external functionalization. The hydrodynamic diameters determined by dynamic light scattering (DLS) and the Zeta potential values for the solids MCM-41, **S1**, **S1–O1**, **S2**, **S2–O3**, and **S2–O4** were determined and are listed in Table S1 in the Supporting Information (see also Figures S3 and S4 in the Supporting Information).

Table 1. BET specific surfaces, pore volumes, and pore sizes calculated from the N_2 adsorption–desorption isotherms for selected materials.

Sample	S_{BET} (m^2 g^{-1})	Pore volume (cm^{-3} g^{-1})	Pore diameter (nm)
MCM-41	1055.5	0.86	2.62
S1	98.5	0.19	-
S2	637.9	0.42	-

On the other hand, the organic content in the functionalized nanoparticles was determined by elemental and thermogravimetric analyses (see Table 2). In addition, the content of oligonucleotide in **S1–O1**, **S2–O3**, and **S2–O4** was calculated by measuring the absorbance of the oligonucleotides **O1**, **O3**, and **O4** at λ = 260 nm after the capping process. Contents of 0.168, 0.017, and 0.085 mmol g^{-1} of solids, were determined for **O1**, **O3**, and **O4**, respectively.

Table 2. Content of APTES, (3-isocyanatopropyl)triethoxysilane and CV in solids **S1** and **S2**.

Solid	**α_{CV} (mmol g^{-1}SiO$_2$)**	**α_{CV} (mmol g^{-1}SiO$_2$)**	**α_{CV} (mmol g^{-1}SiO$_2$)**
S1	0.57	2.87	-
S2	0.53	-	0.31

Mycoplasma detection

Mycoplasma refers to a genome of prokaryotic microorganisms that have been described as parasites of various animals and plants.[54] In addition, their characteristic lack of a cell wall confers them resistance to many common antibiotics so they are often present in research laboratories as cell-culture contaminants. Hence, detection of these microorganisms is of general interest in biomedical and life sciences. For these experiments, **S1**–**O1** in the presence of AuNT@PEG was used. As stated above, a sequence highly conserved in the *Mycoplasma* genome, which corresponds to a fragment of the 16S ribosomal RNA subunit (i.e., **O1**), acted as cap for the MSNs.[43,44] In a first batch of experiments the functionality of the system was analyzed by adding **O2** (an **O1** complementary DNA strand) to a suspension of **S1**–**O1** (see the Experimental Section). Three non-complementary oligonucleotides (i.e., **O5**, **O6**, and **O7**) were also tested and used as specificity controls. In all cases CV release was monitored by both fluorescence and SERS (Figures S6 and S7 in the Supporting Information) and the system was then optimized for SERS detection. These studies showed that the **S1**–**O1**–AuNT@PEG system allowed us to selectively detect extremely low concentrations of **O2** at the nanomolar range (Figure S7 in the Supporting Information), whereas no SERS signal was obtained in the presence of the non-complementary oligonucleotides **O5**, **O6**, and **O7** (Figure S8 in the Supporting Information).

After confirming the selective gate opening with the complementary oligonucleotide, the response of **S1**–**O1** in the presence of *Mycoplasma fermentans* genomic DNA was studied to explore the correlation between the concentration of the genomic DNA within the range of 200 – 20 copies per µL and the amount of released CV. To the supernatant of each sample we added a solution containing AuNT@PEG reaching a final concentration of 0.04 mM Au^0 ([AuNTs] = 2.4×10^{-10} M) and measured the concentration-dependent SERS spectra (Figure 3). The recorded scattered frequencies are in good agreement ($\Delta < \pm 3$ cm^{-1}) with previously reported SERS spectra for CV.[55] From these studies it was observed that, in the absence of the *Mycoplasma* genomic DNA, the solid **S1–O1** was tightly capped and showed a very low release of the dye (which we defined as reference). In contrast, the presence of the target DNA induced uncapping of the pores and CV release. Regarding the sensitivity of this new approach, after subtraction of the reference signal, the SERS signal of CV was clearly detectable at concentrations as low as 30 DNA copies per µL of *Mycoplasma fermentans*. The detection of 20 copies per µL might be possible (see low signal at $\bar{\upsilon}$ = 1617 cm^{-1}) but under the current conditions the signal-to-noise ratio was too low to be correctly determined. Apart from that, the 30 DNA copies per µL limit represents an improvement when compared with previous works, using gated materials.[56,57] The concentration-dependent SERS intensity was plotted as function of the number of DNA copies (Figure 3B) and could be linearly fitted.

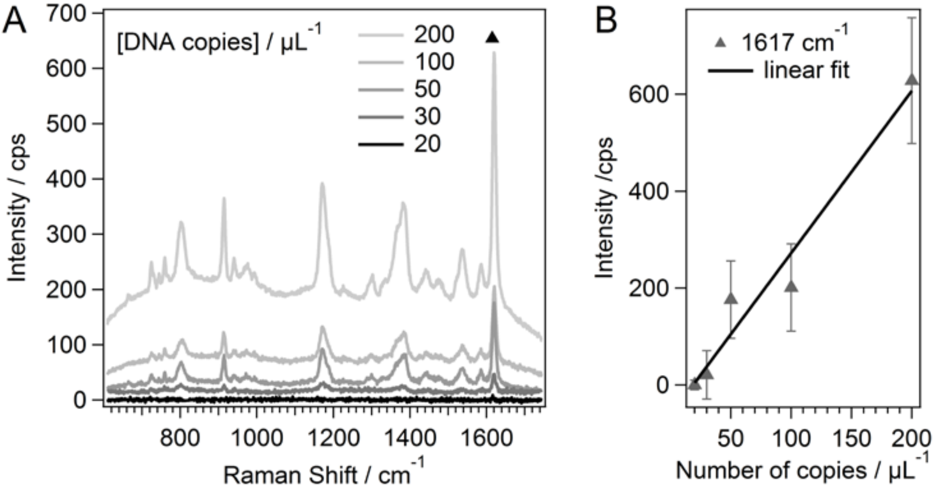

Figure 3. A) Detection of CV release as a function of the number of *Mycobacterium fermentans* genomic DNA copies per µL. The SERS signal of CV is detectable for concentrations as low as 30 DNA copies per µL. The SERS spectra were obtained by subtraction of the analyte spectra and the corresponding reference spectrum (without analyte) and an offset was applied for [DNA] = 30 µL^{-1} for clearer data presentation. **B)** Plot of the intensity of the peak at inline image =1617 cm^{-1} (black triangle in A) as a function of the DNA concentration and linearly fitted (black line) according to the function: y=(3.4±0.4) x−(62±42). The signal intensities were determined after applying a baseline correction. Error bars were calculated from two independent experiments.

Similar experiments with the solid **S1−O1** were carried out to verify the selectivity of the method, in which the genomic DNA of the pathogens *Legionella pneumophilia* and *Candida albicans* were used with a concentration of 100 copies per µL (Figure 4). SERS analysis demonstrated that the solid **S1−O1** responds preferably to the presence of *Mycoplasma fermentans* genomic DNA, as an approximately 64 % lower CV signal was detected in the supernatant in the presence of DNA from other pathogens.

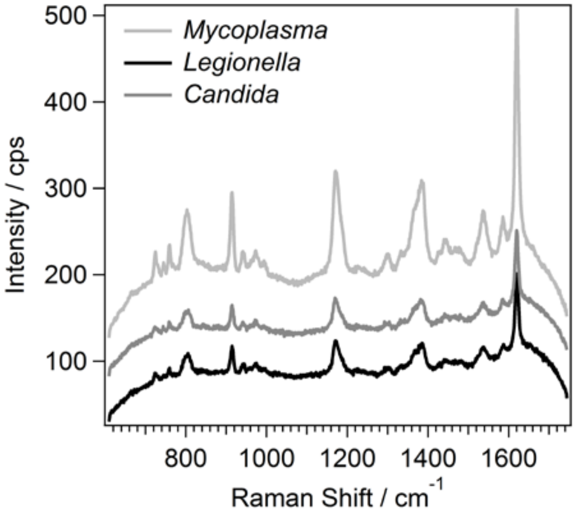

Figure 4. SERS detection of CV release in the presence of different types of genomic DNA, namely, *Mycoplasma fermentans* (light gray curve), *Legionella pneumophilia* (black curve), and *Candida albicans* (dark gray curve). The concentration of the genomic DNA was set at 100 copies per µL. Spectra were not corrected and an offset was applied for clearer data representation.

Cocaine detection

Encouraged by the results obtained for the solid **S1–O1**, we devised a second biosensor, again by using capped MSNs and SERS, aimed at cocaine detection. Cocaine is an alkaloid obtained from the leaves of the coca plant, which is extensively used in developed countries as an illegal recreational drug. Although cocaine production and distribution are restricted and illegal in most contexts, it is a powerful nervous system stimulant that causes strong addiction among consumers, frequently leading to serious health as well as social and legal problems. Therefore, the development of selective and sensitive devices for its detection is of high importance.[58–60] Our cocaine-sensing system comprised MSNs loaded with CV, functionalized with the short DNA sequence **O3** and finally capped with the cocaine aptamer **O4**, resulting in the final material **S2–O4**.

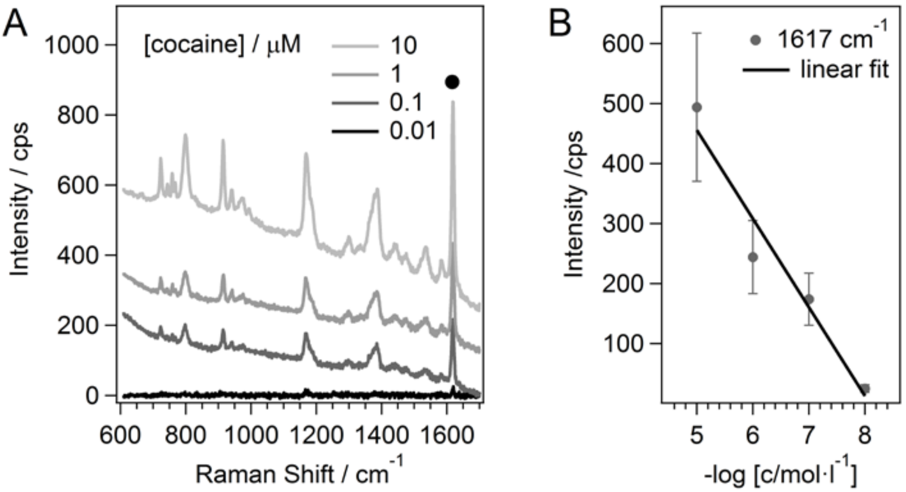

Figure 5. A) Detection of CV release as a function of the cocaine concentration. The most intense characteristic SERS peak of CV at inline image =1617 cm−1 (black dot) was clearly detected at a concentration as low as 10 nM. The SERS spectra were obtained by subtraction of the analyte spectra and the corresponding reference spectra (without analyte) and an offset was applied for clearer data representation. **B)** Plot of the most intense SERS peak (gray dots) at inline image =1617 cm−1 as a function of the cocaine concentration and linearly fitted (black line) according to the function: $y=-(147\pm24)\,x+(1194\pm160)$. Error bars were calculated from two independent experiments.

Subsequently, we studied the response of the prepared sensing nanocarrier **S2–O4** toward the presence of cocaine solutions in the concentration range of 10 µM to 10 nM. CV release was detected by addition of a solution containing AuNT@PEG to the supernatant to reach a final Au^0 concentration of 0.02 mM ([AuNTs] = 1.2×10^{-10} M), which was then monitored by SERS as a function of the cocaine concentration (Figure 5 A). The results clearly demonstrated that the interaction of cocaine with the aptamer triggers pore opening, allowing dye delivery and detection by SERS.

Upon optimization of the system, the most intense vibrations at $\bar{\upsilon}$ = 1617 and 1172 cm^{-1} of CV were detected by SERS at a cocaine concentration as low as 10 nM, indicating a high sensitivity as this result is comparable to those for other aptameric sensors based on fluorescence,[47,60] colorimetric[61,62] or electrochemical measurements.[63,64] Our results additionally provide an improvement of approximately 20-fold in the detection limit as compared to previous SERS-based aptameric cocaine sensors,[60] which confirms that this method is suitable for the ultrasensitive and highly selective detection of cocaine. The concentration-dependent SERS intensity was also plotted as function of the negative logarithmic cocaine concentration showing a linear response (Figure 5B). Furthermore, control experiments were also carried out to determine the specificity of the system. Experiments in the absence of drug (reference) and in the presence of other drugs, such as morphine, methadone and heroine, showed that **S2-O4** was highly selective to the presence of cocaine in the selected concentration range (Figure 6), because no cargo release was detected in the presence of other drugs.

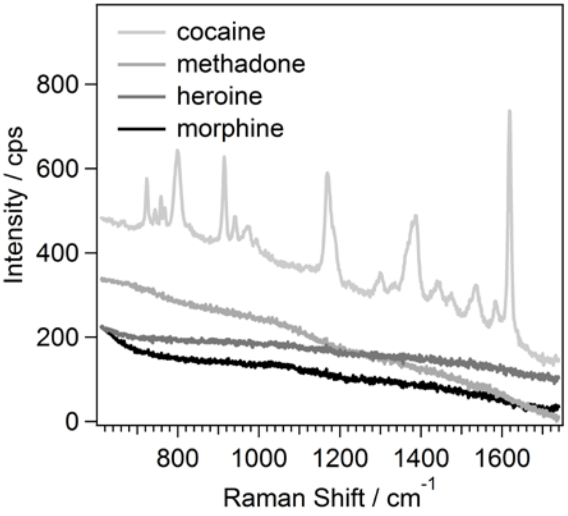

Figure 6. Detection of CV release in the presence of different drugs. The drug concentration was 10 µM in all cases. The SERS spectra were obtained by subtraction of the drug spectra and the corresponding reference spectra (i.e., in absence of the drug) and an offset was applied for clearer data representation.

Conclusions

We demonstrated for the first time that the combination of gated materials with SERS spectroscopy can be used for the design of highly sensitive and selective sensing systems. As a proof-of-concept, CV-loaded MSNs were used in combination with suitable caps and AuNT@PEG for the detection of *Mycoplasma* genomic DNA and cocaine. In both cases a highly selective and sensitive response was found. We propose that a wide variety of SERS-active molecules can be used as cargo in different capped systems, which can be selectively opened in the presence of specific target analytes and combined with SERS efficient plasmonic nanoparticles, rendering this approach appealing and full of potential for the design of new sensing systems.

Experimental section

Materials: Hexadecyltrimethylammonium chloride (CTAC, 25 wt % in water), hydrogen tetrachloroaurate trihydrate ($HAuCl_4 \cdot 3\,H_2O$, ≥99.9 %), crystal violet (CV, ≥90 %), L-ascorbic acid (AA, ≥99 %), *O*-[2-(3-mercaptopropionylamino)ethyl]-*O′*-methylpolyethylene glycol (mPEG-SH, average M_W=5000), sodium borohydride ($NaBH_4$, 99 %), tetraethylorthosilicate (TEOS), (3-isocyanatopropyl)triethoxysilane, sodium hydroxide, (3-aminopropyl)triethoxysilane (APTES), hydrochloric acid, *n*-cetyltrimethylammonium bromide (CTABr, ≥99 %), and tris(hydroxymethyl)aminomethane (Tris) were purchased from Aldrich. Milli-Q water (resistivity of 18.2 MΩ cm at 25 °C) was used in all experiments. The oligonucleotides and aptamers listed in Table 3 were provided by Isogen Life Science. Analytical-grade solvents were obtained from Scharlab (Barcelona, Spain). Cocaine hydrochloride, morphine, methadone, and heroin hydrochloride were provided by the Agencia Española de Medicamentos y Productos Sanitarios (AEMPS). All chemicals were used as received.

Table 3. Oligonucleotide and aptamer sequences used in this work.

Name	Sequence
O1	5′-GGGAGCAAACAGGATTAGATACCCT-3′
O2	5′-AGGGTATCTAATCCTGTTTGCTCCC-3′
O3	NH_2-$(CH_2)_6$-5′-AAAACCCCCCCC-3′
O4	5′-TTTGGGGGGGGGAGACAAGGAAAATCCTTCAATGA AGTGGGTCTCCAGGGGGGTTTT-3′
O5	5′-GAGGTTAACAGAGTGACAGATGGTGCA-3′
O6	5′-AGGGTATCTAATTGCCTGTTGCTCCC-3′
O7	5′-AGGGTATCTAATGGACCTGTTTGCTCCC-3′

General techniques: PXRD, TG analysis, elemental analysis, TEM microscopy, N_2 adsorption–desorption, and UV/Vis spectroscopy were used to characterize the prepared materials. X-ray measurements were performed on a Bruker AXS D8 Advance diffractometer by using CuKα radiation. TEM images of the MSNs were taken with a JEOL TEM-1010 Electron microscope working at 100 kV. TEM images of the AuNPs were collected with a JEOL JEM-1400PLUS instrument operating at 120 kV. N_2 adsorption–desorption isotherms were recorded on a Micromeritics ASAP2010 automated sorption analyzer. The samples were degassed at 120 °C in vacuum overnight. The specific surfaces areas were calculated from the adsorption data in the low-pressure range by using the BET model. The pore size was determined following the BJH method. Fluorescence spectroscopy was carried out on a Jasco FP-8300 Spectrometer. Optical extinction spectra were recorded by using an Agilent 8453 UV/Vis diode-array spectrophotometer. SERS measurements were performed by means of Renishaw inVia system consisting of a confocal Leica microscope equipped with high-resolution diffraction grating (1800 gr mm^{-1}), band pass filter optics, and a Peltier-cooled CCD detector by using a He/Ne laser (λ = 633 nm, maximal output 12.5 mW) as excitation source. All spectra were measured with a long-working distance 50× objective having a numerical aperture of 0.45 from samples in solution within a 1 mL glass vial (Thermo Scientific). Unless otherwise stated, scattered frequencies were collected for 1 s at an irradiation power (P_{laser}) of 6 mW and 100 spectra were accumulated from each sample. Corresponding to each *Mycoplasma* genomic DNA and cocaine concentration an individual reference measurement without the respective analyte was performed. The concentration-dependent SERS data presented here were then plotted as intensity difference between the averaged sample and the averaged reference spectrum.

Buffer solutions: Hybridization buffer consisting in 20 mMTris-HCl, 37.5 mM $MgCl_2$ (pH 7.5) in Milli-Q water, was used for controlled release experiments.

Synthesis of MCM-41 mesoporous nanoparticles: An aqueous solution of NaOH (2 M, 3.5 mL) was added to a solution of CTABr (1.00 g, 2.74 mmol) in deionized H_2O (480 mL). The solution temperature was adjusted to 80 °C. TEOS (5 mL, $2.57 \cdot 10^{-2}$ mol) was subsequently added dropwise to the surfactant solution. The mixture was stirred for 2 h to yield a white precipitate. The final solid was centrifuged, washed with deionized water, and dried at 70 °C for 18 h (MCM-41 as-synthesized). To obtain the final porous material (i.e., MCM-41), the as-synthesized solid was calcined at 550 °C under an oxidizing atmosphere for 5 h to remove the template.

Synthesis of S1: The amino-functionalized solid **S1** was prepared as follows: calcined MCM-41 (500 mg) and CV (161 mg, 0.4 mmol) were suspended in Milli-Q water (20 mL). The suspension was stirred at room temperature for 24 h to load the MCM-41 pores. Afterward an excess of APTES (0.65 mL, 2.77 mmol) was added, and the suspension was stirred at room temperature for 5.5 h. Finally, the resulting solid was isolated by filtration, washed with Milli-Q water (3 mL), and dried at 36 °C for 18 h.

Synthesis of S1-O1: For the preparation of **S1–O1**, the solid **S1** (450 µg) was suspended in a solution containing the oligonucleotide **O1** at a concentration of 40 µM in the hybridization buffer (450 µL), and the suspension was stirred at 37 °C for 30 min. The final solid **S1–O1** was isolated by centrifugation and washed with the hybridization buffer (3×1 mL) in order to remove the residual dye and the free oligonucleotide **O1**.

Synthesis of S2: In a typical synthesis, calcined MCM-41 (300 mg) and CV (98 mg, 0.24 mmol) were suspended in CH_3CN (10 mL). The suspension was stirred at room temperature for 24 h to load the pores. Then, an excess of (3-isocyanatopropyl)triethoxysilane (0.37 mL, 1.5 mmol) was added, and the suspension was stirred at room temperature for 5.5 h. Finally, the resulting solid was isolated by filtration, washed with CH_3CN (3 mL) and dried at 36 °C for 18 h.

Synthesis of S2-O3: Oligonucleotide **O3** (100 µL) was added to a suspension of the solid **S2** (1 mg), triethylamine (2 µL), and CV (1 mM) in CH_3CN (700 µL). The mixture was stirred at room temperature for 3 h. The final solid **S2–O3** was isolated by centrifugation and washed with Milli-Q water (2×700 µL) to eliminate the unbounded oligonucleotide and the dye.

Synthesis of S2-O4: In order to cap the pores of the solid **S2–O3**, a portion of **S2–O3** (200 µg) was suspended in a solution of the cocaine aptamer (**O4**) at a concentration of 5 µM in the hybridization buffer (400 µL). The suspension was stirred at room temperature for 2 h and the final solid **S2–O4** was centrifuged and washed with hybridization buffer to remove the free cocaine aptamer and the residual dye.

Synthesis of gold nanoparticles: Citrate stabilized AuNPs (13 nm), were prepared by the Turkevich method.[65] Briefly, the AuNPs were prepared by injecting sodium citrate (25 mL, 1.7 mM) to the boiling solution of $HAuCl_4$ (500 mL, 0.5 mM). The color of the solution changes from colorless to dark red after 10 min of reaction.

Synthesis of gold nanotriangles: AuNT@PEG were synthesized by a recently reported seeded growth method.[66] In a typical experiment, two growth solutions are prepared: 1) a 0.1 M solution of CTAC (1.6 mL) was added to Milli-Q water (8 mL), followed by a 0.05 M solution of $HAuCl_4$ (40 µL) and a 0.01 M solution of NaI (15 µL); 2) a 0.05 M solution of $HAuCl_4$ (500 µL) was added to a 0.05 M solution of CTAC (40 mL), followed by a 0.01 M solution of NaI (300 µL). The first solution was used to grow the CTAC-capped seed into larger nanoparticles, whereas the second solution was used as the NTs growth batch. Before proceeding, the initial seed@CTAC solution was diluted ten times by using a 0.1 M solution of CTAC. Subsequently, a 0.1 M solution of AA was added to two solutions described above (40 and 400 µL to the first and second solution, respectively), and both solutions were manually stirred until complete transparency of the solutions was achieved. Finally, an aliquot of the diluted seed@CTAC solution (100 µL) was added to the first solution (and manually stirred for one second), and immediately this solution (3.2 mL) was added to the second solution (and manually stirred for a few seconds). The dispersion of the AuNTs was left undisturbed at room temperature for at least one hour. Then, the dispersion of the AuNTs was purified by addition of a solution of CTAC (6.65 mL, 25 wt %) to reach a final CTAC concentration of 0.15 M. Flocculation of the AuNTs was completed overnight, the supernatant was then removed, and the precipitated particles were re-dispersed in a 0.1 M solution of CTAC (5 mL). After TEM characterization, the AuNTs were centrifuged (4000 rpm, 15 min, 30 °C) and stabilized with a suitable amount of mPEG-SH, calculated to add the thiols per NP. The solution was left stirring overnight for proper functionalization. Then, it was centrifuged (4000 rpm, 15 min, 30 °C) and the supernatant was carefully removed. The pellet was finally re-dispersed in Milli-Q water.

Release experiments of S1-O1: To investigate the gating properties of **S1–O1**, this solid (450 µg) was suspended in the hybridization buffer (1.7 mL) and separated in two aliquots (850 µL each). As a control experiment (reference), each first fraction was diluted with Milli-Q water (150 µL) at 50 °C. Whereas the second sample was treated with an aqueous solutions containing different concentrations of oligonucleotide **O2** (150 µL). In both cases, the suspensions were stirred for 60 min at 37 °C. In order to remove the solid, both fractions were centrifuged (8000 rpm, 3 min, 20 °C). Dye delivery was then immediately measured by the fluorescence emission of CV in the solution at λ = 620 nm (λ_{exc} = 590 nm). Subsequently, a solution of AuNT@PEG (20 µL) containing around [Au^0] = 0.04 mM (estimated by using the absorbance at λ = 400 nm[67]) was added to each sample/reference for CV SERS detection. For the release experiments in the presence of *Mycoplasma* genomic DNA, the solid **S1–O1** (1 mg) was suspended in the hybridization buffer (1 mL) and then two aliquots were taken from this suspension. Meanwhile, a solution containing the genomic double-stranded DNA (dsDNA) of *Mycoplasma fermentans* standard (10^3 DNA copies per µL) was heated at 95 °C for 5 min to de-hybridize the dsDNA and then cooled to 50 °C. The DNA solution was added to one of the aliquots to reach a final DNA concentration of 20, 30, 50, 100, or 200 copies per µL, whereas Milli-Q water (without DNA) at 50 °C was added to the second aliquot. Both suspensions were maintained at 37 °C and after one hour the mixtures were centrifuged to remove the solid.

Release experiments of S2-O4: A solution of the solid **S2-O4** (500 µg mL^{-1}, 200 µL) was suspended in the hybridization buffer (800 µL). Then, this suspension was divided in two aliquots and a proper amount of an aqueous solution of cocaine (2 mM) was added to one of the aliquots (samples) to reach a final cocaine concentration of 10^{-5}, 10^{-6}, 10^{-7}, or 10^{-8} M. At the same time, an equal amount of Milli-Q water (without cocaine) was added to the other aliquot (reference). The suspensions were kept at room temperature and after one hour they were centrifuged (8000 rpm, 3 min, 20 °C) to remove the solid. Subsequently, a solution of AuNT@PEG (10 µL) containing around $[Au^0]$ = 0.02 mM ([AuNT@PEG] = $1.2\cdot10^{-10}$ M) was added to each sample/reference for CV SERS detection.

Keywords: gated materials, surface enhanced Raman spectroscopy, biosensors, cocaine, *Mycoplasma*.

Acknowledgements

M.C.-P. acknowledges an FPU Scholarship from the Spanish Ministry of Education, Culture and Sports. L.M.L.- M. acknowledges financial support from the European Research Council (ERC Advanced Grant #267867 Plasmaquo) and the European Union's Seventh Framework Programme (FP7/2007–2013 under Grant Agreement No 312184, SACS). M.O. is grateful to the Universitat Politècnica de València for a FPI-UPV grant. Financial support from the Spanish Government

(Project MAT2015-64139-C4-1-R MINECO/FEDER) and the Generalitat Valenciana (Project PROMETEOII/2014/047) is gratefully acknowledged.

References

1. R. P. Goodman, I. a T. Schaap, C. F. Tardin, C. M. Erben, R. M. Berry, C. F. Schmidt, a J. Turberfield, *Science* **2005**, *310*, 1661–1665.
2. M. Nishikawa, S. Rattanakiat, Y. Takakura, *Adv. Drug Deliv. Rev.* **2010**, *62*, 626–32.
3. A. Mahapatro, *Mater. Sci. Eng. C* **2015**, *55*, 227–251.
4. A. B. Descalzo, R. Martínez-Máñez, F. Sancenón, K. Hoffmann, K. Rurack, *Angew. Chem. Int. Ed.* **2006**, *45*, 5924–5948.
5. K. Ariga, Y. Yamauchi, Q. Ji, Y. Yonamine, J. P. Hill, *APL Mater.* **2014**, *2*, 030701.
6. C. Coll, A. Bernardos, R. Martínez-Máñez, F. Sancenón, *Acc. Chem. Res.* **2013**, *46*, 339–49.
7. Y. Klichko, N. M. Khashab, Y.-W. Yang, S. Angelos, J. F. Stoddart, J. I. Zink, *Microporous Mesoporous Mater.* **2010**, *132*, 435–441.
8. A. Baeza, M. Colilla, M. Vallet-Regi, *Expert Opin. Drug Deliv.* **2015**, *12*, 319–337.
9. C. Argyo, V. Weiss, C. Bräuchle, T. Bein, *Chem. Mater.* **2014**, *26*, 435–451.
10. a) S. Koutsopoulos, *Adv. Drug Deliv. Rev.* **2012**, *64*, 1459–1476; b) G. Bao, S. Mitragotri, S. Tong, *Annu. Rev. Biomed. Eng.* **2013**, *15*, 253–82; c) P. Yang, S. Gai, J. Lin, *Chem. Soc. Rev.* **2012**, *41*, 3679–3698.
11. R. Qian, L. Ding, H. Ju, *J. Am. Chem. Soc.* **2013**, *135*, 13282–13285.
12. E. Aznar, M. Oroval, L. Pascual, J. R. Murguía, R. Martínez-Máñez, F. Sancenón, *Chem. Rev.* **2016**, *116*, 561–718.
13. F. Sancenón, L. Pascual, M. Oroval, E. Aznar, R. Martínez-Máñez, *ChemistryOpen* **2015**, *4*, 418–437.
14. K. Ren, J. Wu, Y. Zhang, F. Yan, H. Ju, *Anal. Chem.* **2014**, *86*, 7494–7499.
15. E. Climent, D. Gröninger, M. Hecht, M. A. Walter, R. Martínez-Máñez, M. G. Weller, F. Sancenón, P. Amorós, K. Rurack, *Chem. Eur. J.* **2013**, *19*, 4117–4122.
16. S. Wu, X. Huang, X. Du, *Angew. Chem. Int. Ed.* **2013**, *52*, 5580–5584.
17. E. Aznar, R. Villalonga, C. Giménez, F. Sancenón, M. D. Marcos, R. Martínez-Máñez, P. Díez, J. M. Pingarrón, P. Amorós, *Chem. Commun.* **2013**, *49*, 6391–6393.
18. S. Sarkar, S. Dutta, T. Pal, *J. Phys. Chem. C* **2014**, *118*, 28152–28161.
19. K. Kneipp, Y. Wang, H. Kneipp, L. T. Perelman, I. Itzkan, R. R. Dasari, M. S. Feld, *Phys. Rev. Lett.* **1997**, 1667–1670.
20. W. Ma, H. Yin, L. Xu, X. Wu, H. Kuang, L. Wang, C. Xu, *Chem. Commun.* **2014**, *50*, 9737-9740.
21. A. La Porta, A. Sánchez-Iglesias, T. Altantzis, S. Bals, M. Grzelczak, L. M. Liz-Marzán, *Nanoscale* **2015**, *7*, 10377–10381.

22. H. Xie, Y. Lin, M. Mazo, C. Chiappini, A. Sánchez-Iglesias, L. M. Liz-Marzán, M. M. Stevens, *Nanoscale* **2014**, *6*, 12403–12407.
23. H. U. I. Wang, D. W. Brandl, *Acc. Chem. Res.* **2007**, *40*, 53–62.
24. A. Shiohara, Y. Wang, L. M. Liz-Marzán, *J. Photochem. Photobiol. C Photochem. Rev.* **2014**, *21*, 2–25.
25. B. Sharma, R. R. Frontiera, A.I. Henry, E. Ringe, R. P. Van Duyne, *Mater. Today* **2012**, *15*, 16–25.
26. T. Kang, S. M. Yoo, I. Yoon, S. Y. Lee, B. Kim, *Nano Lett.* **2010**, *10*, 1189–1193.
27. L. Polavarapu, A. La Porta, S. M. Novikov, M. Coronado-Puchau, L. M. Liz-Marzán, *Small* **2014**, *10*, 3065–3071.
28. D. Cialla, S. Pollok, C. Steinbrücker, K. Weber, J. Popp, *Nanophotonics* **2014**, *3*, 383–411.
29. J. Langer, S. M. Novikov, L. M. Liz-Marzán, *Nanotechnology* **2015**, *26*, 322001.
30. A. F. Palonpon, J. Ando, H. Yamakoshi, K. Dodo, M. Sodeoka, S. Kawata, K. Fujita, *Nat. Protoc.* **2013**, *8*, 677–692.
31. S. Siddhanta, C. Naray, *Nanomater. Nanotechnol.* **2012**, 1.
32. X. X. Han, Y. Ozaki, B. Zhao, *TrAC Trends Anal. Chem.* **2012**, *38*, 67–78.
33. J. J. Giner-Casares, M. Henriksen-Lacey, M. Coronado-Puchau, L. M. Liz-Marzán, *Mater. Today* **2015**, *19*, 19–28.
34. G. Lu, H. De Keersmaecker, L. Su, B. Kenens, S. Rocha, E. Fron, C. Chen, P. Van Dorpe, H. Mizuno, J. Hofkens, et al., *Adv. Mater.* **2014**, *26*, 5124–5128.
35. S. Zong, Z. Wang, H. Chen, J. Yang, Y. Cui, *Anal. Chem.* **2013**, *85*, 2223–2230.
36. G. Zheng, L. Polavarapu, L. M. Liz-Marzán, I. Pastoriza-Santos, J. Pérez-Juste, *Chem. Commun.* **2015**, *51*, 4572–4575.
37. Y. Wang, L. Polavarapu, L. M. Liz-Marzán, *ACS Appl. Mater. Interfaces* **2014**, *6*, 21798–21805.
38. P. Quaresma, I. Osório, G. Dória, P. a. Carvalho, A. Pereira, J. Langer, J. P. Araújo, I. Pastoriza-Santos, L. M. Liz-Marzán, R. Franco, et al., *RSC Adv.* **2014**, *4*, 3659-3667.
39. M. Hecht, E. Climent, M. Biyikal, F. Sancenón, R. Martínez-Máñez, K. Rurack, *Coord. Chem. Rev.* **2013**, *257*, 2589–2606.
40. J.-M. Li, W.-F. Ma, C. Wei, L.-J. You, J. Guo, J. Hu, C.-C. Wang, *Langmuir* **2011**, *27*, 14539–14544.
41. D.-K. Lim, K.-S. Jeon, H. M. Kim, J.-M. Nam, Y. D. Suh, *Nat. Mater.* **2010**, *9*, 60–67.
42. M. Comes, G. Rodríguez-López, M. D. Marcos, R. Martínez-Máñez, F. Sancenón, J. Soto, L. A. Villaescusa, P. Amorós, D. Beltrán, *Angew. Chem. Int. Ed.* **2005**, *44*, 2918–2922.
43. P. C. Choppa, A. Vojdani, C. Tagle, R. Andrin, L. Magtoto, *Mol. Cell. Probes* **1998**, *12*, 301–308.

44. F. J. van Kuppeveld, J. T. van der Logt, A. F. Angulo, M. J. van Zoest, W. G. Quint, H. G. Niesters, J. M. Galama, W. J. Melchers, *Appl. Environ. Microbiol.* **1992**, *58*, 2606–2615.
45. E. Climent, R. Martínez-Máñez, F. Sancenón, M. D. Marcos, J. Soto, A. Maquieira, P. Amorós, *Angew. Chem. Int. Ed.* **2010**, *49*, 7281–7283.
46. C. Chen, J. Geng, F. Pu, X. Yang, J. Ren, X. Qu, *Angew. Chem. Int. Ed.***2011**, *50*, 882–886.
47. M. N. Stojanovic, P. de Prada, D. W. Landry, *J. Am. Chem. Soc.* **2001**, *123*, 4928–4931.
48. P. F. Liao, *J. Chem. Phys.* **1982**, *76*, 751-752.
49. J. Gersten, a Nitzan, *J. Chem. Phys.* **1980**, *73*, 3023-3037.
50. Y. Zhang, B. Walkenfort, J. H. Yoon, S. Schlucker, W. Xie, *Phys. Chem. Chem. Phys.* **2015**, *17*, 21120–21126.
51. W. Meng, F. Hu, L. Y. Zhang, X. H. Jiang, L. D. Lu, X. Wang, *J. Mol. Struct.* **2013**, *1035*, 326–331.
52. E. P. Barrett, L. G. Joyner, P. P. Halenda, *J. Am. Chem. Soc.* **1951**, *73*, 373–380.
53. S. Brunauer, P. H. Emmett, E. Teller, *J. Am. Chem. Soc.* **1938**, *60*, 309–319.
54. S. Razin, D. Yogev, Y. Naot, *Microbiol. Mol. Biol. Rev.* **1998**, *62*, 1094–1156.
55. M. V. Cañamares, C. Chenal, R. L. Birke, J. R. Lombardi, *J. Phys. Chem. C* **2008**, *112*, 20295–20300.
56. E. Climent, L. Mondragón, R. Martínez-Máñez, F. Sancenón, M. D. Marcos, J. R. Murguía, P. Amorós, K. Rurack, E. Pérez-Payá, *Angew. Chem. Int. Ed.* **2013**, *52*, 8938–8942.
57. L. Pascual, I. Baroja, E. Aznar, F. Sancenón, M. D. Marcos, J. R. Murguía, P. Amorós, K. Rurack, R. Martínez-Máñez, *Chem. Commun.* **2015**, *51*, 1414–1416.
58. M. N. Stojanovic, D. W. Landry, *J. Am. Chem. Soc.* **2002**, *124*, 9678–9679.
59. C.-Y. Zhang, L. W. Johnson, *Anal. Chem.* **2009**, *81*, 3051–5.
60. J. Chen, J. Jiang, X. Gao, G. Liu, G. Shen, R. Yu, *Chem. Eur. J.* **2008**, *14*, 8374–8382.
61. J. Liu, J. H. Lee, Y. Lu, *Anal. Chem.* **2007**, *79*, 4120–4125.
62. F. Xia, X. Zuo, R. Yang, Y. Xiao, D. Kang, A. Vallée-Bélisle, X. Gong, J. D. Yuen, B. B. Y. Hsu, A. J. Heeger, et al., *Proc. Natl. Acad. Sci. U. S. A.* **2010**, *107*, 10837–10841.
63. J. Liu, Y. Lu, *Angew. Chem. Int. Ed.* **2006**, *45,* 90–94.
64. B. R. Baker, R. Y. Lai, M. S. Wood, E. H. Doctor, A. J. Heeger, K. W. Plaxco, *J. Am. Chem. Soc.* **2006**, *128*, 3138–3139.
65. J. Kimling, M. Maier, B. Okenve, V. Kotaidis, H. Ballot, A. Plech, *J. Phys. Chem. B* **2006**, *110*, 15700–15707.
66. L. Scarabelli, M. Coronado-Puchau, J. J. Giner-Casares, J. Langer, L. M. Liz-Marzán, *ACS Nano* **2014**, *8*, 5833–5842.
67. J. Rodríguez-Fernández, J. Pérez-Juste, P. Mulvaney, L. M. Liz-Marzán, *J. Phys. Chem. B* **2005**, *109*, 14257–14261.

Chem. Eur. J., 2016, 22, 13488 – 13495

Surface Enhanced Raman Scattering and Gated Materials for Sensing Applications. The Ultrasensitive Detection of Mycoplasma and Cocaine.

SUPPORTING INFORMATION

Mar Oroval, Marc Coronado-Puchau, Judith Langer, Marta Norah Sanz-Ortiz, Angela Ribes, E. Aznar, Carmen Coll, María Dolores Marcos, Félix Sancenón, Luis M. Liz-Marzán and Ramón Martínez-Máñez**

Concentration-dependent SERS of CV

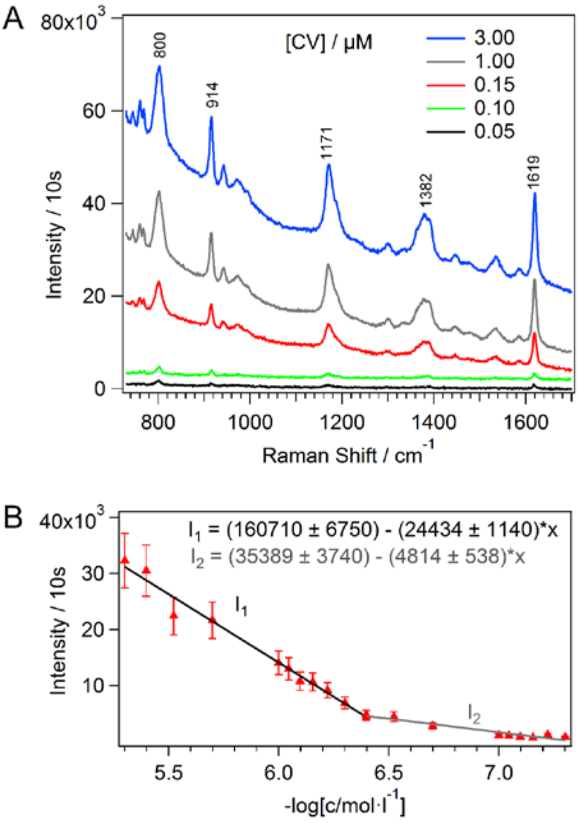

Figure S1. A: Selected concentration-dependent SERS spectra of CV within the range of 3.00 to 0.05 µM. SERS spectra were background corrected using the pure nanoparticle solution without CV as reference and an offset was applied [CV] = 0.15 and 0.1 µM for clearer data representation. **B:** Intensity plot of the 1619 cm^{-1} (most intense peak) as a function of the negative logarithmic CV concentration shows a linear response according to $y_1 = -(24434 \pm 1140)\ x + (160710 \pm 6750)$ within the range of 5.0 to 0.4 µM.; and $y_2 = -(4814 \pm 538)\ x + (35389 \pm 3740)$ within the range of 0.40 to 0.05 µM. Measurement parameters: integration time 10s, laser power 6.2 mW (extended scan). The samples were prepared by mixing 200 mL of AuNT solution ([Au^0] = 0.08 mM corresponding to [AuNT] = 4.8·10^{-10} M) with 200 mL aqueous CV solution of [CV]= 10, 8, 6, 4, 2, 1.8, 1.6, 1.4, 1.2, 1.0, 0.8, 0.6, 0.4, 0.2, 0.18, 0.16, 0.14, 0.12 and 0.10 µM. For the reference sample (background) 200 mL of water was added to the AuNT solution corresponding to [CV]=0.

Characterisation of the materials

N_2 adsorption-desorption measurements of the prepared materials were carried out to study their porous structure. The N_2 adsorption-desorption isotherms of calcined MCM-41 showed two sharp adsorption steps. A first step, at intermediate P/P_0 value (0.1-0.3) (Figure S2, curve a), was attributed to nitrogen condensation inside the mesopores by capillarity. The absence of a hysteresis loop in this interval and the narrow BJH pore distribution suggested the existence of uniform cylindrical mesopores with pore volume of 0.86 $cm^3\ g^{-1}$ calculated by using the BJH model on the adsorption branch of the isotherm. The application of the BET model resulted in a value for the total specific surface of 1055.58 $m^2\ g^{-1}$. From the XRD, porosimetry and TEM studies, a pore diameter of 2.62 nm for MCM-41 was calculated. Besides this adsorption step associated to the micelle generated mesopores, a second feature was observed in the isotherm at a high relative pressure (P/P_0> 0.8). This adsorption corresponds to the filling of larger voids between the particles and yielded a volume of 0.38 $cm^3\ g^{-1}$ (calculated by using the BJH model). This must be considerered texture-like porosity.

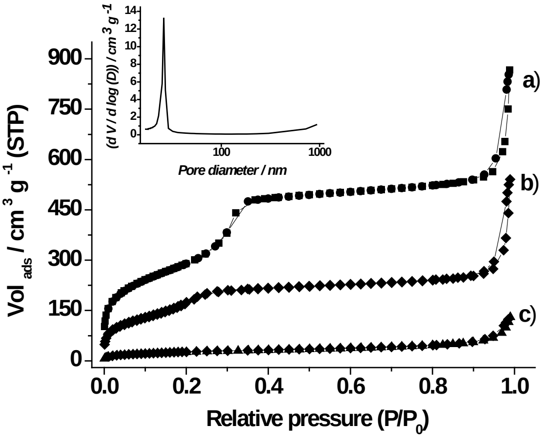

Figure S2. Nitrogen adsorption-desorption isotherms for (a) MCM-41 mesoporous material, (b) **S2** and (c) **S1** materials. Inset: Pore size distribution of MCM-41 mesoporous material.

N_2 adsorption-desorption isotherms of **S1** and **S2** were typical for mesoporous systems with partially filled mesopores (see Figure S2 curves b and c). Moreover, a significant decrease in the adsorbed N_2 volume (0.19 cm^3 g^{-1} and 0.42 cm^3 g^{-1} for **S1** and **S2**, respectively) and surface area (98.5 m^2 g^{-1} and 637.9 m^2 g^{-1} for **S1** and **S2**, respectively) was observed. The most relevant feature in the N_2 adsorption-desorption isotherms for these solids was the absence of a sharp step at low-medium relative pressure ($0.1 < P/P_0 < 0.4$). In fact, these functionalised MSNs showed nearly flat curves when compared (at the same scale) to those of MCM-41, indicating significant pore blocking.

A study of the particle size by dynamic light scattering (DLS) for MCM-41, **S1**, **S1-O1**, **S2**, **S2-O3** and **S2-O4** was carried out. All measurements were performed at 25 °C using a Malvern Zetasizer Nano ZS instrument in triplicate, on previously sonicated dispersions of the nanomaterials in hybridization buffer, at a concentration of 0.01 mg mL^{-1} (see Table S1, Figures S3 and S4). On the other hand, the efficiency of the different surface modifications was studied by Zeta potential measurements of the suspended mesoporous nanoparticles (see Table S1). Bare MCM-41 showed a negative Zeta potential that changed to positive for solids **S1** and **S2** after functionalization with APTES (**S1**) and (3-isocyanatopropyl)triethoxysilane (**S2**), respectively. Zeta potential changed again to negative upon interaction of **S1** and **S2** with the corresponding oligonucleotides (solids **S1-O1**, **S2-O3** and **S2-O4**).

Table S1. Hydrodynamic diameter of MCM-41, **S1**, **S1-O1**, **S2**, **S2-O3** and **S2-O4** solids, measured by DLS.

Solid	Hydrodynamic particle diameter (nm)	Zeta potential (mV)
MCM-41	113.6 ± 24	-11.9
S1	127.2 ± 15.4	19.2
S1-O1	177.4 ± 22.6	-10.86
S2	129.5 ± 16.3	3.51
S2-O3	161.4 ± 18.7	-10.2
S2-O4	190 ± 24	-12.6

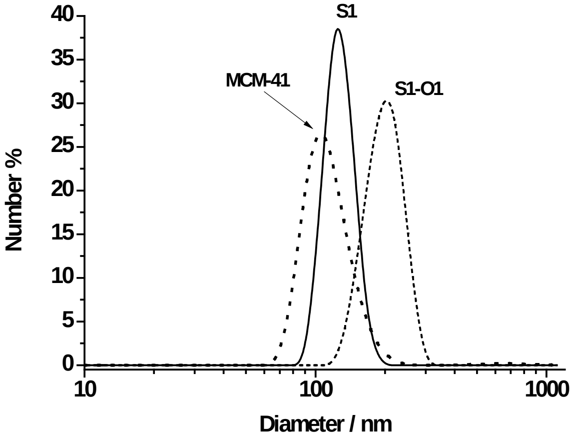

Figure S3. Size distribution by number of particles obtained by DLS studies for calcined **MCM-41**, **S1** and **S1-O1**.

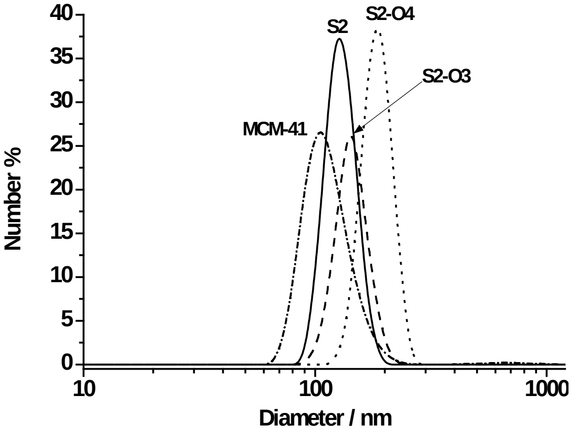

Figure S4. Size distribution by number of particles obtained by DLS studies for calcined **MCM-41**, **S2**, **S2-O3** and **S2-O4**.

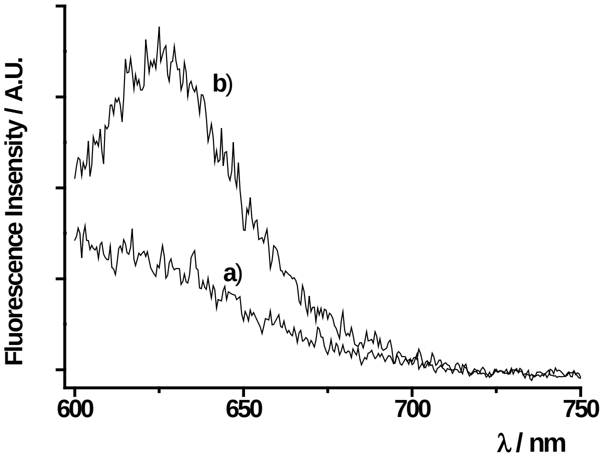

Figure S5. CV fluorescence quenching. Fluorescence spectra (λ_{exc} = 590 nm) of a 1 µM CV aqueous solution in the presence (a) and in the absence of AuNT (b). [Au^0] = 0.5 mM.

Mycoplasma detection

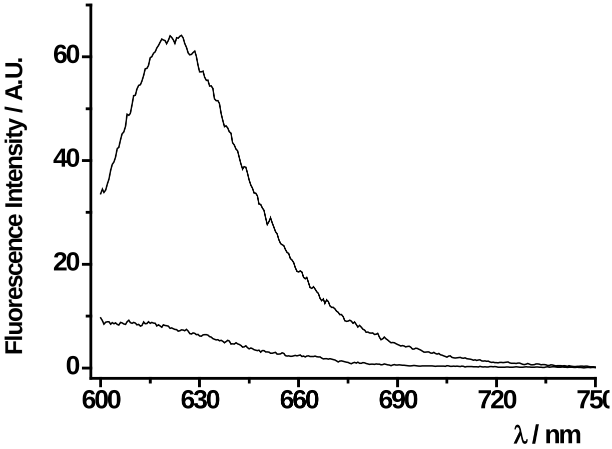

Figure S6. CV fluorescence spectra: Fluorescence spectra of CV released from **S1-O1** in the absence (curve a) and in the presence of oligonucleotide **O2** (curve b). λ_{exc}= 590 nm.

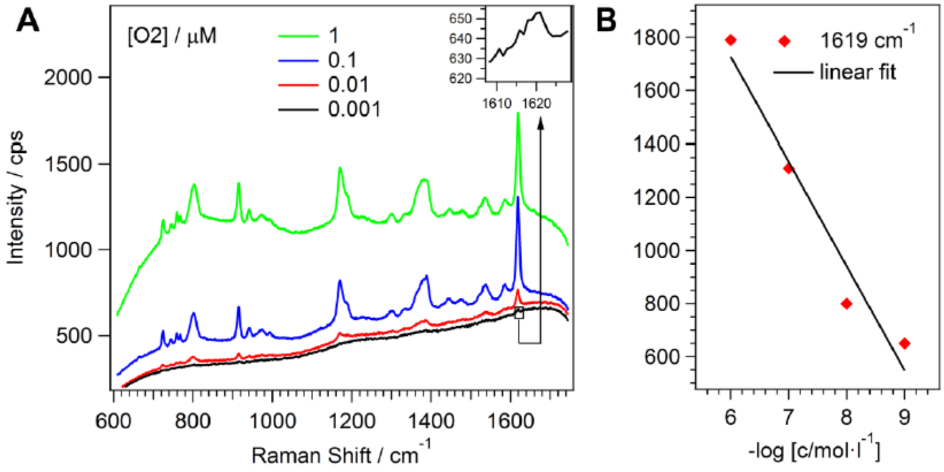

Figure S7. Detection of oligonucleotide O2. A: Detection of CV released as a function of **O2** concentration. Note that **O2** was detected at concentrations as low as 1 nM (see inset). Spectra were not background corrected. **B**: SERS intensity at 1619 cm^{-1}, as function of the negative logarithmic concentration and linear fit to the data (y= -(393 ± 59)x + (4085 ± 448)). Measurement parameters: P_{laser}= 6mW, t_{int} = 1 s, average of 100 accumulations.

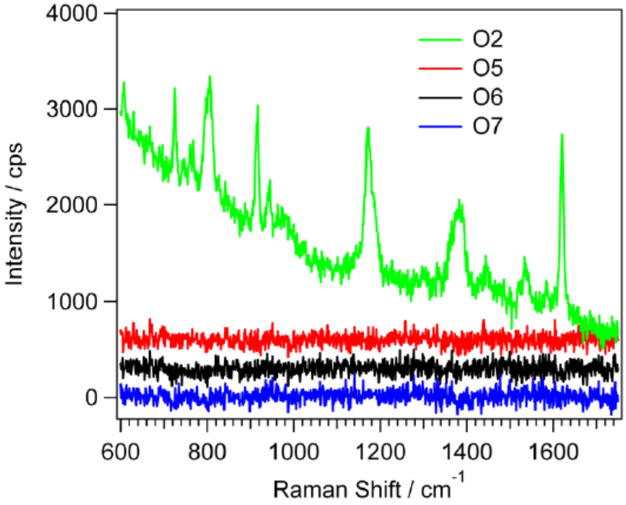

Figure S8. Specificity of solid S1-O1. SERS detection of CV release in the presence of **O2**, **O5**, **O6** and **O7**. The concentration DNA was 1µM in all cases. Note that **O2** is complementary to **O1** while **O3**, **O4** and **O5** are non-complementary oligonucleotides. Spectra were background corrected. Measurement parameters: P_{laser}= 1.2mW, t_{int} = 10 s, 1 accumulation.

5. Self-regulated glucose-sensitive neoglycoenzyme-capped mesoporous silica nanoparticles for insulin delivery

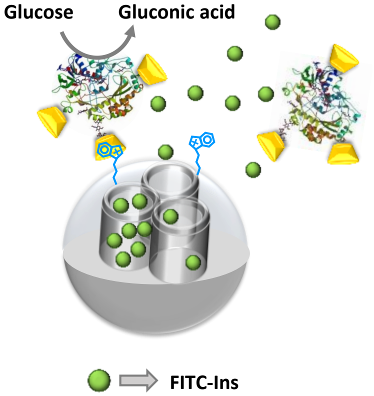

Self-regulated glucose-sensitive neoglycoenzyme-capped mesoporous silica nanoparticles for insulin delivery.

Mar Oroval,[a,b] *Paula Díez ,*[c,d] *Elena Aznar,*[b,a] *Carmen Coll,*[a,b] *María Dolores Marcos,*[a,b,e] *Félix Sancenón,*[a,b,e] *Reynaldo Villalonga*[c,d] *and Ramón Martínez-Máñez**[a,b,e]

[a] Instituto Interuniversitario de Investigación de Reconocimiento Molecular y Desarrollo Tecnológico. Unidad Mixta Universitat Politècnica de València - Universitat de València. Camino de Vera s/n, 46022, Valencia, Spain
[b] CIBER de Bioingeniería, Biomateriales y Nanomedicina (CIBER-BBN).
[c] Department of Analytical Chemistry, Faculty of Chemistry, Universidad Complutense de Madrid, Madrid (Spain)
[d] IMDEA Nanoscience, Cantoblanco Universitary city, Madrid (Spain).
[e] Departamento de Química, Universitat Politècnica de València, Camino de Vera s/n, 46022 València, Spain

Received 30th August 2016
First published on the web 9th November 2016

Chem. Eur. J., DOI: 10.1002/chem.201604104
Reproduced with permission of Wiley-VCH VerlagGmbH&Co. KGaA.

Chem. Eur. J., DOI: 10.1002/chem.201604104

Abstract

We describe herein the preparation of glucose-sensitive capped mesoporous silica nanoparticles for insulin delivery. The new material consists of an expanded pore nanometric silica support grafted with 1-propyl-1-*H*-benzimidazole groups, loaded with fluorescein isothiocyanate-labeled insulin (FITC-Ins) and capped by the formation of inclusion complexes between CD-modified-glucose oxidase (CD-GOx) and the benzimidazole groups grafted on the mesoporous support. Insulin delivery from the gated material in simulated blood plasma was assessed upon addition of glucose. Glucose is transformed by GOx into gluconic acid that promoted the dethreating of the benzimidazole-CD-GOx inclusion complexes allowing cargo release. Small quantities of this support would be needed to release the amount of insulin necessary to decrease diabetic blood glucose concentration to the regular level.

Introduction

Hybrid organic-inorganic nanomaterials have attracted significant interest due to their unique properties resulting from the combination of organic and bioorganic chemistry and material science.[1] In this field, the design and synthesis of mesoporous hybrid gated materials, with the ability to be selectively opened upon the application of an external stimulus and release an entrapped cargo, has generated special interest to the scientific community in recent years.[2-5] These gated materials are composed of two main subunits: (i) a porous scaffold in which a certain cargo is stored and (ii) molecular, supramolecular or biomolecular entities grafted onto the outer surface, which allow control delivery of the entrapped payload.[6,7] Mesoporous silica nanoparticles (MSNs) have been widely used as inorganic support in the construction of gated nanodevices. MSNs present some remarkable features as they are mechanically hard, biocompatible, ease to functionalize using well-known chemistries, have a high loading capacity and tunable pore size.[8–10] In fact, numerous controlled-release systems using mesoporous silica supports have been described using physical,[11-14] chemical[15-17] or biochemical[18-21] stimuli.

From different point of view, diabetes mellitus is a chronic metabolic disease characterized by an accumulating concentration of glucose in blood and urine. This illness, which requires ongoing medical care and patient self-management, takes place when beta cells of pancreas fail to produce insulin (type 1) or produce it insufficiently to overcome insulin resistance in target tissues (type 2).[22] Moreover, it is a major leading cause of mortality in industrialized countries, leading to severe complications, such as kidney disease, retinopathy, neuropathy, leg or foot amputations and heart diseases.[23] In healthy humans, the concentration of glucose in blood is controlled in a finely regulated manner to maintain glucose between 3.5 and 7 mM.[24] In diabetic patients, administration of insulin to help the body to use or store the blood glucose obtained from food is essential in type 1 and longstanding type 2 diabetes patients, requiring continuous dose adjustments based on self-monitoring of blood glucose levels. This widely used therapy is not exempt of hazards. The most important risk when treating with insulin is hypoglycemia.[25] Extremely low blood sugar levels can be life-threatening resulting in seizures, nervous system damage and even comma. Thus, a perfect insulin therapy should minimize the risk of hypoglycemia while improving glycemic control. In this context, the design systems able to detect fluctuations in blood glucose concentrations and release insulin in a self-regulated fashion is highly desirable and still a challenge.[26–28]

In this context different strategies integrated with a large variety of chemical approaches for insulin delivery in response to glucose concentration changes have been reported.[29-39] Nevertheless, only few MSNs based systems have been described for this purpose. One of the first reported examples was developed by Lin et al.,[40] that used MSNs capped with gluconic acid-modified insulin (G-Ins) and loaded with cyclic adenosine monophosphate (cAMP). The nanomaterial demonstrated to be glucose-sensitive, releasing both G-Ins and cAMP. Moreover, Shi and co-workers reported an insulin loaded nanocarrier coated with GOx enzyme-multilayers that were cross-linked with glutaraldehyde and acted as gatekeepers to control the release of insulin in response to glucose.[41] Another example was recently developed by Asefa and co-workers who described the preparation of MSNs for insulin release by tethering insulin molecules onto boronic acid functionalized MSNs and then coating the material with a shell of the pH-sensitive polymer polyacrylic acid.[42] The material exhibited both pH- and glucose-dependent release of insulin.

Based in these concepts and considering the multiple advantages of MSNs as carriers in controlled release applications,[43–45] we report herein the design of a new self-regulated glucose-sensitive platform for insulin release. Our strategy relies on the use of β-cyclodextrin-modified enzyme glucose oxidase (CD-GOx) as gatekeeper in MSNs and the enzymatic reaction between glucose and GOx as trigger which induces insulin delivery.[46] This approach is simple and present some advantages versus other reported glucose-triggered insulin release, such as the storage of insulin into the pores preventing its degradation.

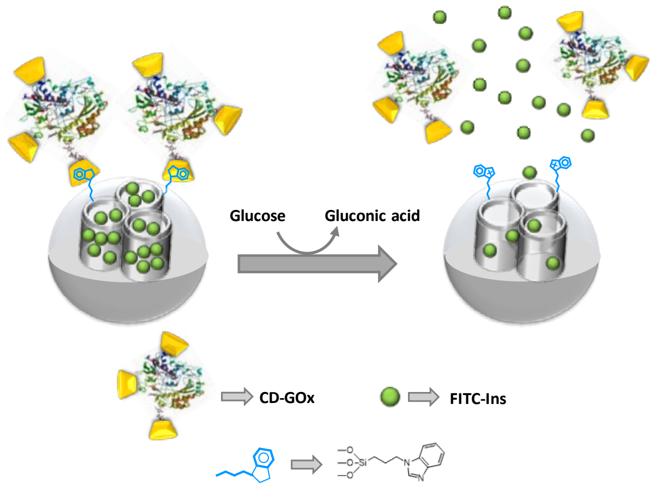

Scheme 1. Schematic representation of the glucose-triggered FITC-Ins release from nanodevice **S3.**

Results and discussion

The glucose-responsive nanomaterial.

The designed nanodevice for controlled insulin release is shown in Scheme 1. The system consists of MSNs with large pores loaded with fluorescein isothiocyanate-labeled insulin (FITC-Ins), functionalized on the outer surface with 1-propyl-1-H-benzimidazol groups and capped by CD-GOx via the formation of inclusion complexes between benzimidazol groups in the pore outlets and β-cyclodextrin groups from CD-GOx (solid **S3**). When **S3** is placed in an aqueous medium, addition of glucose is expected to trigger insulin delivery. Glucose is recognized by glucose oxidase enzyme and hydrolyzed into gluconic acid (pK_a=3.6). The generation of gluconic acid induces a local drop in pH that would cause the protonation of benzimidazol groups (pK_a=5.55) on **S3** and the dethreading of the inclusion complexes between benzimidazol and CD-GOx, finally resulting in the delivery of entrapped insulin yielding solid **S4.**

MSNs with large pores were prepared by the two-step swelling incorporation method, following previous reports with some modifications.[47,48] Especifically, tetramethylorthosilicate (TMOS) and cetyltrimethylammonium bromide (CTABr) were used as the inorganic precursor and structure directing agent, respectively to obtain a nanoparticulated and mesostructured material (**S0-1**). In a second step, material **S0-1** was subjected to a hydrothermal treatment in the presence of equal volumes of 1,3,5-trimethylbenzene (TMB), water, and ethanol to achieve the pore expansion (**S0-2**). Then the surfactant and the pore expanding agent (TMB) were removed by calcination to obtain the final support **S0-3**. The calcined nanoparticles were grafted with 3-iodopropyltrimethoxysilane and the resulting material was treated with benzimidazole yielding solid **S1** which contains 1-propyl-1-*H*-benzimidazole groups in the surface. Subsequently, the pores were loaded with FITC-Ins by a diffusion process to give solid **S2**. Finally, the support was capped by the addition of CD-GOx to a suspension of **S2** in water at pH 7.5 to yield the final capped solid **S3**, which was centrifuged and carefully washed with water at pH 7.5.

Materials characterization.

The prepared materials were characterized using standard procedures. The powder X-ray diffraction (PXRD) pattern of solids **S0-1**, **S0-2**, **S0-3**, **S1** and **S2** are shown in Figure 1. As observed, the PXRD pattern of the as-synthesized nanoparticles **S0-1** (Figure 1, curve a) shows the three typical low-angle reflections of a hexagonal-ordered matrix that can be indexed as (100), (110) and (200) Bragg peaks. However, the regularity of mesopores was highly diminished after pore expansion due to the reorganization of the internal mesostructure, which is corroborated by the significant broadening and the clearly observed displacement of the (100) peak to lower 2θ values (0.976°) (Figure 1, curve b, solid **S0-2**). In addition, diffraction peaks assignable to the (110) and (200) planes disappeared. On the other hand, the condensation of silanol groups during the calcination step is reflected in a slight shift of the (100) peak to higher 2θ values (1.094°) (Figure 1, curve c, solid **S0-3**), corresponding to an approximate cell contraction of 11.3 Å. The a_0 cell parameter for **S0-3** was calculated to be 93.13 Å (d_{100}= 80.65 Å). Finally, curves d and e in Figure 1, correspond to the PXRD pattern of **S1** and **S2**. The presence of the (100) peak in these solids indicated that besides surface functionalization and pore loading, the porous structure in the nanoparticles is preserved.

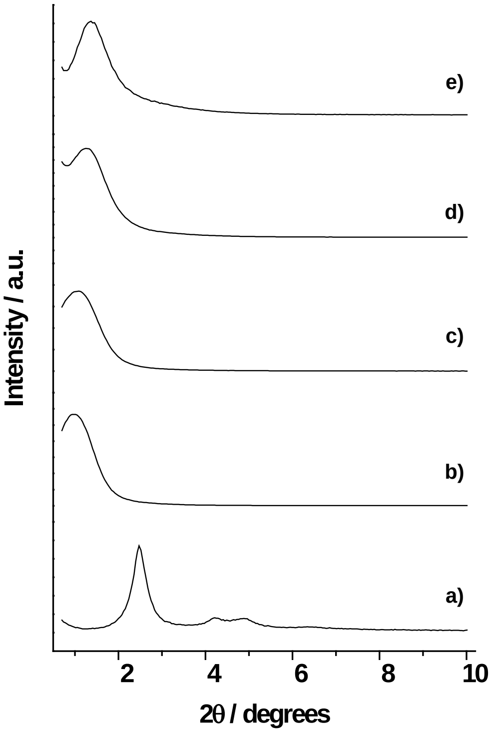

Figure 1. Powder X-ray diffraction patterns of a) as synthesised nanoparticles **S0-1**, b) pore expanded nanoparticles **S0-2**, c) pore expanded and calcined nanoparticles **S0-3**, d) solid **S1** containing 1-propyl-1-*H*-benzimidazole and e) solid **S2** containing 1-propyl-1-*H*-benzimidazole and loaded with FITC-Ins.

By means of transmission electron microscopy (TEM) analysis the porous structure, particle size and morphology of the different samples was also studied. Figure 2 shows a representative image of the calcined scaffold **S0-3**, **S1**, **S2**, **S3** and **S4** materials. It can be clearly seen that these nanoparticles show a spherical form with diameters ranging from 200 to 300 nm. TEM images of **S1**, **S2** and **S3**, also evidence that porosity is still retained after functionalization with 1-propyl-1-*H*-benzimidazole, loading with FITC-Ins and capping with CD-GOx (Figure 2 b, c, d). Moreover, the TEM representative image of solid **S4** (Figure 2 f) confirms that the particle morphology and the porous network remains unaltered after the delivery of FITC-Ins and the detachment of CD-GOx from the surface. In addition, particle size and morphology of solid **S3** was also studied by field emission scanning electron microscopy (FSEM). Figure 2 e confirms the spherical morphology and size of solid **S3** observed in TEM analysis (Figure 2 d).

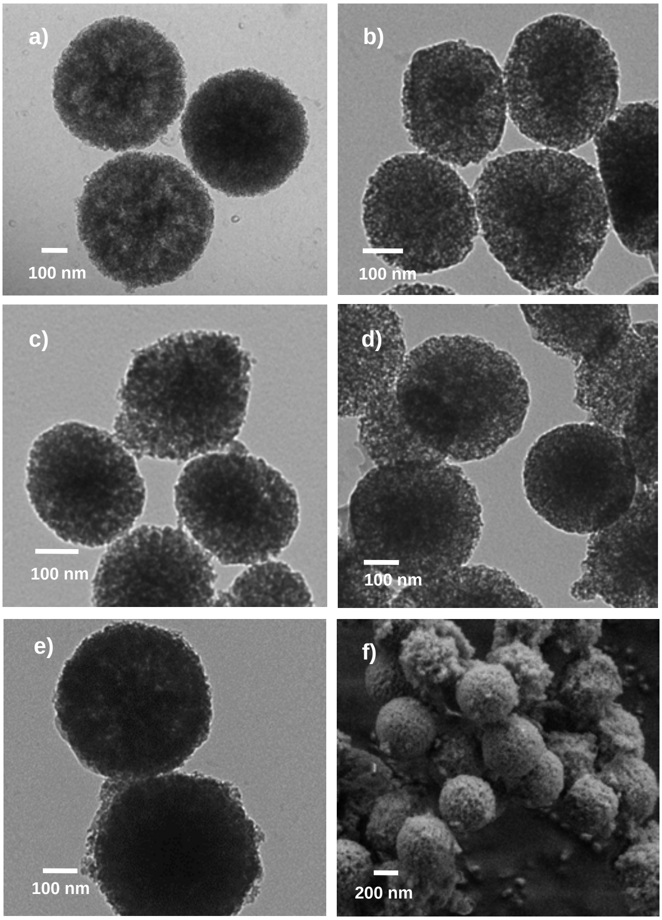

Figure 2. Representative TEM images of a) calcined nanoparticles, b) solid **S1**, c) solid **S2**, d) solid **S3** and e) solid **S4** showing the porosity of the silica-based nanomaterials. f) FSEM image of solid **S3** showing the spherical morphology of the nanoparticles.

As a complement to PXRD and TEM, adsorption-desorption measurements were also carried out to study the porous structure of the calcined nanoparticles **S0-3** and solid **S2** (see Figure 3). Using the Barret-Joyner-Halenda (BJH)[49] model on the adsorption branch of the isotherm the pore diameter and pore volume were calculated (Table 1). Also, the specific surface was calculated by the application of the BET model.[50] The N_2 adsorption-desorption isotherms shown in Figure 3a (calcinated **S0-3** nanoparticles) shows that pore filling occurred over a large range of P/P_0 indicating a wide pore size distribution. On the other hand, the first adsorption step appears at relative high pressure values ($0.7 < P/P_0 < 0.8$)

evidencing the existence of large pores. This step preserves a type-IV isotherm but with a clear H1 hysteresis loop. The total specific area was calculated to be 527 m^2 g^{-1}, whereas the pore size distribution curve (Figure 3, inset) shows a very wide pore size distribution starting in 4 nm and extending up to 18.5 nm, with a mean value of *ca.* 11.8 nm. Futhermore, two shoulders at *ca.* 4.7 and 9.4 nm can also be appreciated.

On the other hand, a pore volume of 0.82 cm^3 g^{-1} and surface area of 302 m^2 g^{-1} where determined for solid **S2** which means a lower N_2 adsorption when compared with the starting calcined material. Moreover, two main features can be appreciated in the pore size distribution of solid **S2**. One is the shift of the maximum towards smaller size values, as it can be expected from the filling of the pores. The second one is that the distribution becomes narrower in the area of smaller pores. This observation may be related with lower difficulty for the FITC-Ins molecules to abandon the solid from the wider pores when washing solid **S2** during the synthesis process. Hence, the smaller pores will remain fully filled while the big ones may still appear not completely blocked.

Table 1. BET specific surfaces, pore volumes, and pore sizes calculated from the N_2 adsorption–desorption isotherms for selected materials.

Sample	S_{BET} (m^2 g^{-1})	Pore volume (cm^{-3} g^{-1})	Pore diameter (nm)
S0-3	527	1.26	11.8
S2	302	0.82	8.9

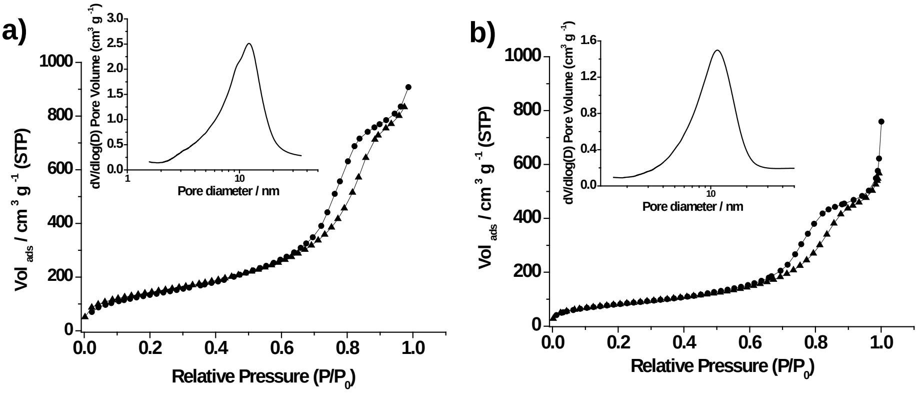

Figure 3. The nitrogen adsorption-desorption isotherms for a) calcined nanoparticles **S0-3** and b) **S2** material. Inset: pore size distribution of the calcined material.

The particle size studies were completed by measuring the diameter of calcined nanoparticles **S0-3** and the hybrid materials **S2** and **S3** by dynamic light scattering (DLS) (Figure 4, and Table 2). All measurements were performed in triplicate on previously sonicated dispersions of the nanomaterials in simulated blood plasma at a concentration of 0.01 mg mL^{-1}. The zeta potential was also determined. Functionalization with benzimidazol moieties and loading with FITC-Ins reduced the zeta potential of the nanoparticles **S2** (-26.5 mV) compared to that of calcined **S0-3** (-31.4 mV). For the final nanodevice **S3**, the surface charge was reduced even more (-17.7) compared to **S2** as a consequence of capping with CD-GOx. In addition an increase of the hydrodynamic diameter after each functionalization step was observed which resulted in a hydrodynamic diameter of 426.1 nm for the final **S3** nanodevice (see Table 2).

Table 2. Particle size distribution by number of particles obtained by DLS studies for calcined nanoparticles **S0-3**, **S2** and **S3**.

Sample	Particle diameter (nm)	Zeta potential (mV)
S0-3	237.9 ± 30.3	-31.4
S2	294.7 ± 41.4	-26.5
S3	426.1 ± 54.2	-17.7-

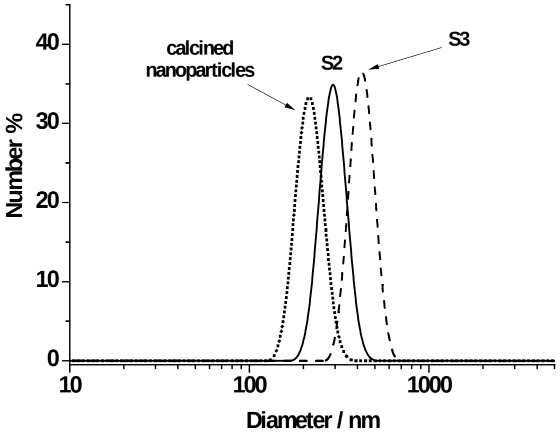

Figure 4. Particle size distribution by number of particles obtained by DLS studies for calcined nanoparticles **S0-3**, **S2** and **S3.**

Moreover, the content of 1-propyl-1-*H*-benzimidazole and FITC-Ins in **S1**, **S2** and **S3** were determined from thermogravimetric and elemental analysis and are detailed in Table 3. Besides, the organic content in solid **S3** was further studied by energy-dispersive X-ray spectroscopy (EDX) measurements. EDX showed the presence of C (38.88 ± 5.14%), N (1.88 ± 0.65%), O (35.97 ± 7.31%) and Si (23.4 ± 7.56%) atoms. In addition, with the aim to estimate the content of CD-GOx retained in the final solid **S3**, the absorbance of CD-GOx in the solution after the capping process was measured. The amount of CD-GOx in the solid **S3** was calculated to be $2.11\cdot10^{-3}$ mg g^{-1} SiO_2, representing 2 U of immobilized neoglycoenzyme per mg SiO_2 according to enzyme activity assays.

Table 3. Content of FITC-Ins and 1-propyl-1-*H*-benzimidazole in the prepared solids **S1**, **S2** and **S3** in mmol g^{-1} SiO_2

Sample	$\alpha_{\text{FTIC-Ins}}$ (mmol $g^{-1}SiO_2$)	$\alpha_{\text{1-propyl-1-}H\text{-benzimidazole}}$ (mmol $g^{-1}SiO_2$)
S1	-	1.24
S2	0.20	1.24
S3	0.17	1.24

Glucose-triggered controlled release of insulin

This section evaluates the self-regulated insulin delivery from **S3** nanoparticles in the presence of glucose. As stated above, in humans, the concentration of this saccharide in blood is controlled by pancreas, which produces and delivers insulin in a finely regulated manner to maintain glucose between 3.5 and 7 mM.[24] The assessment of **S3** in a realistic competitive environment was accomplished by using simulated blood plasma. In a typical experiment, a suspension of **S3** was added to simulated blood plasma (pH 7.4) containing glucose at a concentration of 50 mM. At the same time a similar suspension of **S3** in the absence of glucose was used as control. Both suspensions were stirred for 20 h under dark and aliquots were separated at programmed times and centrifuged in order to remove the nanoparticles and isolate the supernatant. FITC-Ins release was determined by monitoring the fluorescence intensity in the solution (λ_{ex} = 495 nm; λ_{em} = 514 nm). Figure 5 shows the delivery profile of FITC-Ins from solid **S3** in the presence and in the absence of glucose as well as the the FITC-Ins efficiency release from **S3** in %. The results showed that solid **S3** was tightly capped and only a 3 % cargo was released after 20 h in the control experiment (see curve a in Figure 5). In contrast, the presence of 50 mM of glucose induced a remarkable cargo delivery (ca. 26% FITC-Ins release) from solid **S3** after 20 h (curve b). This observation confirms the proposed mechanism, in which the glucose oxidation to gluconic acid by the CD-GOx promotes cargo release. Also, it is worth to mention that the spherical nanoparticle morphology and the porous structure persisted in solid **S4** regardless of the FITC-Ins delivery (Figure 2 e).

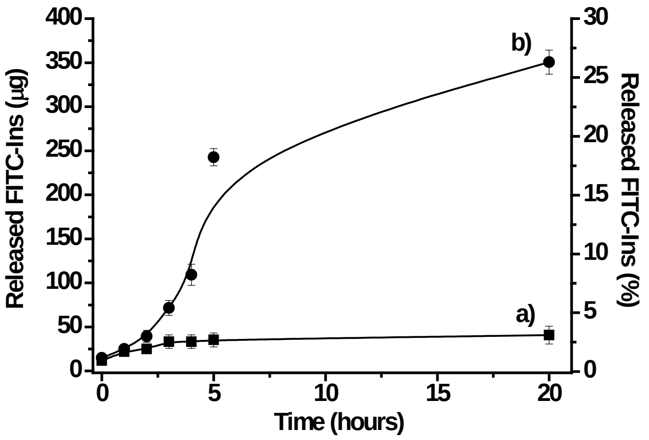

Figure 5. Amount of FITC-Ins released (left y axis) and FITC-Ins release efficiency (right y axis) from 1 mg of solid **S3** as a function of time in the absence (curve a) and in the presence of 50 mM of glucose (curve b).

A more in depth, study of the release profile from **S3** in the presence of glucose showed two different delivery trends. At shorter times, there is a quick release of insulin whereas at longer times the delivery was slower. In order to clarify these two different profiles the release kinetics in the presence of glucose at shorter times (from 0 to 4 hours) were fitted to the Higuchi model. Higuchi's model describes drug release as a diffusion process based in the Ficks's law, square time root time dependent.[51] This extended model takes into account the hypotheses that initial drug concentration in the matrix is much higher than drug solubility, that drug diffusion takes place in only one dimension and that drug diffusivity is constant. This model has been broadly and satisfactorily applied for describing drug release kinetics from insoluble porous matrices.[52,53] Figure 6 shows the fitting of the model to data taken in the first hours of the delivery (from 0 to 4 h). The good fitting observed suggests that FITC-Ins delivery from **S3** pores is essentially a diffusive process. At longer times a certain deviation from linearity was found (data not shown). From Figure 6 it is also possible to observe that solid **S3** presented a y-interception value higher than 0. This phenomenon is known as burst release and leads to an initial massive release occurring in the first minutes after the placement of the delivery system in the release medium. After this phenomenon, the FTIC-Ins release profile follows a more sustained release reaching a maximum delivery at 20

h. This effect (two or more steps in the release profiles) has also been described in other no controlled kinetic release studies of certain guests (usually drugs) from porous carrier materials. As a conclusion, at shorter times the FITC-Ins release is essentially a diffusive process whereas, at longer times, a deviation from the linearity could be observed. This deviation could be ascribed to the fact that the FITC-Ins remaining inside **S3** nanoparticles were strongly adsorbed onto the internal surface of the pores inhibiting, to some extent, its release.

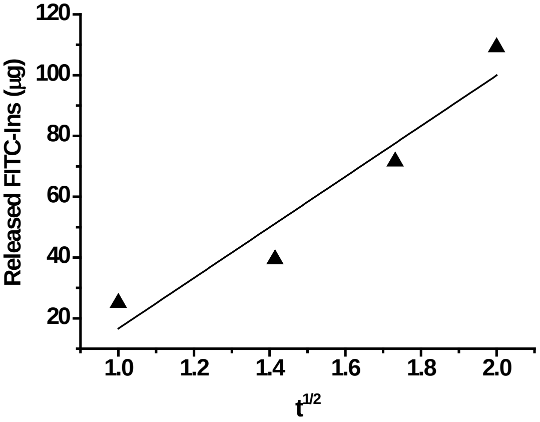

Figure 6. Higuchi release profile of FITC-Ins delivered from solid **S3** in simulated human blood plasma.

As a step forward, the release of FITC-Ins from **S3** as a function of the glucose concentration was studied. In these experiments FITC-Ins delivered after 4 h from **S3** was studied in the glucose concentration range usually found in humans (i.e. up to 40 mM) (see Figure 7). The figure shows that in the presence of small amounts of glucose the delivered FITC-Ins is low. In contrast, when glucose concentration increased the capped system reacted delivering a high FITC-Ins dose mimicking healthy pancreas response and consequently the FITC-Ins release efficiency increases progressively.

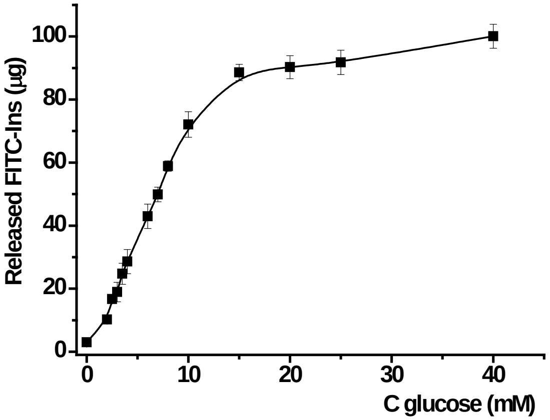

Figure 7. Amount of FITC-Ins released from 1 mg of solid **S3** as a function of glucose concentration after 4h upon addition of the nanomaterial.

The World Health Organization defines diabetes mellitus when fasting plasma glucose level is higher than 126 mg dL^{-1} (7.0 mM) after the intake of 75 g of glucose.[55] This illness, if unmedicated, causes glucose peaks up to 40 mM,[56,57] especially after food intake. In a healthy person, to counteract this effect, blood insulin levels after eating rise more than 10-fold from a baseline of around 20-30 pM to 250-300 pM.[24] Taking into account that the average blood volume in an adult is 5 L, and that **S3** delivers *ca.* 5.91 x 10^{-9} mol of Ins per mg, it can be estimated that the amount of **S3** needed to reach insulin levels in the 250-300 pM range would be as low as *ca*. 110-133 µg of **S3** which is a quite low amount probably tolerable in an *in vivo* scenario.

An important issue when using delivery systems is that they should be ideally selective and deliver the cargo only in the presence of a unique target. In our case, when comparing meals of various combinations of sugars, proteins and fat, only glucose causes blood insulin levels to rise.[24] Thus, it was in our aim to demonstrate that the CD-GOx capped material **S3** is only opened in the presence of glucose and therefore control release experiments from **S3** were carried out in the presence of other saccharides. In particular, the uncapping process in **S3** was monitored after 4 h in simulated blood plasma containing glucose, mannose, fructose, galactose or saccharose at a concentration of 10 mM. As shown in Figure 8, **S3** material shows a notable selectivity for glucose and FITC-Ins delivery from **S3** in the presence of other saccharides was irrelevant. The selective triggering of the FITC-Ins delivery is ascribed to the ability of GOx to catalyze the oxidation of glucose to gluconic acid with high specificity.

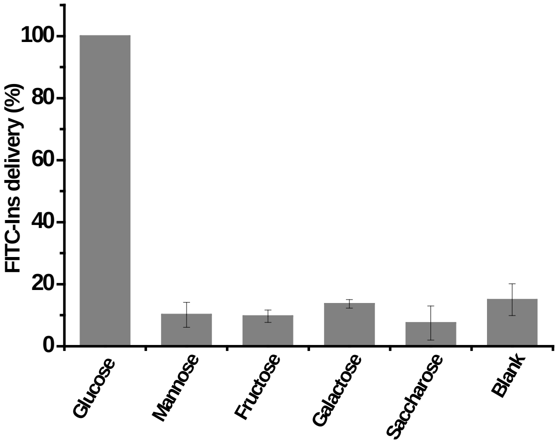

Figure 8. Release of FITC-Ins from solid **S3** in the presence of different saccharides (10 mM) after 4 h.

Conclusions

In summary, we have developed a new glucose-sensitive system for insulin controlled release. Our system consists of MSNs with an expanded pore, loaded with FITC-Ins, functionalized in the external surface with 1-propyl-1-*H*-benzimidazole groups and capped with CD-GOx. Conversion of glucose to gluconic acid by GOx induced the dethreading of the inclusion complexes and thus cargo release. The prepared material demonstrated to be glucose-sensitive by releasing FITC-Ins in simulated blood plasma in presence of glucose. The amount of delivered FITC-Ins was dependent of the concentration of glucose. Moreover, a relatively few amount of the material was able to release suitable amounts of insulin necessary to decrease the blood glucose concentration to the regular level. In addition, the system demonstrated to be highly selective and insulin delivery was only found in the presence of glucose whereas other saccharides were unable to uncap **S3**. Despite the fact that the road from these results to the use of nanoparticles to deliver insulin remains long and uncertain, we believe that such glucose-responsive nanoparticles able to detect levels of glucose in blood and deliver insulin accordingly may open new avenues to future designs of new drug-release system of potential application for diabetes treatment.

Experimental section

General techniques: Powder XRD, TG analysis, elemental analysis, TEM microscopy and N_2 adsorption-desorption techniques were used to characterize the prepared materials. X-ray measurements were performed on a Bruker AXS D8 Advance diffractometer using Cu-K_α radiation. Thermogravimetric analysis were carried out on a TGA/SDTA 851e Mettler Toledo equipment, using an oxidant atmosphere (Air, 80 mL min^{-1}) with a heating program consisting on in a heating ramp of 10 °C per minute from 273 to 373 K followed by an isothermal heating step at this temperature for 60 min in a nitrogen atmosphere (80 mL min^{-1}). Then, the program was allowed to continue with a dynamic heating segment from 373 to 1273 K in an oxidant atmosphere (air, 80 mL min^{-1}) and with an isothermal heating step at this temperature for 30 min. TEM images were taken with a JEOL TEM-1010 Electron microscope working at 100 kV. FSEM images and EDX analysis were performed with a Zeiss Ultra-55 FESEM. N_2 adsorption-desorption isotherms were recorded on a Micromeritics ASAP2010 automated sorption analyser. The samples were degassed at 120 °C in vacuum overnight. The specific surfaces areas were calculated from the adsorption data in the low pressures range using the BET model. Pore size was determined following the BJH method. Fluorescence spectroscopy was carried out on a Jasco FP-8300 Spectrometer.

Chemicals: The chemicals *n*-cetyltrimethylammonium bromide (CTABr), sodium hydroxide (NaOH), fluorescein isothiocyanate (FITC), 3-iodopropyltrimethoxysilane, tetramethylorthosilicate (TMOS), 1,3,5-trimethylbenzene (TMB), benzimidazole, triethylamine, insulin human, dimethyl sulfoxide (DMSO), glucose, mannose, fructose, galactose, maltose and saccharose were provided by Aldrich. Analytical-grade solvents were provided by Scharlab. β-Cyclodextrin-modified glucose oxidase (CD-GOx) was synthesized as previously reported.[26]

Synthesis of MSNs with large pores S0-3: The synthetic procedure of MSNs with large pores was carried out according with previous reports with slight modifications.[21] 3.94 g of CTABr and 2.28 mL 1M of NaOH were dissolved in 800 g ethanol/water (0.4/0.6 = w/w). Then 1.3 mL of TMOS were added to the solution with vigorous stirring. After 8h, the mixture was kept unstirred overnight. The resulting white precipitate was isolated by centrifugation and washed 3 times with ethanol and 3 times with distilled water to obtain solid **S0-1**. The as-synthesised silica nanoparticles **S0-1** were dispersed in 30 mL of ethanol and the mixture was sonicated for 30 min. Subsequently, 20 mL of a 1:1 mixture (v/v) of water and TMB was added to the suspension. The mixture was kept in an autoclave at 140 °C for 4 days. The resulting solid **S0-2** was isolated by centrifugation and washed 3 times with ethanol. Finally, the material **S0-2** was calcined at 550 °C using oxidant atmosphere for 5 h in order to remove the organic content and obtain the support **S0-3**.

Synthesis of fluorescein isothiocyanate-labeled insulin (FITC-Ins): Insulin human was labelled with FITC following previous reports. [10] 2.5 mL of FITC in DMSO (1 mg mL^{-1}) was added in 5 µL aliquots with gentle stirring to a sodium carbonate buffer (0.1 M, pH 9) solution containing insulin (4 mg mL^{-1}). The reaction was stirred for 2 h in dark and at room temperature. Then, 2.5 mL of NH_4Cl 1M was added to the reaction in order to quench the excess of FITC. After stirring for an extra hour, the solution was dialyzed in phosphate-buffered saline and freeze dried yielding FITC labelled insulin. By measuring the absorbance at 495 nm and 280 nm the ratio of FITC to insulin was estimated at 1.4.

Synthesis of S1: The hybrid solid **S1** was prepared by adding an excess of 3-iodopropyltrimethoxysilane (196 µL, 1 mmol) to a suspension of 500 mg of **S0-3**. Then, the suspension was stirred for 5.5 h. The resulting solid was filtered, washed with acetonitrile and dried at 70 °C overnight. Following, 500 mg of the resulting material were suspended in a 40 mL of a saturated solution of benzimidazole in toluene at 120 °C and containing triethylamine (benzimidazol and triethylamine in a 1:3 proportion). The suspension was refluxed and stirred during 72 h. The resulting white solid (**S1**) was filtered off, washed with 10 mL of acetonitrile and dried at 70 °C overnight.

Synthesis of S2: The loading of the pores was carried out by soaking 400 mg of solid **S1** in 40 mL of HCl 0.01 M containing 200 mg of the prepared FITC-Ins. The suspension was stirred for 24 h in dark. The resulting solid was filtered off to yield **S2**, washed with 2 mL of HCl 0.01 M, dried under vacuum and stored in the fridge.

Synthesis of S3: With the aim to obtain solid **S3**, 10 mg of **S2** were suspended in a CD-GOx solution (1 mL, 1.56 mg mL^{-1}) and the suspension was stirred at room temperature for 24 h. The final yellow solid (**S3**) was centrifuged (9500 rpm, 4 min, 20 °C) and washed with deionized water at pH 7.5 five times in order to remove the residual dye and the free CD-GOx.

Release studies: In a typical experiment, 10 mg of freshly prepared **S3** solid were suspended in 1.5 mL of deionized water at pH 7.5. Subsequently, the suspension was separated in different batches of 150 µL and each one was diluted to 3 mL with a mixture of simulated human blood plasma and deionized water at pH 7.5. At a certain time, an aliquot of 0.3 mL of the suspension was separated and centrifuged (8000 rpm, 3 min). The delivered dye was registered by measuring the FITC-Ins emission in the supernatant (λ_{ex} = 495nm).

Keywords: Mesoporous silica, Glucose, Insulin, Controlled release, Molecular gates.

Acknowledgements

Authors thank the Spanish Government (projects CTQ2011-24355, CTQ2014-58989-P, MAT2015-64139-C4-1-R and AGL2015-70235-C2-2-R (MINECO/FEDER)) and the Generalitat Valenciana (project PROMETEOII/2014/047) for support. M.O. thanks the Universitat Politècnica de València for her FPI grant. P.D. thanks the Ministerio de Economía y Competitividad for her FPI grant (BES-2012-054066). C.C. thanks the Generalitat Valenciana for her postdoctoral contract VALi+D.

References

1. L. Nicole, C. Laberty-Robert, L. Rozes, C. Sanchez, *Nanoscale* **2014**, *6*, 6267–6292.
2. A. A. Beltrán-Osuna, J. E. Perilla, *J. Sol-Gel Sci. Technol.* **2015**, 480–496.
3. B. G. Trewyn, I. I. Slowing, S. Giri, H. Chen, V. S. Lin, *Acc. Chem. Res*. **2007**, 846–853.
4. M. Vallet-Regí, F. Balas, *Open Biomed. Eng. J.* **2008**, *2*, 1–9.
5. F. Sancenón, L. Pascual, M. Oroval, E. Aznar, R. Martínez-Máñez, *ChemistryOpen* **2015**, *4*, 418-437.
6. E. Aznar, M. Oroval, L. Pascual, J. R. Murguía, R. Martínez-Máñez, F. Sancenón, *Chem. Rev.* **2016**, *116* , 561–718.
7. S. Alberti, G.J.A.A. Soler-Illia, O. Azzaroni, *Chem. Commun.* **2015**, *51*, 6050–6075.
8. C. Argyo, V. Weiss, C. Bräuchle, T. Bein, *Chem. Mater.* **2014**, *26*, 435–451.
9. A. P. Wight, M. E. Davis, *Chem. Rev.* **2002**, *102*, 3589–3614.
10. G. Kickelbick, *Angew. Chem. Int. Ed.* **2004**, *43*, 3102–3104.
11. N. K. Mal, M. Fujiwara, Y. Tanaka, *Nature* **2003**, *421*, 350-353.
12. J. Liu, C. Detrembleur, M.-C. De Pauw-Gillet, S. Mornet, C. Jérôme, E. Duguet, *Small* **2015**, *11*, 2323-2332.
13. Q. Fu, G.V.R. Rao, L.K. Ista, Y. Wu, B.P. Andrzejewski, L.A. Sklar, T.L. Ward, G.P. Lopez, *Adv. Mater.* **2003**, *15*, 1262-1266.
14. A. Baeza, E. Guisasola, E. Ruiz-Hernandez, M. Vallet-Regí, *Chem. Mater.* **2012**, *24*, 517-524.
15. R. Hernandez, H.R. Tseng, J.W. Wong, J. F. Stoddart, J. I. Zink, *J. Am. Chem. Soc.* **2004**, *126*, 3370-3371.
16. S. Niedermayer, V. Weiss, A. Hermann, A. Schmidt, S. Datz, K. Müller, E. Wagner, T. Bein, C. Bräuchle, *Nanoscale* **2015**, *7*, 7953-7964.
17. X. Zhang, F. Li, S. Guo, X. Chen, X. Wang, J. Li, Y. Gan, *Biomaterials* **2014**, *35*, 3650-3665.
18. K. Patel, S. Angelos, W.R. Dichtel, A. Coskun, Y.W. Yang, J.I. Zink, J.F. Stoddart, *J. Am. Chem. Soc.* **2008**, *130*, 2382-2383.
19. R. Bhat, A. Ribes, N. Mas, E. Aznar, F. Sancenón, M.D. Marcos, J.R. Murguía, A. Venkataraman, R. Martínez-Máñez, *Langmuir* **2016**, *32*, 1195−1200.
20. C. Yu, L. Qian, M. Uttamchandani, L. Li, S.Q. Yao, S. Q. *Angew. Chem. Int. Ed.* **2015**, *54*, 10574-10578.
21. M. Kavruk, O. Celikbickak, V.C. Ozalp, B.A. Borsa, F. Hernandez, G. Bayramoglu, B. Salih, M.Y. Arica, *Chem. Commun.* **2015**, *51*, 8492-8495.
22. M.M Aye, S.L. Atkin, *Drug Healthc. Patient Saf.* **2014**, *6*, 55–67.

23. L.-Y. Chu, *Expert Opin. Ther. Patents.* **2005**, *15*, 1147–1155.
24. J. Suckale, M. Solimena, *Frontiers Biosci.* **2008**, *13*, 7156–7171.
25. American Diabetes Association. *Diabetes Care*, **2014**, *37*, S14–S80.
26. J. C. Pickup, F. Hussain, N. D. Evans, N. Sachedina, *Biosens. Bioelectron.* **2005**, *20*, 1897–1902.
27. T. G. Farmer, T. F. Edgar, N. A. Peppas, *J. Pharm. Pharmacol.* **2008**, *60*, 1–13.
28. G. P. Carino, E. Mathiowitz, *Adv. Drug Deliv. Rev.* **1999**, *35*, 249–257.
29. K.A. Rubeaan, M. Rafiullah, S. Jayavanth, *Expert Opin. Drug Deliv.* **2016**, *13*, 223–237.
30. A. Verma, N. Kumar, R. Malviya, P.K. Sharma, *J Pharm.* **2014**, *2014*, 1–9.
31. R. Mo, T. Jiang, J. Di, W. Taiac, Z. Gu, *Chem. Soc. Rev.* **2014**, *43*, 3595—3629.
32. K. Sato, Y. Imoto, J. Sugama, S. Seki, *Langmuir* **2005**, *21*, 797–799.
33. S. Tanna, T. S. Sahota, K. Sawicka, M. J. Taylor, *Biomaterials* **2006**, *27*, 4498–4507.
34. W. Qi, X. Yan, J. Fei, A. Wang, Y. Cui, J. Li, *Biomaterials* **2009**, *30*, 2799–2806.
35. K. Ishihara, M. Kobayashi, N. Ishimaru, I. Shinohara, *Polym. J.* **1984**, *16*, 625–631.
36. Z. Wu, X. Zhang, H. Guo, C. Li, D. Yu, *J. Mater. Chem.* **2012**, *22*, 22788.
37. P. Liu, Q. Luo, Y. Guan, Y. Zhang, *Polymer* **2010**, *51*, 2668–2675.
38. X. Zhang, Y. Guan, Y. Zhang, *J. Mater. Chem.* **2012**, *22*, 16299.
39. N. Akhtar, S.A. El-Safty, M.E. Abdelsalam, H. Kawarada, *Adv. Healthcare Mater.* **2015**, *4*, 2110–2119.
40. Y. Zhao, B. G. Trewyn, I. I. Slowing, V. S.-Y. Lin, *J. Am. Chem. Soc.* **2009**, *131*, 8398–8400.
41. W. Zhao, H. Zhang, Q. He, Y. Li, J. Gu, L. Li, H. Li, J. Shi, *Chem. Commun.* **2011**, *47*, 9459–9461.
42. R. N. Jain, X. Huang, S. Das, R. Silva, V. Ivanova, T. Minko, T. Asefa, *Zeitschrift fuer Anorg. und Allg. Chemie* **2014**, *640*, 616-623.
43. É. Pérez-Esteve, A. Fuentes, C. Coll, C. Acosta, A. Bernardos, P. Amorós, M. D. Marcos, F. Sancenón, R. Martínez-Máñez, J. M. Barat, *Microporous Mesoporous Mater.* **2015**, *202*, 124–132.
44. C. Giménez, C. de la Torre, M. Gorbe, E. Aznar, F. Sancenón, J. R. Murguía, R. Martínez-Máñez, M. D. Marcos, P. Amorós, *Langmuir* **2015**, *31*, 3753–62.
45. C. de la Torre, I. Casanova, G. Acosta, C. Coll, M.J. Moreno, F. Albericio, E. Aznar, R. Mangues, M. Royo, F. Sancenón, R. Martínez-Máñez, *Adv. Funct. Mater.* **2015**, *25*, 687–695.
46. E. Aznar, R. Villalonga, C. Giménez, F. Sancenón, M. D. Marcos, R. Martínez-Máñez, P. Díez, J. M. Pingarrón, P. Amorós, *Chem. Commun.* **2013**, *49*, 6391–6393.
47. M. Mizutani, Y. Yamada, T. Nakamura, K. Yano, *Chem. Mater.* **2008**, *20*, 4777–4782.

48. M. H. Kim, H. K. Na, Y. K. Kim, S. R. Ryoo, H. S. Cho, K. E. Lee, H. Jeon, R. Ryoo, D. H. Min, *ACS Nano* **2011**, *5*, 3568–3576.
49. E. P. Barrett, L. G. Joyner, P. P. Halenda, *J. Am. Chem. Soc.* **1951**, *73*, 373–380.
50. S. Brunauer, P. H. Emmett, E. Teller, *J. Am. Chem. Soc.* **1938**, *60*, 309–319.
51. T. Higuchi, *J. Pharm. Sci.* **1963**, *52*, 1145–1149.
52. É. Pérez-Esteve, M. Ruiz-Rico, C. De La Torre, L. A. Villaescusa, F. Sancenón, M. D. Marcos, P. Amorós, R. Martínez-Máñez, J. M. Barat, Food Chem. **2016**, *196*, 66–75.
53. A. Bernardos, E. Aznar, C. Coll, R. Martínez-Mañez, J. M. Barat, M. D. Marcos, F. Sancenón, A. Benito, J. Soto, *J. Control. Release* **2008**, *131*, 181-189.
54. K. Radhakrishnan, S. Gupta, D. P. Gnanadhas, P. C. Ramamurthy, D. Chakravortty, A. M. Raichur, *Part. Part. Syst. Charact*. **2014**, *31*, 449-458.
55. World Health Organization: World Health Organization, International Diabetes Federation, editors. Definition and diagnosis of diabetes mellitus and intermediate hyperglycemia. Report of a WHO/IDF Consultation. Geneva (Switzerland): WHO Press; 2006.
56. C.C. Thomas, L.H. Philipson, *Med. Clin. N. Am.* **2015**, *99*, 1–16.
57. M. J. Mattu, and Gary W. Small, M. A. Arnold, *Anal. Chem.* **1997**, *69*, 4695-4702.

7. General Discussion

Design of stimuli-responsive nanostructured devices has recently attained significant relevance in areas such as controlled delivery and sensing of target species, also offering a wide range of future extraordinary applications. The main goal of the present thesis was to contribute to this field. Indeed, the different hybrid materials here presented were designed in order to respond to different biotechnological and environmental necessities. The findings of all the studies carried out in the development of this thesis are detailed in four original research papers and this section aims to give a comprehensive overview of the results presented in this PhD thesis.

First of all, a general introduction was included in order to put the present PhD thesis in context. This first chapter encompassed main aspects of nanotechnology, and the development of hybrid organic-inorganic mesoporous materials and their potential applications. Particularly, the use of stimuli-responsive hybrid materials as sensing and controlled release systems was detailed. As a final point, this chapter included a brief description of some significant examples of gated nanodevices based on mesoporous silica supports for these applications (sensing and controlled delivery).

The following part of the thesis comprises three chapters focused on the design, synthesis, characterization and evaluation of new hybrid materials containing molecular gates for the detection of relevant chemical and biochemical species. To apply gated materials for sensing protocols, the prepared materials must be capable of retaining a reporter inside the pores and of delivering it by upon the application of specific stimuli, which triggers the release of the loaded reporter. In this approach, the capping mechanism is designed in such a way that a target analyte is able to selectively trigger uncapping of the pores. This new sensing protocol offers the advantage of possible amplification features. In this case, the presence of relatively few molecules of the target analyte may induce the release of a relatively large amount of entrapped reporter molecules. Using this core concept, chapter two, three and four described the synthesis and evaluation of novel gated-nanocarriers as sensing probes for the detection of α-thrombin, arsenic, *Mycoplasma fermentans* genomic DNA and cocaine.

The second chapter addresses the design and preparation of a new aptamer-gated controlled delivery system for the fluorogenic detection of α-thrombin. Concretely, the protein-responsive gated mesoporous material was constructed by using MCM-41 as inorganic scaffold, loaded with a fluorophore and capped with the TBA aptamer. The aptamer was absorbed on the surface through electrostatic interactions with the positively charged amines on the external particles' surface. Controlled delivery studies confirmed that the fluorophore release was triggered by the presence of α-thrombin. The *in vitro* studies showed a remarkable limit of detection for α-thrombin, ascribed to the high affinity between the capping-aptamer and its target protein. Moreover, the nanocarrier displayed a selective performance since a mixture of other non-binding proteins (such as ovalbumin and BSA) was unable to induce the uncapping of the pores. Additionally, the prepared nanomaterial allowed accurate α-thrombin detection in PBS-diluted human serum.

Having proved in Chapter 2 the suitability of using aptamers in gated-silica nanoparticles for simple chromo-fluorogenic assays, in the third chapter a novel probe for the fluorogenic detection of As(III) was designed and developed. In this case, the aptamer Ars-3 (that selectively recognizes As(III)) was used to cap pores via electrostatic interactions with the anchored amines partially protonated in water at neutral pH. Reporter delivery assays demonstrated that release of dye from the material was selectively triggered in the presence of As(III) due to the aptamer-analyte recognition. The selectivity of the system versus other metal ions was successfully tested and a low limit of detection was achieved. The performance of the nanocarrier in realistic conditions was further confirmed, allowing a highly accurate As(III) detection in tap water samples. Additionally, it might be interesting to remark that this was the first aptamer-gated mesoporous system described for the detection of As(III).

The results obtained in Chapters 2 and 3 confirmed the suitability of gated-MSNs to develop new fluorogenic sensing probes. In order to evaluate other sensing protocols, a new approach was proposed in the fourth chapter. Specifically, Chapter 4 describes the combination of gated MSNs and SERS spectroscopy in the designing of new sensing probes. Two different smart systems for the detection of *Mycoplasma* genomic DNA and cocaine were successfully prepared. The designed systems consisted of MSNs loaded with a SERS reporter and capped either with a suitable DNA sequence for the detection of *Mycoplasma* genomic DNA, or with an aptamer that selectively interacts with cocaine. In both cases, the delivery of the reporter was triggered by the presence of the corresponding target analyte, and was detected by SERS spectroscopy upon adsorption on AuNTs. Both analytes were sensitively detected, reaching improved LODs when compared with other cocaine or *Mycoplasma fermentans* gated-MSNs sensors. No interference was observed in the detection of *Mycoplasma fermentans* when DNA from other pathogens were present in solution. In the same way, selectivity for cocaine in the presence of other nonspecific drugs was successfully verified. It might be of importance to remark that this was the first reported example that combines gated MSNs and SERS for sensing applications, opening the possibility of designing a wide range of new sensing systems.

In Chapter 5, a smart nanomaterial that comprises both sensing and therapeutic functions integrated into a single agent was described. It was developed a gated-nanomaterial that was able to detect fluctuations in glucose concentration and release insulin in a self-regulated manner. To accomplish this, a drug delivery nanosystem consisting of a glucose-responsive enzyme-capped material for insulin delivery was developed. With this purpose, silica nanoparticles were loaded with insulin and capped with active CD-GOx enzyme, through the formation of an inclusion complex between cyclodextrins and the propylbenzymidazole groups anchored to the solid support. Experimental studies confirmed that FITC-Ins release was induced by the presence of glucose in simulated blood plasma. The nanocarrier was also tested in the presence of other saccharides (such as mannose, fructose, galactose, maltose, and saccharose), however no significant insulin delivery was observed. An especial feature to highlight, is the fact that small amounts of the prepared material was able to deliver insulin necessary to decrease the blood glucose concentration to regular levels.

To summarize, it can be concluded that gated MSNs-based materials have been developed, and their application to the design of sensing probes and controlled delivery systems have been described in this PhD thesis. Within this thesis, it has been demonstrated that gated MSNs have the potential to act as sensing systems and also as smart drug delivery systems. Hopefully, some of the results obtained in this PhD thesis would be of inspiration for future applications of hybrid materials in analytical chemistry, clinical diagnosis or advanced drug delivery systems.

8. Conclusions

- A new aptamer-capped hybrid nanomaterial for the detection of α-thrombin has been successfully synthesized and characterized.
    - ✓ The presence of α-thrombin in solution has resulted to effectively induce the release of the entrapped dye. Sensing features of the material have been studied by means of fluorescence spectroscopy.
    - ✓ The sensitivity of the nanoprobe has been determined in simulated human blood plasma and human serum diluted with PBS, achieving a LOD of 2 nM and 4 nM respectively.
    - ✓ The nanomaterial has resulted to be highly selective to thrombin in the presence of a mixture of non-specific proteins, such as OVA and BSA, in human serum diluted with PBS.
    - ✓ Accurate determination of α-thrombin in human serum diluted with PBS has been achieved.

- A novel sensing probe for the detection of As(III) based on aptamer-capped MSNs has been successfully synthesized and characterized.
    - ✓ The feasibility of the proposed sensing mechanism has been studied by means of fluorescence spectroscopy. The presence of As(III) in solution successfully triggered the release of the reporter.
    - ✓ A remarkable LOD for As(III) as low as 0.9 ppb has been determined.
    - ✓ The prepared material has shown to be highly selective to As(III) in the presence of potential interfering metal ions (such as As(V), Ag(I), Pb(II), K(I), Na(I), Fe(III), Fe(II), Mg(II) and Ca(II)).
    - ✓ Accurate As(III) determination in tap water samples has been successfully achieved.

- The combination of gated-mesoporous silica nanoparticles with SERS spectroscopy has been used in the development of *Mycoplasma fermentans* DNA and cocaine sensing systems.

  - ✓ Two gated-hybrid materials for the detection *Mycoplasma* genomic DNA and cocaine have been designed, synthetized and characterized.
  - ✓ SERS spectroscopy has been used to test the triggering features of the corresponding analytes by combining AuNTs and the prepared gated-materials. The presence of the corresponding analytes effectively triggered the delivery of the loaded reporter.
  - ✓ In both cases, the determination of the sensitivity for each corresponding analyte has been successfully accomplished. LOD as low as 30 copies DNA/µL and 10 nM have been achieved for *Mycoplasma genomic* DNA and cocaine detection, respectively.
  - ✓ The selectivity of both materials for *Mycoplasma* genomic DNA and cocaine detection, has been verified in the presence of other pathogens genomic DNA (*Legionella pneumophilia* and *Candida albicans)* and of different drugs (methadone, heroine and morphine), respectively.

- A new glucose-sensitive nanocarrier for insulin controlled release based on GOx-capped silica nanoparticles has been designed, developed and characterized.
  - ✓ The insulin controlled release features or the nanocarrier in the presence of glucose (as a function of time and glucose concentration) has been successfully validated. The nanocarrier demonstrated to be glucose-sensitive by releasing insulin in a glucose concentration-dependent manner in simulated blood plasma.
  - ✓ The material has demonstrated to be glucose-selective whereas other saccharides such as mannose, fructose, galactose and saccharose where unable to induce cargo delivery.
  - ✓ It was found that relatively low quantities of the nanocarrier (*ca.* 210-233 µg) would only be necessary to release enough insulin to decrease diabetic blood glucose concentration to regular levels.

9. Appendices

Appendix I. List of Publications included in this thesis

Oroval, M.; Coll, C.; Bernardos, A.; Marcos, M. D.; Martínez-Máñez, R.; Shchukin, D. G.; Sancenón, F. Selective fluorogenic sensing of As(III) using aptamer-capped nanomaterials. *Submitted to ACS Applied Materials and Interfaces*

Oroval, M.; Díez, P.; Aznar, E.; Coll, C.; Marcos, D.; Sancenón, F.; Villalonga, R.; Martínez-Máñez, R.; Oroval, M.; Díez, P.; Aznar, E.; Coll, C.; Marcos, D. Self-Regulated Glucose-Sensitive Neoglycoenzyme-Capped Mesoporous Silica Nanoparticles for Insulin Delivery. *Chem. Eur. J. DOI: 10.1002/chem.201604104.*

Oroval, M.; Coronado-Puchau, M.; Langer, J.; Sanz-Ortiz, M. N.; Ribes, Angela; Aznar, E.; Coll, C.; Marcos, M. D.; Sancenón, F.; Liz-Marzán, L. M.; Martínez-Máñez, R. Surface Enhanced Raman Scattering and Gated Materials for Sensing Applications: The Ultrasensitive Detection of *Mycoplasma* and Cocaine. *Chem. Eur. J.* **2016**, 22, 13488–13495.

Oroval, M.; Climent, E.; Coll, C.; Eritja, R.; Aviñó, A.; Marcos, M. D.; Sancenón, F.; Martínez-Máñez, R.; Amorós, P. An Aptamer-Gated Silica Mesoporous Material for Thrombin Detection. *Chem. Commun.* **2013**, *49* , 5480–5482.

Appendix II. Other scientific publications

Sancenón, F.; Pascual, L.; Oroval, M.; Aznar, E.; Martínez-Máñez, R. Gated Silica Mesoporous Materials in Sensing Applications. *ChemistryOpen* **2015**, *4*, 418–437.

Aznar, E.; Oroval, M.; Pascual, L.; Murguía, J. R.; Martínez-Máñez, R.; Sancenón, F. Gated Materials for On-Command Release of Guest Molecules. *Chem. Rev.* **2016**, *116*, 561–718.